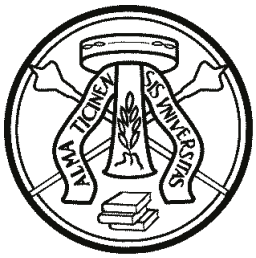

Università degli Studi di Pavia

PhD program in Desing, Modeling and Simulation in Engineering
Department of Civil Engineering and Architecture

Reduced Order Homogenization for Multiscale Analysis of Nonlinear Composites

---

Author:
Alfredo
Castrogiovanni

Supervisor:
Prof. Ferdinando
Auricchio
Coadvisor:
Prof.ssa Sonia Marfia

XXXIII Cycle
2018 - 2021

Abstract

Heterogeneous materials are nowadays used in several fields of structural engineering. Such materials, regarded as *composites*, have a heterogeneous microstructure in which two or more constituents are combined in order to reach improved mechanical properties. Most of the composites include constituents characterized by a nonlinear behaviour, hence, it is important to consider the inelastic phenomena arising at the microscale, to accurately predict the macroscopic response of the heterogeneous material.

A modeling approach allowing for the heterogeneous nature of the composite to be considered during the design process is provided by the Multiscale Analysis, in which both the macroscopic scale and the microscopic scale are involved. At the microscale, a Unit Cell, being a representaive sample of the heterogeneous nonlinear material, is studied in order to derive the behaviour of an equivalent homogeneous macroscopic material. In the scale transition process, usually regarded as *homogenization*, efficient numerical tools are needed in order to reduce the computational cost due to the large quantity of internal variables, coming from the evaluation of the elastoplastic material models at the microscopic level. Reduced Order Models (ROM) are introduced with the aim of lowering the number of internal variables of the problem and to provide accurate solutions with reasonable computational cost and time.

This thesis is mainly dedicated to the development of a ROM for the homogenization of nonlinear heterogeneous materials; starting from the Hashin-Shtrikman analytical homogenization scheme, a piecewise uniform distribution of the microscopic quantities is assumed, and thus, the proposed ROM is referred as PieceWise Uniform Hashin-Shtrikman (PWUHS) technique. In particular, the PWUHS is developed for the solution of homogenization problems of nonlinear composites and extended, in comparison the literature, to Mises plasticity with linear hardening.

Numerical results demonstrate the accuracy of the proposed homogenization

scheme, which is compared to the well known PieceWise Uniform Transformation Field Analysis (PWUTFA) in order to investigate the similarities and the advantages of both reduced order models. PWUHS is implemented in the framework of Multiscale Analysis for studying the response of auxetic composites and numerical results are compared to the experimental counterpart to assess the efficiency of the proposed multiscale scheme.

Acknowledgements

I want to first declare my sincere recognition to Prof. Ferdinando Auricchio for his continuous support and mentoring during the past three years.
I would also like to thank my Ph.D advisor Prof.ssa Sonia Marfia for driving me through my research activity with her precious advises and Prof. Elio Sacco for the valuable expertise and care for details: anything of this work would have been done without your guidance.
Many thanks go to all the people in CompMech group for the partecipation in building a stimulating and friendly envoinronment, I really enjoyed to spend my (good and bad) time with all of you; Gianmaria, Mauro, Michele, Lorenzo, Karim, Ahmed, Franca, Giulia, you deserve more than a thank you for the uncountable laughs and for all the times you lightened my days inside and outside the office. I'm grateful to Gianluca for the help provided during the experimental investigations and the whole 3D Printing lab for the support in developing an efficient experimental setup.
I'm also indebted to the few great people I met in Pavia, Vincenzo and Roberto, for the fantastic time spent in Villa Indipendenza and in VIlla Pilla.
My biggest gratitude goes to the people I love, who supported me despite the distance, Mamma, Papà, Alessandra, Roberta.
Finally I want to thank Aurora, for encouraging me in all my choices. You have been my source of motivation whenever I lacked.

Contents

List of Figures

List of Tables

List of Abbreviations

RVE	**R**epresentative **V**olume **E**lement
UC	**U**nit **C**ell
BC	**B**oundary **C**onditions
ROM	**R**educed **O**rder **M**odel
FEA	**F**inite **E**lement **A**nalysis
FE	**F**inite **E**lements
CH	**C**omputational **H**omogenization
HS	**H**ashin-**S**htrikman
PWUHS	**P**iecewise **U**niform **H**ashin **S**htrikman
TFA	**T**ransformation **F**ield **A**nalysis
PWUTFA	**P**iecewise **U**niform **T**ransformation **F**ield **A**nalysis
UTFA	**U**niform **T**ransformation **F**ield **A**nalysis
NTFA	**N**onuniform **T**ransformation **F**ield **A**nalysis
LC	**L**oad **C**ase
URI	**U**niform **R**educed **I**ntegration
SRI	**S**elective **R**educed **I**ntegration
PU	**P**oly**U**rethane
MJF	**M**ulti **J**et **F**usion
AM	**A**dditive**M**anufacturing

Chapter 1

Introduction

Over the last decades heterogeneous materials have been increasingly used in engineering applications, especially in the field of constructions, aerospace, and automotive. Materials having heterogeneous microstructures are generally manufactured with the aim of improving the performances in terms of properties like the final strength or an optimized weight-strength ratio. Most of the composites include constituents having a nonlinear behaviour, thus, during the design process, it is relevant to consider the microscopic structure, performing accurate and efficient numerical analysis in order to understand how the nonlinearities occurring in the microstructure influence the overall behavior of the heterogeneous material.

In order to take into account the microscopic scale, several modeling approaches are proposed in literature, depending on the observation scale.
At the macroscopic scale, the structural elements can be considered as a homogeneous material, thus, the mechanical properties at this scale mimic the overall properties of the composite material.
On the contrary, at the microscopic scale, the different materials are clearly recognizable and the mechanical properties of the single constituents are used. The interaction between the different constituents are studied and the inelastic phenomena are well captured.
Depending on the scale of analysis, three different approaches can be pursued:

- Macroscopic modeling: this is the simplest and generally most inaccurate, modeling approach. The heterogeneous structure is modeled as a fictitious homogeneous continuum, stress and strain fields are considered as average fields. The constitutive law of the fictituous homogeneous continuum is experimentally derived, this means that the modeling approach can be regarded as a phenomenological approach. The main advantage is that

macroscopic modeling can be easily implemented in the framework of FEA, discretizing the domain in a relatively coarse mesh, making the calculations not expensive. The main disadvantage comes from the impossibility of taking into account the different costituents of the heterogeneous material.

- Microscopic modeling: this approach consists in modeling the heterogeneous material considering the discontinuities between the different constituents. This modeling approach implies a fine discretizetion of the domain in elements being at least as small as the heterogeneities. Microscopic modeling captures the local phenomena and delivers the most accurate global response but leads to a very high computational burden and to memory and time issues.

- Multiscale Analysis: this modeling approach considers both the material or microscale, and the structural or macroscale, thus, it is also known as two-scale technique. At the material scale a micromechanical analysis is performed in order to obtain the overall response of the composite material; the results obtained from the solution of the constitutive problem at the microscale are adopted during the structural analyses. Multiscale analysis overcomes the low accuracy issue tipycal of macroscopic modeling and the prohibitive computational cost of microscopic modeling.

In the framework of two-scale techniques, at the material scale, several analytical homogenization schemes have been proposed in order to obtain the average properties of heterogeneous materials. Initial analytical schemes are based on the solution of auxiliary problems [1, 2]; even if originally introduced for polycrystals, have been successfully extended to composites in general via the self-consistent scheme by Hill [3]. Some analytical approaches provide for variational principles requiring the introduction of elastic reference materials in order to solve linear elastic equivalent problems [4, 5]. These principles were extended to nonlinear problems by Talbot and Willis [6], Ponte Castañeda and Suquet [7, 8, 9], for homogenization of nonlinear materials.

The main advantage of the analytical methods is the very low number of unknowns, coming at the expense of a limited accuracy in prediction of the nonlinear response of heterogeneous materials.

An alternative is given by numerical approaches; a representative volume element (RVE) of the heterogeneous material, is identified and studied to obtain

the overall material response at the structural level. The finite element method can be used both at the macroscale and microscale, leading to the well known FE^2 [10, 11, 12, 13]. This computational homogenization scheme is appreciated for the high accuracy that comes at the expense of a very high computational effort, due to the large quantity of unknowns. Even the generation of meshes, discretizing the complex microstructure geometry, can be very time consuming and for this reason simplified geometries are usually preferred.

Various attempts for reducing the computational burden of the micromechanical analyses have been done developing Reduced Order Models (ROM), whose goal is to obtain a computationally efficient homogenization scheme. A large class of reduced order models is based on *data-clustering*; the solution of the problem is achieved combining the results of simplified computational experiments carried out during an offline phase in order to reduce the number of unknowns. One of the most recent techniques is the Proper Generalized Decomposition (PGD) based on the separated representation of the unknown fields [14]. During an offline stage the problem is solved for every possible value of the free parameters. This allows for a parametric solution of the complex problem that is solved on the fly during the online stage, setting the desired values for the parameters. Even if PGD particularly fits to high-dimensional problems [15, 16, 17], it provides an alternative approach for classical problems [18]. The main drawback of such a powerful approach is the huge quantity of data that must be computed, stored, and combined.

In the eigenstrains or eigenstresses based [19] Reduced Order Models, a numerical counterpart of the localization tensors of the analytical schemes is adopted in order to associate structural and local quantities. Among them, the Transformation Field Analysis (TFA), originally proposed by Dvorak [20] for the homogenization of nonlinear composites, employs eigenstrains in order to account for the inelastic deformation arising from the material nonlinearity. Numerical experiments are carried out on the microsctructure during an offline phase in order to build the localization matrices. Applications of the TFA approach to derive the response of nonlinear composites differ in considering the inelastic strain distribution uniform [20], piecewise uniform [21, 22, 23] or nonuniform [24, 25, 26, 27, 28, 29, 30, 31] throughout the microscopic UC. The more complex the inelastic strain distribution is considered, the better is the accuracy of the homogenization scheme that leads, however, to a larger computational

effort. Some applications, based on the piecewise uniform transformation analysis (PWUTFA) [22, 23], rely upon the RVE subdivision in clusters, or subsets, where the inelastic strain fields are considered uniform.

Some interesting computational homogenization approaches have been derived from Hashin-Shtrikman (HS) variational principle. Luciano and Willis [32] proposed a method of analysis consisting in a FE implementation of the Hashin-Shtrikman variational principle to approximate the elastic behavior of random composites. Recently, a reduced order homogenization scheme has been proposed by Wulfinghoff et al. [33] to study the mechanical response of nonlinear elastic composites. The mechanical problem at the microscale is formulated in terms of the Hashin-Shtrikman variational principle and a homogeneous reference material, coupled to the real nonlinear microstructure by a polarization stress (an eigenstress), is introduced to solve the problem at the microscale. This eigenstress based method is combined with an analytical homogenization scheme [34, 35, 36], thus, it results in hybrid method. As for piecewise TFA [22, 23], HS based methods allow for a progressive refinement of the RVE division into subsets, regions where the polarization stress fields are considered uniform.
The scope of this thesis is to present a novel multiscale technique for studying the response of composite materials, characterized by elastoplastic response. In particular, a Piecewise Uniform Hashin-Shtrikman (PWUHS) reduced order homogenization scheme is developed and adopted at the microscale to get the average response of the heterogeneous material. The problem is formulated for periodic composites and a Unit Cell (UC) representative of the heterogeneous material is studied. A homogeneous elastic reference media is introduced and a piecewise uniform distribution of the polarization stress is considered to couple the reference material to the real material, which is divided in subsets according to the constituents distribution.
In Chapter 2 Multiscale analysis is introduced. General considerations are made on the formulation of the problem at both the structural scale and microscopic scale, focusing on the transition between the two levels. Furthermore, the two main groups of homogenization schemes, namely the analytical and computational homogenization, are introduced. Chapter 3 is dedicated to the presentation of Reduced Order Models, being the main topic of this thesis, as a tool for lowering the computational effort in two-scale homogenization schemes. Among them, the PWUTFA homogenization scheme is illustrated. Chapter 4 presents

the PWUHS homogenization and the governing equations are given. The numerical procedure, adopting an implicit Backward Euler scheme, is developed and the typical time step is solved using a predictor-corrector algorithm where the iterative Newton-Raphson method is used for solving the nonlinear system of equations. Two kind of inelastic material models are considered: Mises plasticity with history variables and elastoplasticity with power law hardening. Different choices for the elastic stiffness matrix of the reference materials are presented: the elastic matrix derived from the homogenization theory by Voigt and the numerically computed overall elastic matrix of the composite material. A secant approach for PWUHS, also for non isotropic homogenized materials, is developed in Section 4.2.1 in order to update the reference material during the analyses. Numerical applications on simplified microstructures, having different material properties and geometries, are carried out in order to investigate the accuracy of the reduced order model. In Chapter 5 the Piecewise Uniform Transformation Field Analysis (PWUTFA) is compared to Piecewise Uniform Hashin-Shtrikman (PWUHS) homogenization technique. The effectiveness of both procedures is evaluated in different cases. In fact, several two-dimensional numerical applications, in plane-strain condition, are carried out, also for complex loading histories. A comparative convergence study is illustrated and the proofs of the equivalence between PWUTFA and PWUHS for composites with homogeneous elastic properties, are given. In Chapter 6 multiscale analysis adopting the PWUHS homogenization technique is used to study the response of heterogeneous materials. In particular, auxetic materials are introduced and a foam-filled honeycomb, belonging to the class of *meta-materials*, is studied via multiscale analysis. Experimental validation of the numerical results is pursued in order to assess the efficiency of the two-scale technique.

Chapter 2

Multiscale Analysis: Theoretical Foundations

In this Chapter the fundamentals of multiscale analysis are presented for stydying the behaviour of heterogeneous materials, which characteristics are strictly related to the observation scale. The formulation of both the structural and microscopic problem is illustrated with a focus on the choice of suitable scale transition law, allowing for the coupling of the different scales and the definition of the microstructural Boundary Value Problem. The notions of *Homogenization* and *Localization* are introduced and an overview of the most relevant analytical and computational homogenization schemes is given.

2.1 Multiscale problem

The behaviour of heterogeneous materials strongly depends on the scale analysis: at the structural or macroscopic scale, having characteristic dimension L, the material appears like an homogeneous medium which behaviour can be described considering overall mechanical properties. On the other hand, at the microscopic scale or microscale, having characteristic size l, the micro-structural constituents can be easily identified (Fig. 2.1). The material phases are usually arranged in complex geometries and are characterized by different properties. Furthermore, different constituents may exhibit different behaviours, so that most of the mechanical and kinematic phenomena arises at this scale.

In order to take into account the phenomena occurring throughout the inner structure, multiscale analysis can be used. This method is based on the *Principle of Scale Separation* claiming that, if the characteristic size at the macroscale

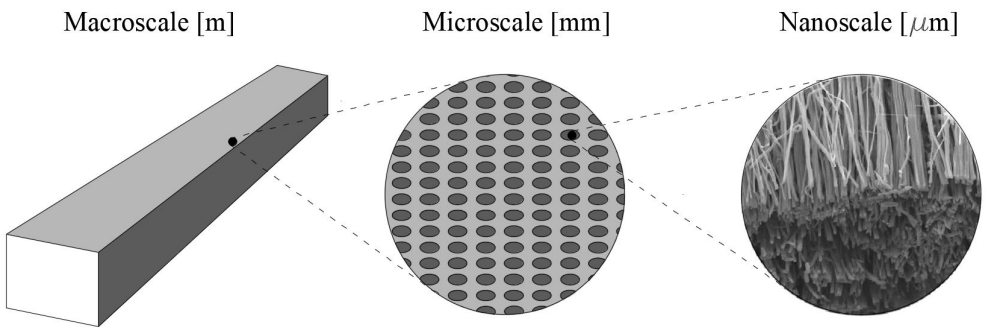

FIGURE 2.1: Characteristic scales.

in much bigger than the miscroscopic lenght scale ($L >> l$), a Representative Volume Element (RVE) containing the heterogeneities of the composite material, can be identified at the smaller scale in order to be considered as statistically representative of the macroscopic homogeneous medium [12].
The choice of a RVE is not an easy task; in the case of random microstructures, which geometries are not known *a priori*, a suitable RVE can be generated following the statistically relevant information of the microstructure such as constituents volume fractions, inclusions shape and orientation. In other cases the observation of the microscopic structure helps in identifying a regular pattern which allows for the detection of a periodic Unit Cell (UC) that can be adopted as RVE in the scheme of multiscale modeling of heterogeneous materials.
After the identification of a suitable RVE, the structural problem can be solved exploiting the multiscale analysis which is based on the interaction between the macroscopic and microscopic scales, as described in the following, in the framework of small strain regime.
At the macroscale, the homogeneous body $\mathcal{B}$ is subjected to body forces $\mathbf{b}$, surface tractions $\mathbf{t}$ on the boundary $\mathcal{S}_t$ and prescribed displacements $\mathbf{U}^*$ on the boundary $\mathcal{S}_u$, such that $\mathcal{S} = \mathcal{S}_u \cup \mathcal{S}_t$ and $\mathcal{S}_u \cap \mathcal{S}_t = \emptyset$.
The displacement field is denoted as $\mathbf{U}(\mathbf{X}) = \{U_1, U_2\}^T$, where $\mathbf{X} = \{X_1, X_2\}^T$ is the position vector of the typical point of $\mathcal{B}$. Under the hypothesis of small strain regime, the strain field $\mathbf{E} = \{E_{11}, E_{22}, \Gamma_{12}\}^T$ at the macroscale, according the Voigt notation, is:

$$\mathbf{E} = \mathbf{B}\,\mathbf{U} \qquad \text{with } \mathbf{B} = \begin{bmatrix} \partial/\partial X_1 & 0 \\ 0 & \partial/\partial X_2 \\ (\partial/\partial X_2) & (\partial/\partial X_1) \end{bmatrix}. \tag{2.1}$$

The stress field is denoted as $\mathbf{\Sigma} = \{\Sigma_{11}, \Sigma_{22}, \Sigma_{12}\}^T$, so that the equilibrium equations and the associated boundary conditions are written as:

$$\begin{array}{lll} \mathbf{B}^T\,\mathbf{\Sigma} + \mathbf{b} = \mathbf{0} & \text{in} & \mathcal{B} \\ \mathbf{N}\,\mathbf{\Sigma} = \mathbf{t} & \text{on} & \mathcal{S}_t \\ \mathbf{U} = \mathbf{U}^* & \text{on} & \mathcal{S}_u \end{array}. \tag{2.2}$$

where $\mathbf{N}$ is the matrix associated to the unit normal vector to $\mathcal{S}_t$.
In a two-scale scheme, $\mathbf{\Sigma}$ is not directly derived from $\mathbf{E}$ evaluating a constitutive law but it is obtained solving a Boundary Value Problem (BVP) at the microscopic level.
The macroscopic response is usually evaluated at material points, as the average response of a microstructural UC representing the heterogeneous material; to this end structural and microscopic scale have to be coupled.

2.2 Micromechanical Problem

A periodic material is considered at the microscale, thus a two-dimensional repetitive UC, denoted by Ω is identified at each macroscopic material point of the macroscopic body $\mathcal{B}$.
At this level, all the different constituents of the composite are distinguishable in the heterogeneous domain Ω, having assigned shape, dimensions and area A. The displacement field is denoted as $\mathbf{u}(\mathbf{x}) = \{u_1, u_2\}^T$, where $\mathbf{x} = \{x_1, x_2\}^T$ is the position vector of the typical point of Ω. Under the hypothesis of small strain regime, the strain field $\boldsymbol{\varepsilon} = \{\varepsilon_{11}, \varepsilon_{22}, \gamma_{12}\}^T$ at microscale is:

$$\boldsymbol{\varepsilon} = \mathbf{D}\,\mathbf{u} \qquad \text{with } \mathbf{D} = \begin{bmatrix} \partial/\partial x_1 & 0 \\ 0 & \partial/\partial x_2 \\ (\partial/\partial x_2) & (\partial/\partial x_1) \end{bmatrix}. \tag{2.3}$$

The equilibrium equations are written in absence of body forces, leading to:

$$\mathbf{D}^T\boldsymbol{\sigma} = \mathbf{0}. \tag{2.4}$$

Concerning the material response at the microscale, no consideration are here made on the relation between strain and stress. In order to solve the microscopic BVP appropriate boundary conditions have to be provided.

2.3 Micro-Macro Scale Transition

A consistent *transition law* is introduced to perform the coupling between the macroscopic amd microscopic scales. This operation is equivalent to a scale transition between the macro and micro level, or rather the transition from the macroscopic loads, defined at each structural material point to the evaluation of the microscopic BC, to be applied on the UC.
The scale transition law is expressed according to Hill's lemma [37]:

$$\langle \boldsymbol{\Sigma} : \delta \mathbf{E} \rangle = \frac{1}{A} \int_{\Omega} \boldsymbol{\sigma} : \delta \boldsymbol{\varepsilon} \, dA, \tag{2.5}$$

where $\langle \bullet \rangle$ denotes the average. Hill's lemma states that the virtual work density at the macroscopic scale corresponds to the volume average of virtual work over the microscopic UC. This means that it is possible to substitute the equilibrium of the macroscopic structure with the solution of the BVP at the microscopic level, if suitable BC are provided.
A macroscopic property can be defined as the volume average over the RVE. Accordingly, the relation between the strain at different scales is:

$$\mathbf{E} = \frac{1}{A} \int_{\Omega} \boldsymbol{\varepsilon} \, dA, \tag{2.6}$$

so that the average strain field over the UC is equal to the macroscopic strain. Equation (2.6) is valid only if there are no voids or cracks over the UC.
On the basis of the average relationship (2.6), the displacement field at microscale can be represented as sum of two contributions, in the form:

$$\mathbf{u} = \bar{\mathbf{u}} + \hat{\mathbf{u}}, \tag{2.7}$$

where $\bar{\mathbf{u}}$ is the displacement map:

$$\bar{\mathbf{u}} = \left\{ \begin{array}{l} E_{11}\, x_1 + \frac{1}{2}\Gamma_{12}\, x_2 \\ \frac{1}{2}\Gamma_{12}\, x_1 + E_{22}\, x_2 \end{array} \right\}, \tag{2.8}$$

and $\hat{\mathbf{u}}$ is the displacement (periodic) fluctuation due to the presence of heterogeneities in the UC. Because of the equations (2.3), (2.7) and (2.8), the strain field takes the form:

$$\boldsymbol{\varepsilon} = \mathbf{E} + \hat{\boldsymbol{\varepsilon}} \qquad \text{with } \hat{\boldsymbol{\varepsilon}} = \mathbf{D}\,\hat{\mathbf{u}}. \tag{2.9}$$

Taking into account the average relationship (2.6) and equation (2.9), the periodic part of the displacement gradient must have null average over the domain:

$$\langle \hat{\boldsymbol{\varepsilon}} \rangle = \mathbf{0}. \tag{2.10}$$

According to equation (2.6), the kinematical BC can be prescribed at the microscale considering the macroscopic deformation tensor $\mathbf{E}$ calculated at the associated material point of the structural scale. In the framework of *strain driven* problems, linear displacements can be prescribed at the boundaries $\partial\Omega$:

$$\boldsymbol{u} = \mathbf{E}\boldsymbol{x}, \qquad \forall \boldsymbol{x} \in \partial\Omega. \tag{2.11}$$

If repetitive RVE's are considered, it is possible to indentify periodicity directions [38] and periodic boundary conditions can be imposed.
To this end, periodic strain are applied to pair of points $\boldsymbol{x}^-$ and $\boldsymbol{x}^+$, lying at opposite boundaries $\partial\Omega^-$ and $\partial\Omega^+$ of the UC, having typical dimension $\Delta\boldsymbol{x}$ (see Fig. 2.2):

$$\boldsymbol{u}^+ = \boldsymbol{u}^- + \mathbf{E}\Delta\boldsymbol{x}, \qquad \forall \boldsymbol{x} \in \partial\Omega. \tag{2.12}$$

Both the described BC satisfy equation (2.5); periodic BC are considered delivering more accurate response and reasonable estimates of the statistically relevant properties.

2.4 Homogenization Problem

With a well posed micromechanical BVP and provided a coherent scale transition law, the constitutive problem is solved at the microscale in order to derive an homogenized macroscopic response (Fig. 2.3).
The macroscopic stress is evaluated calculating the average of the microscopic stress over the domain Ω, so that the Hill condition is satisfied:

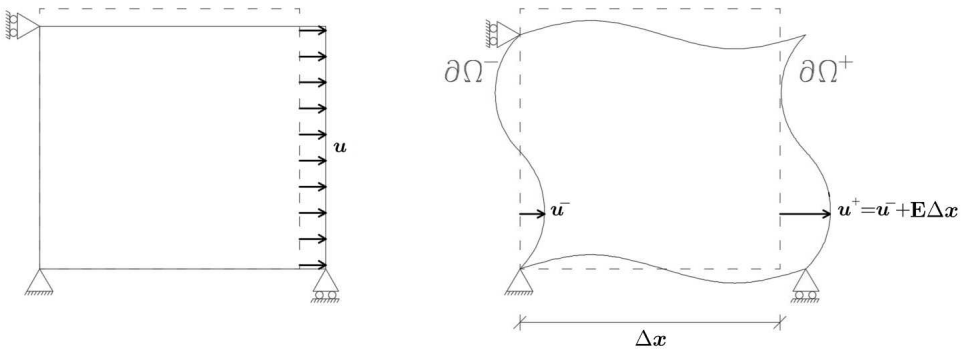

FIGURE 2.2: Linear boundary conditions (left) and periodic boundary conditions (right).

$$\boldsymbol{\Sigma} = \frac{1}{A}\int_{\Omega} \boldsymbol{\sigma}\, dA. \tag{2.13}$$

Considering an elastic material and according to equations (2.6) and (2.13), the constitutive behaviour at the macroscale can be written as:

$$\boldsymbol{\Sigma} = \bar{\mathbf{C}}\mathbf{E}, \tag{2.14}$$

where the overall elastic matrix of the composite material $\bar{\mathbf{C}}$ is introduced, having compliance $\bar{\mathbf{S}} = \bar{\mathbf{C}}^{-1}$.
Since in linear elasticity the stress and strain fields depend linearly on the loading, a relation between macroscopic and local fields can be obtained considering the so called *localization* (or conentration) matrices:

$$\begin{aligned} \boldsymbol{\varepsilon}(\boldsymbol{x}) &= \mathbf{A}(\boldsymbol{x})\mathbf{E}(\mathbf{X}) \\ \boldsymbol{\sigma}(\boldsymbol{x}) &= \mathbf{B}(\boldsymbol{x})\boldsymbol{\Sigma}(\mathbf{X}) \end{aligned}, \tag{2.15}$$

which depend on the microscopic geometry and constituents volume fractions.

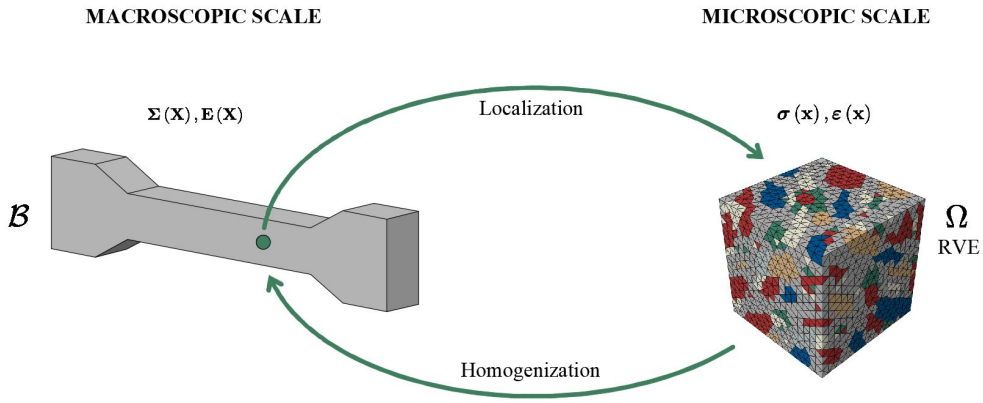

FIGURE 2.3: Multiscale analysis scheme.

Many schemes for the solution of the homogenization (and localization) problems have been developed in oder to predict the overall material response of both linear and nonlinear heterogeneous materials, as shown in the following Section.

2.5 Homogenization Schemes

Homogenization schemes can be classified in three main categories, according to their main characteristics:

- Analytical homogenization schemes, which calculate the mean fields of heterogeneous materials averaging the properties of the constituents;
- Computational homogenization schemes, involving numerical tools as the FE to derive the miscoscopic behaviour of heterogeneous RVEs;
- Reduced Order Models (ROMs), which aim is to solve the microscopic problem reducing the total amount of unknowns. ROMs, being the main topic of this dissertation, are illustrated in Chapter 3.

2.5.1 Analytical Homogenization

Various theories for the analytical determination of mean fields of composites have been developed during the past decades.
Mean field homogenization schemes are able to predict the behaviour of heterogeneous materials starting from basic informations such as constituents' shape, volume fractions, and strain-stress state. A severe limitation of this class of

methods, in comparison with computational approaches, is that they are not able to consider size effects, strain or stress localization.
In the following a selection of the most important analytical homogenization schemes is presented starting from the *self-consistent scheme*, originally proposed by Hill [3]. This homogenization scheme extends the seminal works based on the solution of auxiliary problems [1, 2], originally introduced for homogenization of elementary geometries, to composites in general. Other approaches, based on the introduction of a reference material, provide for suitable variational principles which allow to predict the overall macroscopic characteristics and their bounds [4, 5]. A generalization for inelastic problems is due to Talbot and Willis [6] and further investigations are due to Ponte Castaneda [7, 8, 9].
In comparison with computational honogenization schemes, the analytical methods presented in the following are dramatically faster. Furthermore, some theoretical bounds of the effective material response are reported; these bounds allow for evaluating the quality of the approximated material properties.

2.5.1.1 The self-consistent theory

The self-consistent theory [3, 39, 40, 41] helps in estimating the overall stiffness tensor $\bar{\mathbf{C}}$ of a composite made by a matrix containing n distinct types of inclusions, each with elastic matrix $\mathbf{C}^j$, having volume fractions c^j, $(j = 1, 2, ..., n)$. The elasticity tensor of the matrix, with volume fraction c^{n+1}, is denoted by $\mathbf{C}^{n+1}$. The limiting case of a polycrystal is included in this framework by taking $c^{n+1} = 0$ and allowing an high number for n.
The self-consistent model assumes that each inclusion is isolated and embedded in a fictitious homogeneous matrix, namely the *reference material*, possessing the composite unknown overall stiffness $\bar{\mathbf{C}}$. The homogeneous matrix is subjected to a uniform strain $\mathbf{E}$ far from the inclusion.
Let's define the average strain and stress in the j-th subset as:

$$\boldsymbol{\sigma}^j = \mathbf{C}^j \boldsymbol{\varepsilon}^j. \tag{2.16}$$

It follows that the far field strain and stress, corresponding to the average values in the composite, are:

$$\mathbf{E} = \sum_{j=1}^{n+1} c^j \boldsymbol{\varepsilon}^j, \tag{2.17}$$

$$\boldsymbol{\Sigma} = \sum_{j=1}^{n+1} c^j \boldsymbol{\sigma}^j, \tag{2.18}$$

or, excluding the matrix phase:

$$\boldsymbol{\Sigma} = \mathbf{C}^{n+1}\mathbf{E} + \sum_{j=1}^{n} c^j \left(\mathbf{C}^j - \mathbf{C}^{n+1}\right) \boldsymbol{\varepsilon}^j. \tag{2.19}$$

In order to evaluate the phase-wise average strain, each inclusion is supposed to be embedded in a matrix with stiffness $\bar{\mathbf{C}}$ subjected to the overall strain in equation (2.17), so that:

$$\boldsymbol{\varepsilon}^j = \mathbf{A}^j \mathbf{E}, \tag{2.20}$$

where the introduction of a localization tensor $\mathbf{A}^j$, depending on $\mathbf{C}^j$ and $\bar{\mathbf{C}}$, implies that:

$$\boldsymbol{\Sigma} = \left[\mathbf{C}^{n+1} + \sum_{j=1}^{n} c^j \left(\mathbf{C}^j - \mathbf{C}^{n+1}\right) \mathbf{A}^j\right] \mathbf{E}. \tag{2.21}$$

With equation (2.21) at hand, is now possible to get the overall elasticity tensor, bonding the average stress and strain, using the following equation:

$$\bar{\mathbf{C}} = \mathbf{C}^{n+1} + \sum_{j=1}^{n} c^j \left(\mathbf{C}^j - \mathbf{C}^{n+1}\right) \mathbf{A}^j. \tag{2.22}$$

For ellipsoidal inclusions, the localization tensors $\mathbf{A}^j$ can be explicitly obtained according to the works from Eshelby [2] or Willis [42].
The self-consistent scheme, regarded to deliver good predictions of the average properties of polycristals, is also applied for two-phases composites.

2.5.1.2 The Hashin Shtrikman variational formulation

Hashin and Shtrikman [4] introduced a variational procedure in the linear theory of elasticity that can be applied to the theory of the elastic behaviour of multiphase materials in order to estimate the effective elasticity tensor of linear isotropic composites.
The method introduces a homogeneous elastic reference material and does not relate total stress and strain fields, but *polarization* quantities, representing the deviation of the composite problem from the reference solution, namely the *stress polarization* $\boldsymbol{\tau}(\mathbf{x})$ and the strain fluctuation $\hat{\boldsymbol{\varepsilon}}(\mathbf{x})$.

Consider a heterogeneous domain Ω, composed by two or more materials having elasticity matrices $\mathbf{C}(\mathbf{x})$ and assume that diplacements $\mathbf{u}(S)$ are prescribed on the boundary S and no body forces are present. Let $\mathbf{u}(\mathbf{x})$, $\boldsymbol{\varepsilon}(\mathbf{x})$ and $\boldsymbol{\sigma}(\mathbf{x})$ be the unknown displacements, strain and local stress in the domain.
Consider now another domain Ω_0, with elasticity matrix $\mathbf{C}_0$, having identical geometry and prescribed boundary displacements $\mathbf{u_0}(S)$, being elastic, isotropic and homogeneous. Assume $\mathbf{u_0}$, $\boldsymbol{\varepsilon}_0$ and $\boldsymbol{\sigma}_0$ being respectively the known displacements, strain and stress, with the strain given in terms of the displacements by the usual small strain expression:

$$\boldsymbol{\varepsilon}_0 = \mathbf{D}\mathbf{u_0}. \tag{2.23}$$

Stresses and strain in this domain are related by the Hooke's law, so that:

$$\boldsymbol{\sigma}_0 = \mathbf{C}_0\boldsymbol{\varepsilon}_0, \tag{2.24}$$

with the elasticity matrix of the isotropic homogeneous material defined as:

$$\mathbf{C}_0 = \left[\lambda\left(\mathbf{1}\otimes\mathbf{1}\right) + 2\mu\left(\boldsymbol{I} - \frac{1}{3}\mathbf{1}\otimes\mathbf{1}\right)\right], \tag{2.25}$$

in terms of the Lamè constants λ and μ. The already mentioned *stress polarization*, being a eigenstress field, is now introduced:

$$\boldsymbol{\tau}(\mathbf{x}) = \left(\mathbf{C}(\mathbf{x}) - \mathbf{C}_0\right)\boldsymbol{\varepsilon}(\mathbf{x}). \tag{2.26}$$

This unknown quantity represents the stress gap between the inhomogeneous material and the elastic homogeneous reference material. Taking into account the stress polarization field, a new form of the stress tensor can be obtained as:

$$\boldsymbol{\sigma}(\mathbf{x}) = \mathbf{C}_0\boldsymbol{\varepsilon}(\mathbf{x}) + \boldsymbol{\tau}(\mathbf{x}). \tag{2.27}$$

A further additional unknown of the Hashin-Shtrikman formulation is the strain fluctuation field, defined as:

$$\hat{\boldsymbol{\varepsilon}}(\mathbf{x}) = \boldsymbol{\varepsilon}(\mathbf{x}) - \boldsymbol{\varepsilon}_0. \tag{2.28}$$

If $\tau(\mathbf{x})$ were given, the strain $\boldsymbol{\varepsilon}(\mathbf{x})$ solving the equilibrium:

$$\mathbf{D}^T\boldsymbol{\sigma}(\mathbf{x}) = \mathbf{D}^T\left(\mathbf{C}_0\boldsymbol{\varepsilon}(\mathbf{x})\right) + \mathbf{D}^T\boldsymbol{\tau}(\mathbf{x}) = 0, \tag{2.29}$$

could be expressed as:

$$\boldsymbol{\varepsilon}(\mathbf{x}) = \boldsymbol{\varepsilon}_0 - \boldsymbol{\Gamma}\boldsymbol{\tau}(\mathbf{x}), \tag{2.30}$$

with $\boldsymbol{\Gamma}$ being a linear operator producing a strain fluctuation $\hat{\boldsymbol{\varepsilon}}(\mathbf{x})$ from $\boldsymbol{\tau}(\mathbf{x})$, allowing for the equilibrium in equation (2.29) to be satisfied. It can be noted that the problem on the heterogeneous material is basically tranferred to a problem on a homogeneous material with a fictitious body force $\boldsymbol{\tau}(\mathbf{x})$.
Combining (2.26) and (2.30) an equation for the polarization stress $\boldsymbol{\tau}$ fulfilling the BVP is obtained:

$$\left(\mathbf{C}(\mathbf{x}) - \mathbf{C_0}\right)^{-1}\boldsymbol{\tau}(\mathbf{x}) + \boldsymbol{\Gamma}\boldsymbol{\tau}(\mathbf{x}) = \boldsymbol{\varepsilon}_0, \tag{2.31}$$

which is equivalent to the variational principle:

$$\delta U_p = \delta\left(\frac{1}{2}\boldsymbol{\tau}(\mathbf{x})\left(\mathbf{C}(\mathbf{x}) - \mathbf{C_0}\right)^{-1}\boldsymbol{\tau}(\mathbf{x}) + \frac{1}{2}\boldsymbol{\tau}(\mathbf{x})\boldsymbol{\Gamma}\boldsymbol{\tau}(\mathbf{x}) - \boldsymbol{\tau}(\mathbf{x})\boldsymbol{\varepsilon}_0\right) = 0. \tag{2.32}$$

The stationary value of the functional in (2.32), according to [4, 43], is equal to:

$$U_p = U_0 - U = U_0 - \frac{1}{2}\int_\Omega \boldsymbol{\tau}(\mathbf{x})\left(\mathbf{C}(\mathbf{x}) - \mathbf{C_0}\right)^{-1}\boldsymbol{\tau}(\mathbf{x}) + \frac{1}{2}\boldsymbol{\tau}(\mathbf{x})\boldsymbol{\Gamma}\boldsymbol{\tau}(\mathbf{x}) - \boldsymbol{\tau}(\mathbf{x})\boldsymbol{\varepsilon}_0 \, d\Omega, \tag{2.33}$$

where U_0 is the strain energy density of the homogeneous reference material:

$$U_0 = \frac{1}{2}\int_{\Omega_0} \boldsymbol{\sigma}_0\boldsymbol{\varepsilon}_0 \, d\Omega_0. \tag{2.34}$$

2.5.1.3 Bounds

Analytical homogenization schemes have proved to be an efficient tool for approximation of the effective behaviour of composites. Anyway, even for linear constituents, to determine the overall characteristics of heterogeneous material is not an easy task. The approximations are strongly influenced from the initial assumptions (e.g. phase-wise constant fields) so that it is difficult to assess the quality of the results.
An useful approach to determine the quality of the approximation is to bound

the possible material response, which is supposed to span the interval between an upper and a lower bound.

First-order bounds

A first attempt in bounding the behaviour of heterogeneous materials is due to Voigt [44] and Reuss [45], which independently defined an upper and a lower bound for the elastic strain energy and complementary energy, respectively, of composites with given materials elasticity matrix and volume fractions.
Voigt assumed homogeneous strain $\boldsymbol{\varepsilon}(\mathbf{x}) = \mathbf{E}$ throughout both the inclusion Ω^1 and the matrix Ω^2 such that, if $\langle \boldsymbol{\varepsilon}^1 \rangle = \langle \boldsymbol{\varepsilon}^2 \rangle = \mathbf{E}$, according to equation (2.20), the strain localization matrices are:

$$\mathbf{A}^1 = \mathbf{A}^2 = \mathbf{I}. \tag{2.35}$$

According to Voigt, the composite overall stiffness is:

$$\mathbf{C}^V = c^1\mathbf{C}^1 + c^2\mathbf{C}^2. \tag{2.36}$$

The Voigt average for the overall elasticity tensor is an upper bound on the composite modulus in which kinematic compatibility is fulfilled at the expense of the equilibrium.
Viceversa, the Reuss average considers both material constituents experiencing the same uniform stress $\boldsymbol{\sigma}(\mathbf{x}) = \boldsymbol{\Sigma}$, satisfying the equilibrium at the expense of the compatibility. As a consequence, with the dual equation of (2.20) equal to:

$$\boldsymbol{\sigma}^j = \mathbf{Z}^j\boldsymbol{\Sigma}, \tag{2.37}$$

the stress-concentration tensor $\mathbf{Z}^j$ are:

$$\mathbf{Z}^1 = \mathbf{Z}^2 = \mathbf{I}. \tag{2.38}$$

The overall compliance tensor of the composite material, according to Reuss assumption of uniform stress field, is:

$$\mathbf{S}^R = c^1\mathbf{S}^1 + c^2\mathbf{S}^2. \tag{2.39}$$

This represents a lower bound on the stiffness of the composite.
Voigt and Reuss bounds are obtained provided that both inclusion and matrix are isotropic. Furthermore, when the stiffness of the constituents are far each other, the gap between the upper and the lower bounds is quite big, delivering not accurate information about the overall composite stiffness. This is the reason why more accurate bounds were developed afterwards from Hashin and Shtrikman, as illustrated in the following.

The Hashin-Shtrikman bounds

The variational principle in (2.32) has been used from Hashin and Shtrikman [5] and similarly from Walpole [40] and Willis [43] to find optimal bounds for the overall properties of composite materials made of several inclusions embedded in a matrix.
In order to determine the bounds, the average of equation (2.32) must reach stationarity, such that $\delta\bar{U}_p = \langle \delta U_p \rangle = 0$. Furthermore, the second variation of the average strain energy $\delta^2\bar{U}_p$ determines if the stationary values correspond to a maximum or a minimum:

$$\delta^2\bar{U}_p = \langle \delta\boldsymbol{\tau}(\mathbf{x}) \left(\mathbf{C}(\mathbf{x}) - \mathbf{C_0}\right)^{-1} + \delta\boldsymbol{\Gamma}\boldsymbol{\tau}(\mathbf{x}) \rangle \begin{cases} > 0 & \bar{U}_p \; min \\ < 0 & \bar{U}_p \; max \end{cases} . \tag{2.40}$$

With the functional U_p representing the difference between the strain energy in the real composite and the strain energy in the reference material, being $\mathbf{R} = (\mathbf{C}(\mathbf{x}) - \mathbf{C_0})$ the stiffness gap, the following relation for the stationary values are obtained:

$$R \begin{cases} \text{positive definite, } \delta^2\bar{U}_p > 0, \; \bar{U} = \bar{U}_{max} \\ \text{negative definite, } \delta^2\bar{U}_p < 0, \; \bar{U} = \bar{U}_{max} \end{cases} . \tag{2.41}$$

It is known that optimal Hashin-Shtrikman bounds are found for composites with isotropic constituents or for polycrystals with specific crystal symmetries [46]; an extension for optimal bounds in composites composed by arbitrarily anistropic constituents is due to Walpole [40].
In contrast with the first order bounds, the Hashin-Shtrikman formulation delivers both the upper and lower bounds by an accurate choice of the reference material stiffness. To derive the upper bound the reference material must be as

stiff as the stiffer constituent of the composite; on the contrary, the lower bound is derived if the reference material is as stiff as the weaker constituent in the composite.

The Hashin-Shtrikman variational formulation gives tighter bounds in comparison to the ones derived by Voigt and Reuss which, moreover, can be recovered from the HS formulation giving infinite or null stiffness to the reference material [47].

These bounds, originally derived for polycrystals, are have been mainly used for isotropic composites with isotropic constituents, for both 2D and 3D models, containing sphericle particles or randomly oriented fibers.

In the following first and second order bounds are used to investigate the evolution of mean field moduli in a two-phase elastic composite with varying geometries. In particular, the considered bounds refer to the plane strain bulk modulus λ and shear modulus μ of an isotropic composite made of a circular inclusion with elastic modulus E^1 embedded in a matrix with elastic modulus E^2. Both constituents, which volume fractions are respectively c^1 and c^2, have Poisson ratio $\nu = 0.25$. The composite material is assumed to be *well ordered* [48], in the sense that both the bulk modulus λ^1 and the shear modulus μ^1 of the inclusion are greater than the respective values in the matrix ($\lambda^1 \geq \lambda^2$, $\mu^1 \geq \mu^2$). With a fixed value for $E^2 = 70$GPa, three different increasing values are given to the inclusion elastic modulus: $E^1 = 140$GPa (Fig. 2.4, a, b), $E^1 = 210$GPa (Fig. 2.4, c, d) and $E^1 = 210$GPa (Fig. 2.4, e, f).

As expected, Voigt and Reuss formulations deliver larger bounds in comparison to the Hashin-Shtrikman estimates. Furthermore, is possible to note that both first and second order bounds are sensitive to the increasing gap between the phases elastic properties: the lower is the difference between inclusions and matrix elastic moduli, the tighter are the upper and lower bounds.

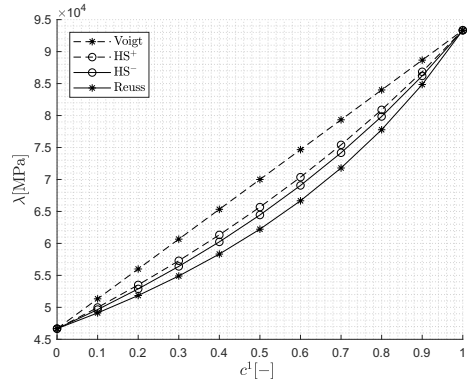

(a)

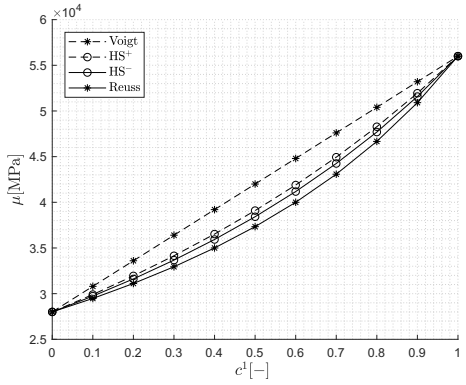

(b)

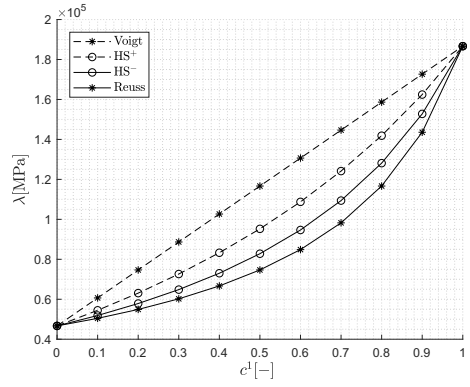

(c)

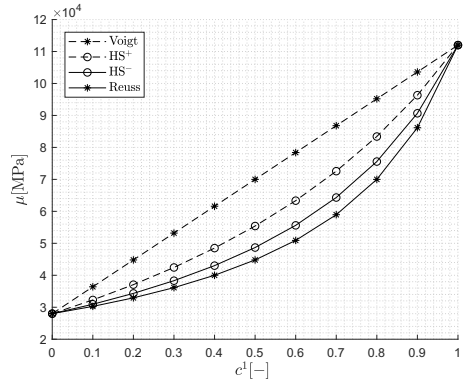

(d)

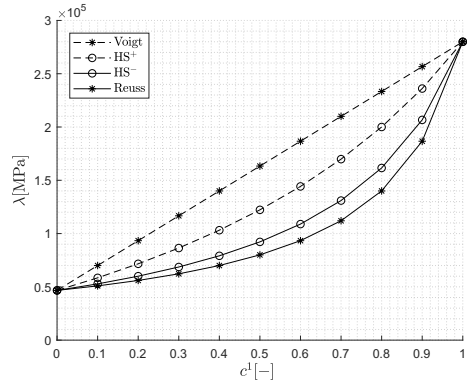

(e)

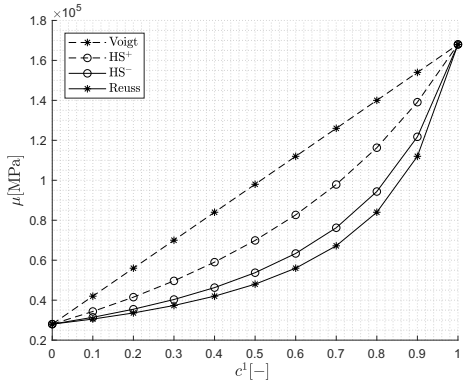

(f)

FIGURE 2.4: Bulk modulus λ and shear modulus μ bounds as a function of the inclusion volume fraction c^1 in a two-phases composite: Voigt (isostrain) bound, Reuss (isostress) bound, Hashin-Shtrikman upper (HS^+) and lower (HS^-) bounds obtained considering E^1=140 GPa (a and b), E^1=210 GPa (c and d), E^1=280 GPa (e and f).

2.5.2 Computational Homogenization

Analytical homogenization schemes are considered to be effective in the mean field prediction of random microstructures, as polycrystals. Such schemes are easy to implement in the framework of two-scales analyses and are numerically inexpensive but show some limits in the applications on ordered microstructures [49]; in particular, is impossible to take into account the interactions between the different material constituents at the microscale and they cannot provide informations about local phenomena, i.e. strain localization.
A possibility to overcome this limitations is provided from the so called *multi-level finite element methods* [50, 51, 52] that are basically nested FE analysis, therefore, outer and inner scales are approached using the FE method. Even if this computational method allows for multiple levels of analysis, two levels are usually taken in consideration so that it is usually referred to as FE^2 [10, 13, 53]. In the framework of computational homogenization methods each integration point (GP) of the macroscopic mesh has an associated RVE on which a separate finite element analysis is performed. An appropriate transition law is provided so that suitable boundary conditions are imposed at the microscopic scale according to the macroscopic strain tensor. Once the micromechanical FE analysis is completed, the macroscopic stress tensor is recovered according to equation (2.13).

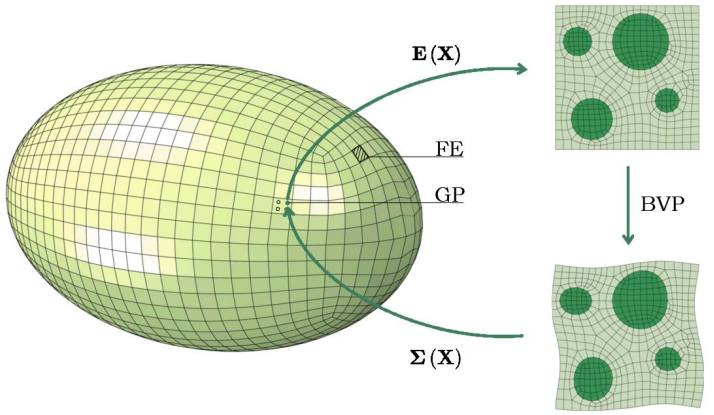

FIGURE 2.5: First-Order Computational Homogenization.

Early FE^2 schemes assume the average strain over the RVE being equal to the macroscopic strain $\mathbf{E}$ (see equation (2.6)): these homogenization approaches,

illustrated in Fig. 2.5, are usually regarded as *first order computational homogenization* schemes, based on the general assumpions of multiscale problems, considering the characteristic size of the microscopic model neglectable if compared to the structural scale.
A direct consequence of this assumption is that only global deformation modes (tension, compression, shear) are captured at the microscale regardless of the RVE dimensions. Increasing the size of the miscoscopic model does not influence the averaged results, meaning that the dimensional properties of the RVE are not relevant and size effects are not captured.
The limitations of the first order CH schemes are relevant if localization phenomena or softening behaviour occur at the microscopic scale. In order to avoid the disadvantages of the first order CH methods, another class of numerical methods usually regarded as *second order* compuational homogenization schemes, has been developed in the framework of large strain regime [11, 54, 55].
The main difference is that also the second order gradient $\mathbf{G}(\mathbf{X})$ of the macroscopic displacements is involved in the definition of the microscopic BC, as shown in Fig. 2.6. At the microscopic scale, if body forces are neglected, the equilibrium equation reads:

$$\mathbf{D}^T\mathbf{p} = \mathbf{0}, \tag{2.42}$$

where $\mathbf{p}$ is the first Piola-Kirchoff stress tensor [56] at the microscopic level. After the microscopic BVP is solved, the macroscopic Piola-Kirchoff stress tensor $\mathbf{P}(\mathbf{X})$ and a higher-order stress tensor $\mathbf{Q}(\mathbf{X})$ are obtained and passed at the macroscopic material point.

The main advantage of computational homogenization schemes is that the evaluation of the constitutive behaviour is carried out at the microscopic level, which is treated in the framework of FEA, thus, RVE with complex geometries can be considered.
However, this leads to the main disadvantage of FE^2 methods, requiring a large number of unknowns evaluations at the microscopic level, where a FE analysis is carried out at each macroscopic integration point.
Furthermore, when nonlinear behaviour are considered at the RVE level, a large amount of history variables has to be stored at each load step, leading to a prohibitive computational burden and, when large deformations occur, a remeshing of the geometry could be required.

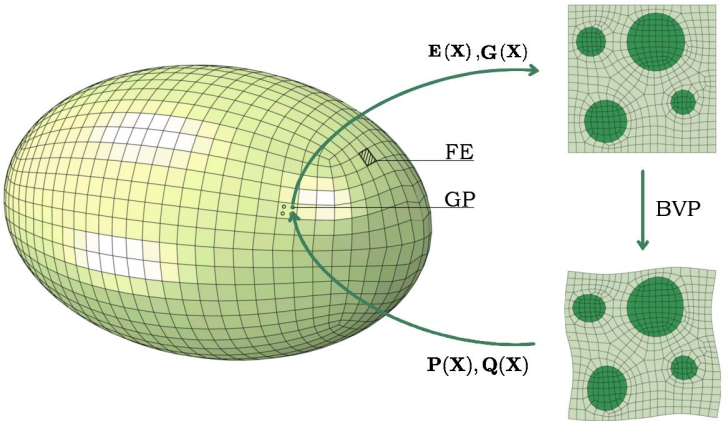

FIGURE 2.6: Second-Order Computational Homogenization.

One of the possible aid in overcoming the CH disadvantages is provided by Reduced Order Models, which aim is to decrease the numerical effort of computational homogenization schemes.

Chapter 3

Reduced Order Models

In this Chapter Reduced Order Models (ROMs), being the main topic of this thesis, are presented as an effective tool to reduce time consuming and storage requirements, in the framework of multiscale analysis. As reported in Chapter 2, the microscopic fields are obtained by mean of a *localization* process and the solution of the microscopic BVP allows for the computation of the homogenized macroscopic quantities.
In the framework of CH, these two concatenad processes have two different complexity levels: while the homogenization corresponds to averaging the microscopic fields, the localization requires the solution of a nonlinear BVP for each macroscopic material point.
In the eigenstrain based [19] ROMs, a numerical counterpart of the localization tensors in 2.15 is adopted in order to associate structural and local quantities.
Among the ROMs the *Transformation Field Analysis*, initially proposed in [20] for homogenization problems of nonlinear composites, is presented in this Chaper, focusing on the numerical procedure of the Piecewise Uniform Transformation Field Analysis (PWUTFA).

3.1 The Transformation Field Analysis

One of the most interesting ROM techniques is the Transformation Field Analysis (TFA), based on the use of eigenstrains in order to consider the inelastic deformation arising from the material nonlinearity.
The applications of this technique for studying the behaviour of nonlinear composites differ in considering the inelastic strain distribution uniform [23], piecewise uniform [22, 23] or nonuniform [23, 24, 25, 26, 27, 29, 31] inside the RVE. These possible assumptions lead, respectively, to the diversification of the method

in Uniform Transformation Field Analysis (UTFA), Piecewise Uniform Transformation Field Analysis (PWUTFA) and Nonuniform Transformation Field Analysis (NTFA).

3.1.1 General Idea

In order to obtain accurate solutions of the micromechanical problem with a reduced computational effort, TFA consider a subdivision of the domain Ω in a number of m *subsets* Ω^j with $j = 1, .., m$, so that:

$$\Omega = \bigcup_{j=1}^{m} \Omega^j \,, \tag{3.1}$$

with the j-th subset Ω^j having area A^j and volume fraction $c^j = (A^j/A)$.

Note that the discretization of the UC in subsets is performed ensuring that each subset is homogeneous, thus, it contains only one of the constituents. Concerning the material response at the microscale, it is assumed that the UC constituents are characterized by a nonlinear behavior. Different kind of inelastic material models can be adopted. Here is only assumed that the considered small strain plasticity model admits a decomposition in elastic and inelastic parts:

$$\boldsymbol{\varepsilon}^j = \boldsymbol{\varepsilon}_e^j + \boldsymbol{\pi}^j \,, \tag{3.2}$$

with $\boldsymbol{\varepsilon}^j$ being the total strain, $\boldsymbol{\varepsilon}_e^j$ being the elastic strain and $\boldsymbol{\pi}^j$ the inelastic strain in the subset Ω^j.

It is assumed that the inelastic strain $\boldsymbol{\pi}^j$ (eigenstrain) is uniform, i.e. constant, within each subset Ω^j leading to the piecewise uniform TFA (PWUFTA) [23].

Taking into account equation (2.9), the total strain $\boldsymbol{\varepsilon}^j$ in the subset Ω^j is the sum of the average strain $\mathbf{E}$ and the periodic fluctuation $\hat{\boldsymbol{\varepsilon}}^j$, that can be written as:

$$\hat{\boldsymbol{\varepsilon}}^j(\boldsymbol{x}) = \boldsymbol{e}^j(\boldsymbol{x}) + \boldsymbol{p}^j(\boldsymbol{x}), \tag{3.3}$$

where the fluctuation strain $\boldsymbol{e}^j(\boldsymbol{x})$ is the effect of the prescribed macroscopic strain $\mathbf{E}$ arising in each subset Ω^j and the fluctuation strain $\boldsymbol{p}^j(\boldsymbol{x})$ is the effect of the piecewise uniform distribution of the inelastic strains alternately acting in all the subsets defined by the discretization of Ω.

The fluctuation strain $\boldsymbol{e}^j(\boldsymbol{x})$ arising in the subset Ω^j, due to the macroscopic strain $\mathbf{E}$, results:

$$\boldsymbol{e}^j(\boldsymbol{x}) = \mathbf{L}^j_{\mathbf{E}}(\boldsymbol{x})\mathbf{E}, \tag{3.4}$$

where $\mathbf{L}^j_{\mathbf{E}}$ is a 3×3 localization matrix.

Collecting the inelastic strains $\boldsymbol{\pi}^s = \{\pi^s_{11}, \pi^s_{22}, \pi^s_{12}\}^T$, defined in the subsets Ω^s with $s = 1, .., m$, in a unique vector $\boldsymbol{\Pi} = \left\{\boldsymbol{\pi}^1, ..., \boldsymbol{\pi}^m\right\}^T$, the fluctuation strain $\boldsymbol{p}^j(\boldsymbol{x})$ arising in each subset Ω^j, is:

$$\boldsymbol{p}^j(\boldsymbol{x}) = \mathbf{L}^j_{\pi}(\boldsymbol{x})\boldsymbol{\Pi}, \tag{3.5}$$

with $\mathbf{L}^j_{\pi}$ the $3 \times 3m$ localization matrix of the piecewise uniform distribution of inelastic strains.

Due to equation (3.3), the total fluctuation strain in the j-th subset is finally obtained as the sum of the effects of the macroscopic strain $\mathbf{E}$ and of the inelastic strain $\boldsymbol{\Pi}$:

$$\hat{\boldsymbol{\varepsilon}}^j(\boldsymbol{x}) = \mathbf{L}^j_{\mathbf{E}}(\boldsymbol{x})\mathbf{E} + \mathbf{L}^j_{\pi}(\boldsymbol{x})\boldsymbol{\Pi}. \tag{3.6}$$

Following equation (3.6), the average fluctuation strain $\bar{\hat{\boldsymbol{\varepsilon}}}^j$ in the subset Ω^j is:

$$\bar{\hat{\boldsymbol{\varepsilon}}}^j = \bar{\mathbf{L}}^j_{\mathbf{E}}\mathbf{E} + \bar{\mathbf{L}}^j_{\pi}\boldsymbol{\Pi}, \tag{3.7}$$

with the average localization operators defined as:

$$\bar{\mathbf{L}}^j_{\mathbf{E}} = \frac{1}{A^j}\int_{\Omega^j} \mathbf{L}^j_{\mathbf{E}} dA, \quad \bar{\mathbf{L}}^j_{\pi} = \frac{1}{A^j}\int_{\Omega^j} \mathbf{L}^j_{\pi} dA. \tag{3.8}$$

A total amount of m matrices $\bar{\mathbf{L}}^j_{\mathbf{E}}$ and m matrices $\bar{\mathbf{L}}^j_{\pi}$ have to be defined and computed. The construction of the aforementioned localization matrices is performed developing an offline stage, namely the *precomputations*, according the following scheme:

- the columns of the matrices $\bar{\mathbf{L}}^j_{\mathbf{E}}$ are obtained running 3 micromechanical elastic analyses. In each solution the UC is subjected to an overall strain $\mathbf{E}$ in which a unit value is assigned to only one of the three macrostrain components. The vector collecting the average local strain in the j-th subset forms a column of the corresponding localization matrix $\bar{\mathbf{L}}^j_{\mathbf{E}}$;

- the columns of the matrices $\bar{\mathbf{L}}_{\pi}^{j}$ are obtained running $3 \times m$ micromechanical linear elastic analyses. In each solution, a unit component of the inelastic strain is assigned to a single subset Ω^j, hence, a unit value is assigned to only one of the $3 \times m$ inelastic strain components in $\mathbf{\Pi}$, under the assumption of null average strain in the UC ($\mathbf{E} = \mathbf{0}$). The vector collecting the average total strain in the j-th subset forms a column of the corresponding localization matrix $\bar{\mathbf{L}}_{\pi}^{j}$.

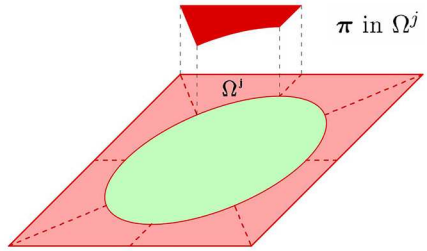

FIGURE 3.1: PWUTFA preanalyses: UC decomposition in subsets Ω^j in which the inelastic strain is assumed uniform.

3.2 PWUTFA in elastoplasticity with linear hardening

Although different kind of inelastic material models can be adopted, the classical associated Mises plasticity [57] is herein considered.
The stress-strain relation for the plastic material is written as:

$$\boldsymbol{\sigma} = \mathbf{C}\left(\boldsymbol{\varepsilon} - \boldsymbol{\pi}\right), \tag{3.9}$$

with $\mathbf{C}$ being a 3×3 elastic matrix, function of the position vector $\boldsymbol{x}$ because of the heterogeneity of Ω, and $\boldsymbol{\pi}$ being the inelastic strain due to the plastic response. The Mises yield criterion, accounting for isotropic hardening, is considered; thus, the elastic region is defined by the activation function:

$$f = q - \sigma_y - K\alpha, \tag{3.10}$$

where σ_y is the yield stress, K is the isotropic hardening parameter, the von Mises stress $q = \sqrt{\frac{3}{2}}\|\bar{\boldsymbol{\sigma}}'\|$, with $\boldsymbol{\sigma}'$ being the deviatoric stress, can be rewritten as:

$$q = \sqrt{\frac{3}{2}\boldsymbol{\sigma}^T \mathbf{M} \boldsymbol{\sigma}} \qquad \text{where } \mathbf{M} = \frac{1}{3}\begin{bmatrix} 2 & -1 & 0 \\ -1 & 2 & 0 \\ 0 & 0 & 6 \end{bmatrix}, \tag{3.11}$$

and α is a time dependent function describing the amount of accumulated plastic strain:

$$\alpha = \int_0^t \|\dot{\boldsymbol{\pi}}\| dt. \tag{3.12}$$

The equations governing the evolution of the plastic strain and of the accumulated plastic strain are:

$$\dot{\boldsymbol{\pi}} = \dot{\gamma}\frac{\partial f}{\partial \boldsymbol{\sigma}}, \qquad \dot{\alpha} = \dot{\gamma}, \tag{3.13}$$

with $\dot{\gamma}$ being the plastic multiplier. The following relations, usually known as Kuhn-Tucker conditions, are introduced for the evaluation of the plastic multiplier:

$$\dot{\gamma} \geq 0, \qquad f \leq 0, \quad \dot{\gamma} f = 0. \tag{3.14}$$

The plastic multiplier $\dot{\gamma}$ is evaluated via the consistency condition:

$$\dot{\gamma}\dot{f} = 0. \tag{3.15}$$

3.2.1 Numerical procedure

With the localization matrices $\bar{\mathbf{L}}^j_{\mathbf{E}}$ and m $\bar{\mathbf{L}}^j_{\pi}$ computed during the offline stage, and after the definition of the nonlinear constitutive law for the elastoplastic material (here Mises plasticity with isotropic hardening is considered, see equations (3.9) - (3.15)), it is possible to evaluate the average stress $\bar{\boldsymbol{\sigma}}^j$ in each subset, which i sassumed governing the evolution of the inelastic strain $\boldsymbol{\pi}^j$.
The time integration of the evolutive problem is performed adopting a Backward Euler implicit scheme.
At the beginning of each time step a macroscopic strain $\mathbf{E}$ is prescribed and a predictor-corrector approach is used to determine the unknowns; the history variables defined at the previous time step are considered as frozen:

$$\boldsymbol{\Pi} = \boldsymbol{\Pi}_n, \quad \boldsymbol{\alpha} = \boldsymbol{\alpha}_n, \tag{3.16}$$

where $\boldsymbol{\alpha}$ is the m component vector of the average accumulated plastic strain in each subset of the domain discretization. Then, the trial state is calculated for all the subsets Ω^j with $j = 1, .., m$, as:

$$\bar{\hat{\boldsymbol{\varepsilon}}}^j = \bar{\mathbf{L}}^j_{\mathbf{E}}\mathbf{E} + \bar{\mathbf{L}}^j_{\pi}\boldsymbol{\Pi} \tag{3.17}$$

$$\bar{\boldsymbol{\sigma}}^j = \mathbf{C}^j\left(\mathbf{E} + \bar{\hat{\boldsymbol{\varepsilon}}} - \boldsymbol{\pi}^j\right) \tag{3.18}$$

$$f^j = \sqrt{\frac{3}{2}}\|\bar{\boldsymbol{\sigma}}'^j\| - \sigma_y - K\alpha^j\,. \tag{3.19}$$

If, for all the activation functions, it results $f^j \leq 0$, the step is elastic and the trial state is solution of the micromechanical problem. On the contrary, if $f^j > 0$ at least for one subset Ω^j, the step is plastic and a correction phase is needed; to this end, equations (3.17), (3.18), (3.19) and the inelastic strain evolution equation (3.13), in the finite time step, are rewritten in residual form in each subset as:

$$\mathbf{r}^j_{\varepsilon} = \bar{\hat{\boldsymbol{\varepsilon}}} - \bar{\mathbf{L}}^j_{\mathbf{E}}\mathbf{E} - \bar{\mathbf{L}}^j_{\pi}\boldsymbol{\Pi} = \mathbf{0} \tag{3.20}$$

$$\mathbf{r}^j_{\sigma} = \bar{\boldsymbol{\sigma}}^j - \mathbf{C}^j\left(\mathbf{E} + \bar{\hat{\boldsymbol{\varepsilon}}} - \boldsymbol{\pi}^j\right) = \mathbf{0} \tag{3.21}$$

$$\mathbf{r}^j_{\pi} = \boldsymbol{\pi}^j - \boldsymbol{\pi}^j_n - \Delta\gamma^j\frac{\partial f^j}{\partial \bar{\boldsymbol{\sigma}}^j} = \mathbf{0} \tag{3.22}$$

$$r^j_f = \left\langle \sqrt{\frac{3}{2}}\|\bar{\boldsymbol{\sigma}}'^j\| - \sigma_y - K(\alpha^j_n + \Delta\gamma^j)\right\rangle_+ = 0\,, \tag{3.23}$$

where the Macaulay brackets $\langle\cdot\rangle_+$ denote the positive part of the number. This is a system of $(3+3+3+1)\times m$ nonlinear equations that is solved via Newton-Raphson method with a return-mapping technique [58] considering $\bar{\hat{\boldsymbol{\varepsilon}}}$, $\bar{\boldsymbol{\sigma}}^j$, $\bar{\boldsymbol{\pi}}^j$ and $\Delta\gamma^j$ with $j = 1, .., m$ as unknowns. Introducing the residual vector $\mathbf{R} = \left\{(\mathbf{r}^1)^T\ (\mathbf{r}^2)^T\ ...\ (\mathbf{r}^m)^T\right\}^T$ and the unknowns vector $\mathbf{S} = \left\{(\mathbf{s}^1)^T\ (\mathbf{s}^2)^T\ ...\ (\mathbf{s}^m)^T\right\}^T$ with $\mathbf{r}^j = \left\{(\mathbf{r}^j_{\varepsilon})^T\ (\mathbf{r}^j_{\sigma})^T\ (\mathbf{r}^j_{\pi})^T\ (r^j_f)^T\right\}^T$ and $\mathbf{s}^j = \left\{(\bar{\hat{\boldsymbol{\varepsilon}}})^T\ (\bar{\boldsymbol{\sigma}}^j)^T\ (\boldsymbol{\pi}^j)^T\ \Delta\gamma^j\right\}^T$, for $j = 1, .., m$, the linearized form of the problem, at the $k+1$-th iteration, leads to the updated increment of the unknowns at the iteration $k+1$:

$$\Delta\mathbf{S}_{(k+1)} = \Delta\mathbf{S}_{(k)} - \left(\left[\frac{\partial\mathbf{R}}{\partial\mathbf{S}}\right]_{(k)}\right)^{-1}\mathbf{R}_{(k)} \tag{3.24}$$

The iterative procedure stops when the norm of the residual vector is lower that a prefixed tolerance. It can be remarked that for the elastic subsets, where

the activation function is lower than zero, equation (3.23) becomes trivial, thus, the solver algorithm have to properly take into account this eventuality [23].

Chapter 4

The PWUHS Reduced Order Model

In this Chapter the PWUHS technique is introduced. It is a Reduced Order Model combining the Hashin-Shtrikman analytical homogenization scheme and a FE^2-like computational homogenization approach, thus, it can be regarded as a hybrid homogenization approach. In the following, both the theoretical aspects and the numerical procedure are illustrated. The homogenization procedure is applied to microstructures characterized by nonlinear stress-strain relationships: plasticity with isotropic hardening and power-law plasticity are considered. Numerical results are shown for different periodic RVEs.

4.1 General Idea

The PWUHS is a ROM which aim is to solve the micromechanical problem with a reasonable computational burden. To this end, similarly to the TFA, the RVE domain Ω is assumed to be divided in a low number m of *subsets* Ω^j with $j = 1, .., m$, according to 3.1.
Each subset is considered containing only one of the constituents, thus, a piecewise representation of the stresses is assumed, allowing for a independent approximation over each region.

In the framework of HS homogenization, as seen in the analytical approach proposed by Hashin and Shtrikmann [4, 5] and illustrated in section 2.5.1.2, an elastic and homogeneous reference material, characterized by an elasticity matrix $\mathbf{C}_0$, is introduced. To associate the reference material to the heterogeneous

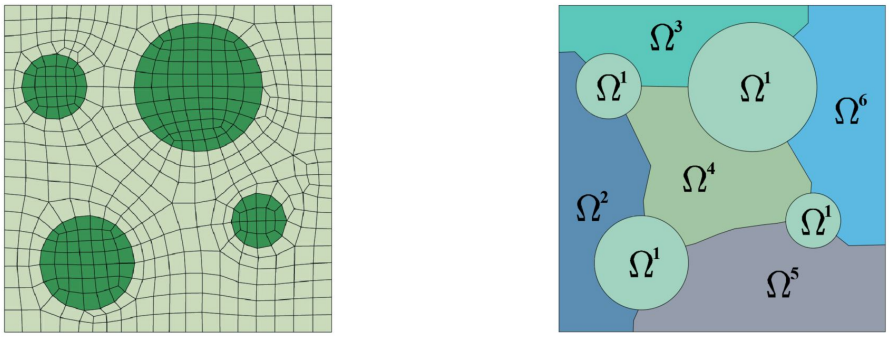

FIGURE 4.1: Computational RVE with circular inclusions: comparison between FE discretization (left) and division in subsets (right).

material, the *polarization stress* $\boldsymbol{\tau}^j$ in the subset Ω^j, is defined:

$$\boldsymbol{\tau}^j(\boldsymbol{x}) = \boldsymbol{\sigma}^j(\boldsymbol{x}) - \mathbf{C}_0\,\boldsymbol{\varepsilon}^j(\boldsymbol{x}), \tag{4.1}$$

where $\boldsymbol{\sigma}^j(\boldsymbol{x}, \boldsymbol{\varepsilon})$ is assumed following a nonlinear stress-strain relationship according to an elasto-plastic constitutive law.
This means that the polarization stress represents the stress gap between the heterogeneous material and the elastic homogeneous reference material, due not only to the difference in terms of stiffness between the real material and the reference one, but also to the inelastic phenomena occurring in the nonlinear material.
It is assumed that the polarization stress $\boldsymbol{\tau}^j$ (an eigenstress) is uniform, i.e. constant, in each subset, representing its average value in Ω^j. This assumption leads to the piecewise uniform HS (PWUHS) approach [33]. Averaging the polarization stress (4.1) and the stresses $\boldsymbol{\sigma}^j(\boldsymbol{x}, \boldsymbol{\varepsilon})$ in the subsets, taking into account equation (2.9) and (3.9), it results:

$$\bar{\boldsymbol{\tau}}^j = \bar{\boldsymbol{\sigma}}^j - \mathbf{C}_0\,(\mathbf{E} + \bar{\hat{\boldsymbol{\varepsilon}}}^j) \tag{4.2}$$

$$\bar{\boldsymbol{\sigma}}^j = \mathbf{C}^j\left(\mathbf{E} + \bar{\hat{\boldsymbol{\varepsilon}}} - \boldsymbol{\pi}^j\right). \tag{4.3}$$

Collecting the polarization stresses $\boldsymbol{\tau}^s = \{\tau^s_{11}, \tau^s_{22}, \tau^s_{12}\}^T$, defined in the subsets Ω^s with $s = 1, .., m$, in a unique vector $\mathbf{T} = \left\{\bar{\boldsymbol{\tau}}^1, ..., \bar{\boldsymbol{\tau}}^m\right\}^T$, the periodic fluctuation strain $\hat{\boldsymbol{\varepsilon}}^j$, arising in each subset Ω^j, is:

$$\hat{\boldsymbol{\varepsilon}}^j(\boldsymbol{x}) = \boldsymbol{\Gamma}^j(\boldsymbol{x})\mathbf{T}, \tag{4.4}$$

where $\mathbf{\Gamma}^j$ is the $3 \times 3m$ localization matrix due to the subset-wise uniform distribution of the polarization stresses. The average strain fluctuation field can be obtained by averaging the terms in equation (4.4), resulting:

$$\bar{\hat{\boldsymbol{\varepsilon}}}^j = \bar{\mathbf{\Gamma}}^j \mathbf{T} \qquad \text{with } \bar{\mathbf{\Gamma}}^j = \frac{1}{A^j} \int_{\Omega^j} \mathbf{\Gamma}^j(\boldsymbol{x}) dA \,. \tag{4.5}$$

being $\bar{\mathbf{\Gamma}}^j$ the average localization matrix.

The construction of the aforementioned localization matrix $\bar{\mathbf{\Gamma}}^j$ is performed developing an offline stage.

The columns of the matrices $\bar{\mathbf{\Gamma}}^j$ are obtained running $3 \times m$ micromechanical elastic analyses on the homogeneous *reference material*. In each solution, a unit component of the polarizaton stress is assigned to a single subset Ω^j; a unit value is assigned to only one of the $3 \times m$ polarization stress components in $\mathbf{T}$. The vectors collecting the average strain fluctuations in the j-th subset due to the polarization stress in Ω^s with $s = 1, .., m$, form the columns of the corresponding localization matrix $\bar{\mathbf{\Gamma}}^j$.

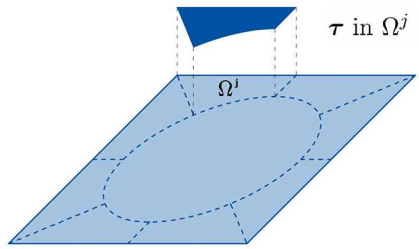

FIGURE 4.2: PWUHS preanalyses: UC decomposition in subsets Ω^j in which the polarization stress is assumed uniform.

4.2 Choice of the reference stiffnes matrix $\mathbf{C}_0$

The PWUHS is formulated introducing a reference material, characterized by a suitable elastic stiffness matrix $\mathbf{C}_0$, whose choice represents a crucial point. Typically, the Hashin-Strickman theory assumes the matrix or the inclusion as reference material. Of course, different choices can be done for the reference material, that can significantly influence the effectiveness of the PWUHS approach described above. A rational choice is to assume the homogenized material as the reference material, i.e. $\mathbf{C}_0 = \bar{\mathbf{C}}$, where $\bar{\mathbf{C}}$ is the overall elastic matrix of the

composite material. Several different techniques can be adopted to derive the homogenized properties of the material. A very simple possibility is to consider the elastic matrix derived by the Voigt homogenization theory [44, 59], which evaluates the equivalent elastic matrix assuming an homogeneous strain field throughout the composite material components.

It is well-known that the evaluation of the homogenized elastic matrix derived by the Voigt theory could be quite inaccurate and more satisfactory techniques can be adopted to determine $\bar{\mathbf{C}}$. In fact, a further and, maybe, efficient possible choice is to evaluate the overall elasticity matrix $\bar{\mathbf{C}}$ of the composite material using numerical techniques, such as the finite element method. In such a case, the overall elasticity matrix is evaluated averaging the stress components when the composite is subjected to an average strain. In particular, the three columns of $\bar{\mathbf{C}}$ are computed prescribing the overall strain $\mathbf{E} = \{1\,0\,0\}^T$, $\mathbf{E} = \{0\,1\,0\}^T$ and $\mathbf{E} = \{0\,0\,1\}^T$, respectively. For the PWUHS reduced order model, the three precomputations needed to assemble $\bar{\mathbf{C}}$ are added to the precomputations required to derive the localization matrices $\bar{\mathbf{\Gamma}}^j$.

Using the homogenized elastic matrix for the reference material allows to derive the response of the composite, activating a polarization field characterized by null average in the UC. When inelastic strains arise in the material the polarization field looses its property of null average, thus a different evaluation of the homogenized elastic matrix may be convenient.

4.2.1 Updated secant modulus approach

In order to improve the PWUHS method, new reference material can be defined during the inelasticity evolution, updating the elastic matrix during the nonlinear analysis. To this end, it is convenient to consider an isotropic reference material, as shown in the following. When the homogenized material, characterized by an overall elastic matrix $\bar{\mathbf{C}}$, is non isotropic, the reference material can be obtained considering an isotropic material with elastic properties related to the homogenized ones. A possible procedure to derive the elasticity matrix of the isotropic reference material $\mathbf{C}_0$ from a homogenized non isotropic one $\bar{\mathbf{C}}$ consists in evaluating $\mathbf{C}_0$ as the isotropic matrix closest to $\bar{\mathbf{C}}$. Hence, for the isotropic reference material it is possible to evaluate the elastic modulus E_0, the Poisson's ratio ν_0 and the shear modulus $\mu_0 = E_0/2(1+\nu_0)$, so that the plane

strain elasticity matrix is represented in the form:

$$\mathbf{C}_0 = \mu_0 \begin{bmatrix} \dfrac{1-\nu_0}{1-2\nu_0} & \dfrac{\nu_0}{1-2\nu_0} & 0 \\ \dfrac{\nu_0}{1-2\nu_0} & \dfrac{1-\nu_0}{1-2\nu_0} & 0 \\ 0 & 0 & \dfrac{1}{2} \end{bmatrix}. \tag{4.6}$$

A correction of the elasticity matrix $\mathbf{C}_0$ can be implemented introducing a scaling factor describing the evolution of the shear modulus μ_0 that has to be updated in order to take into account the nonlinearity arising in the material components, according to a secant modulus approach that has been proved to be very efficient [60, 61, 62, 63].

At the typical time step, the updated (secant) value of the overall shear modulus μ_0^t is determined as the ratio of the norm of the deviatoric stress $||\boldsymbol{\Sigma}'||$ and the norm of the deviatoric strain $\|\mathbf{E}'\|$:

$$\mu_0^t = \frac{1}{2}\frac{\|\boldsymbol{\Sigma}'\|}{\|\mathbf{E}'\|}. \tag{4.7}$$

Then, the scaling factor f_0 is introduced as:

$$f_0 = \frac{\mu_0^t}{\mu_0}. \tag{4.8}$$

and the correction of the elastic reference matrix is defined as:

$$\mathbf{C}_0^t = f_0 \mathbf{C}_0. \tag{4.9}$$

representing an evaluation of the secant reference elastic matrix.

The correction strategy affects also the localization matrix obtained in equation (4.5), for the initial reference material. During the precomputations the matrix $\bar{\boldsymbol{\Gamma}}$ is obtained using a value for $\mathbf{C}_0$. The correction in equation (4.9) implies a equivalent rescaling of the localization matrix using the same factor f_0 defined in equation (4.8). Hence, the corrected average localization matrix is obtained as:

$$\bar{\boldsymbol{\Gamma}}^t = \frac{1}{f_0}\bar{\boldsymbol{\Gamma}}. \tag{4.10}$$

4.3 PWUHS in elastoplasticity with linear hardening

After the evaluation of the localization matrices $\bar{\mathbf{\Gamma}}^j$ computed during the pre-computations, and after the definition of the nonlinear constitutive law for the elastoplastic material (here Mises plasticity with isotropic hardening is considered, see equations (3.9)-(3.15)), it is possible to evaluate the average stress $\bar{\boldsymbol{\sigma}}^j$ in each subset, governing the evolution of the inelastic strain $\boldsymbol{\pi}^j$.

4.3.1 Numerical Procedure

A Backward Euler technique is adopted for the time integration of the evolution problem and a predictor-corrector approach is used to solve the time step.
The quantities at the actual time step t_{n+1} are denoted with no pedex while the quantities at the previous time step t_n are denoted with $_n$.
At the beginning of each time step a macroscopic strain $\mathbf{E}$ is prescribed and a predictor-corrector approach is used to determine the unknowns. A trial state is calculated for all the subsets Ω^j with $j = 1, .., m$, evaluating the equations (4.2), (4.5), (3.10) and (4.3), in the unknowns $\bar{\tilde{\boldsymbol{\varepsilon}}}^j$, $\bar{\boldsymbol{\tau}}^j$ and $\bar{\boldsymbol{\sigma}}^j$, with $j = 1, .., m$ and considering the history variables as frozen at the previous time step:

$$\mathbf{\Pi} = \mathbf{\Pi}_n \tag{4.11}$$

$$\boldsymbol{\alpha} = \boldsymbol{\alpha}_n \tag{4.12}$$

$$\bar{\boldsymbol{\tau}}^j = \bar{\boldsymbol{\sigma}}^j - \mathbf{C}_0 \left(\mathbf{E} + \bar{\tilde{\boldsymbol{\varepsilon}}}^j\right) \tag{4.13}$$

$$\bar{\tilde{\boldsymbol{\varepsilon}}}^j = \bar{\mathbf{\Gamma}}^j \mathbf{T} \tag{4.14}$$

$$\bar{\boldsymbol{\sigma}}^j = \mathbf{C}^j \left(\mathbf{E} + \bar{\tilde{\boldsymbol{\varepsilon}}} - \boldsymbol{\pi}^j\right) \tag{4.15}$$

$$f^j = q - \sigma_y - K\alpha^j \tag{4.16}$$

$$q^j = \sqrt{\frac{3}{2}\bar{\boldsymbol{\sigma}}^T \mathbf{M} \bar{\boldsymbol{\sigma}}} \tag{4.17}$$

Note that this trial state cannot be computed at subset level, but it is determined solving the problem involving all the subsets of the discretization. Once the trial stress $\bar{\boldsymbol{\sigma}}^j$ is computed, the value of the activation function is calculated. If, for all the activation functions, it results $f^j \leq 0$ with $j = 1, .., m$, the step is elastic and the trial state is solution of the micromechanical problem. On the contrary, if $f^j > 0$ at least in one subset Ω^j, the step is plastic and a correction phase is needed; to this end, equations (4.2), (4.3), (4.5), (3.13) and (3.10), in

the finite time step, are rewritten in residual form in each subset as:

$$\mathbf{r}_\tau^j = \bar{\boldsymbol{\tau}}^j - \left[\bar{\boldsymbol{\sigma}}^j - \mathbf{C}_0\left(\mathbf{E} + \bar{\hat{\boldsymbol{\varepsilon}}}^j\right)\right] = \mathbf{0} \tag{4.18}$$

$$\mathbf{r}_\sigma^j = \bar{\boldsymbol{\sigma}}^j - \mathbf{C}^j\left(\mathbf{E} + \bar{\hat{\boldsymbol{\varepsilon}}} - \boldsymbol{\pi}^j\right) = \mathbf{0} \tag{4.19}$$

$$\mathbf{r}_\varepsilon^j = \hat{\boldsymbol{\varepsilon}}^j(\boldsymbol{x}) - \boldsymbol{\Gamma}^j(\boldsymbol{x})\mathbf{T} = \mathbf{0} \tag{4.20}$$

$$\mathbf{r}_\pi^j = \boldsymbol{\pi}^j - \boldsymbol{\pi}_n^j - \Delta\gamma^j \frac{\partial f^j}{\partial \bar{\boldsymbol{\sigma}}^j} = \mathbf{0} \tag{4.21}$$

$$r_f^j = \left\langle q^j - \sigma_y - K(\alpha_n^j + \Delta\gamma^j)\right\rangle_+ = 0\,, \tag{4.22}$$

where the Macaulay brackets $\langle\cdot\rangle_+$ denote the positive part of the number. This is a system of $(3+3+3+3+1)\times m$ nonlinear equations that is solved via Newton-Raphson method, introducing the residual and unknowns vectors:

$$\mathbf{R} = \left\{\ (\mathbf{r}^1)^T\ (\mathbf{r}^2)^T\ \cdots\ (\mathbf{r}^m)^T\ \right\}^T, \tag{4.23}$$

$$\mathbf{S} = \left\{\ (\mathbf{s}^1)^T\ (\mathbf{s}^2)^T\ \cdots\ (\mathbf{s}^m)^T\ \right\}^T, \tag{4.24}$$

where:

$$\mathbf{r}^j = \left\{\ (r_\tau^j)^T\ (r_\sigma^j)^T\ (r_\varepsilon^j)^T\ (r_\pi^j)^T\ r_f^j\ \right\}^T, \tag{4.25}$$

$$\mathbf{s}^j = \left\{\ (\bar{\hat{\boldsymbol{\varepsilon}}})^T\ (\bar{\boldsymbol{\tau}}^j)^T\ (\bar{\boldsymbol{\sigma}}^j)^T\ (\boldsymbol{\pi}^j)^T\ \Delta\gamma^j\ \right\}^T. \tag{4.26}$$

The linearized form of the system 4.18-4.22 at the tipycal $k+1$-th iteration, in global form, reads:

$$\mathbf{R}_{(k)} + \left.\frac{\partial \mathbf{R}}{\partial \mathbf{S}}\right|_{(k)} \mathrm{d}\mathbf{S}_{(k+1)} = \mathbf{0}, \tag{4.27}$$

with d$\mathbf{S}$ being the unknowns variation with respect to the k-th iteration.
The extended form of the linearized problem is:

$$\left\{\begin{array}{c}\mathbf{r}^1\\ \\ \mathbf{r}^2\\ \\ \vdots\\ \\ \mathbf{r}^m\end{array}\right\}_{(k)} + \left[\begin{array}{cccc}\frac{\partial \mathbf{r}^1}{\partial \mathbf{s}^1} & \frac{\partial \mathbf{r}^1}{\partial \mathbf{s}^2} & \cdots & \frac{\partial \mathbf{r}^1}{\partial \mathbf{s}^m}\\ \frac{\partial \mathbf{r}^2}{\partial \mathbf{s}^1} & \frac{\partial \mathbf{r}^2}{\partial \mathbf{s}^2} & \cdots & \frac{\partial \mathbf{r}^2}{\partial \mathbf{s}^m}\\ \vdots & & & \\ \cdots & \cdots & \cdots & \cdots\\ \frac{\partial \mathbf{r}^m}{\partial \mathbf{s}^1} & \frac{\partial \mathbf{r}^m}{\partial \mathbf{s}^2} & \cdots & \frac{\partial \mathbf{r}^m}{\partial \mathbf{s}^m}\end{array}\right]_{(k)} \left\{\begin{array}{c}\mathrm{d}\mathbf{s}^1\\ \\ \mathrm{d}\mathbf{s}^2\\ \\ \vdots\\ \\ \mathrm{d}\mathbf{s}^m\end{array}\right\}_{(k+1)} = \left\{\begin{array}{c}\mathbf{0}\\ \\ \mathbf{0}\\ \\ \vdots\\ \\ \mathbf{0}\end{array}\right\}, \tag{4.28}$$

where the j-th component of the unknowns variation vector is:

$$\mathrm{d}\mathbf{s}^j = \left\{ \; (\mathrm{d}\bar{\tilde{\boldsymbol{\varepsilon}}})^T \, (\mathrm{d}\bar{\boldsymbol{\tau}}^j)^T \, (\mathrm{d}\bar{\boldsymbol{\sigma}}^j)^T \, (\mathrm{d}\boldsymbol{\pi}^j)^T \, \mathrm{d}\Delta\gamma^j \; \right\}^T , \tag{4.29}$$

and the explicit form of the components in the $[(13 \times m) \times (13 \times m)]$ tangent matrix is:

$$\frac{\partial \mathbf{r}^j}{\partial \mathbf{s}^l} = \begin{bmatrix} \dfrac{\partial \mathbf{r}^j_\tau}{\partial \bar{\boldsymbol{\tau}}^l} & \dfrac{\partial \mathbf{r}^j_\tau}{\partial \bar{\boldsymbol{\sigma}}^l} & \dfrac{\partial \mathbf{r}^j_\tau}{\partial \bar{\tilde{\boldsymbol{\varepsilon}}}^l} & \dfrac{\partial \mathbf{r}^j_\tau}{\partial \boldsymbol{\pi}^l} & \dfrac{\partial \mathbf{r}^j_\tau}{\partial f^l} \\ \dfrac{\partial \mathbf{r}^j_{\boldsymbol{\sigma}}}{\partial \bar{\boldsymbol{\tau}}^l} & \dfrac{\partial \mathbf{r}^j_{\boldsymbol{\sigma}}}{\partial \bar{\boldsymbol{\sigma}}^l} & \dfrac{\partial \mathbf{r}^j_{\boldsymbol{\sigma}}}{\partial \bar{\tilde{\boldsymbol{\varepsilon}}}^l} & \dfrac{\partial \mathbf{r}^j_{\boldsymbol{\sigma}}}{\partial \pi^l} & \dfrac{\partial \mathbf{r}^j_{\boldsymbol{\sigma}}}{\partial f^l} \\ \dfrac{\partial \mathbf{r}^j_{\boldsymbol{\varepsilon}}}{\partial \bar{\boldsymbol{\tau}}^l} & \dfrac{\partial \mathbf{r}^j_{\boldsymbol{\varepsilon}}}{\partial \bar{\boldsymbol{\sigma}}^l} & \dfrac{\partial \mathbf{r}^j_{\boldsymbol{\varepsilon}}}{\partial \bar{\tilde{\boldsymbol{\varepsilon}}}^l} & \dfrac{\partial \mathbf{r}^j_{\boldsymbol{\varepsilon}}}{\partial \boldsymbol{\pi}^l} & \dfrac{\partial \mathbf{r}^j_{\boldsymbol{\varepsilon}}}{\partial f^l} \\ \dfrac{\partial \mathbf{r}^j_{\boldsymbol{\pi}}}{\partial \bar{\boldsymbol{\tau}}^l} & \dfrac{\partial \mathbf{r}^j_{\boldsymbol{\pi}}}{\partial \bar{\boldsymbol{\sigma}}^l} & \dfrac{\partial \mathbf{r}^j_{\boldsymbol{\pi}}}{\partial \bar{\tilde{\boldsymbol{\varepsilon}}}^l} & \dfrac{\partial \mathbf{r}^j_{\boldsymbol{\pi}}}{\partial \boldsymbol{\pi}^l} & \dfrac{\partial \mathbf{r}^j_{\boldsymbol{\pi}}}{\partial f^l} \\ \dfrac{\partial \mathbf{r}^j_f}{\partial \bar{\boldsymbol{\tau}}^l} & \dfrac{\partial \mathbf{r}^j_f}{\partial \bar{\boldsymbol{\sigma}}^l} & \dfrac{\partial \mathbf{r}^j_f}{\partial \bar{\tilde{\boldsymbol{\varepsilon}}}^l} & \dfrac{\partial \mathbf{r}^j_f}{\partial \boldsymbol{\pi}^l} & \dfrac{\partial \mathbf{r}^j_f}{\partial f^l} \end{bmatrix} . \tag{4.30}$$

The variation of the unknowns are obtained solving the system of equations in (4.28):

$$\begin{Bmatrix} \mathrm{d}\mathbf{s}^1 \\ \mathrm{d}\mathbf{s}^2 \\ \vdots \\ \mathrm{d}\mathbf{s}^m \end{Bmatrix}_{(k+1)} = - \begin{bmatrix} \dfrac{\partial \mathbf{r}^1}{\partial \mathbf{s}^1} & \dfrac{\partial \mathbf{r}^1}{\partial \mathbf{s}^2} & \cdots & \dfrac{\partial \mathbf{r}^1}{\partial \mathbf{s}^m} \\ \dfrac{\partial \mathbf{r}^2}{\partial \mathbf{s}^1} & \dfrac{\partial \mathbf{r}^2}{\partial \mathbf{s}^2} & \cdots & \dfrac{\partial \mathbf{r}^2}{\partial \mathbf{s}^m} \\ \vdots & & & \\ \cdots & \cdots & \cdots & \cdots \\ \dfrac{\partial \mathbf{r}^m}{\partial \mathbf{s}^1} & \dfrac{\partial \mathbf{r}^m}{\partial \mathbf{s}^2} & \cdots & \dfrac{\partial \mathbf{r}^m}{\partial \mathbf{s}^m} \end{bmatrix}^{-1}_{(k)} \begin{Bmatrix} \mathbf{r}^1 \\ \mathbf{r}^2 \\ \vdots \\ \mathbf{r}^m \end{Bmatrix}_{(k)} , \tag{4.31}$$

and the updated increment of the unknowns in the time step, at the iteration $k+1$, is finally obtained:

$$\Delta\mathbf{S}_{(k+1)} = \Delta\mathbf{S}_{(k)} + \mathrm{d}\mathbf{S}_{(k+1)}, \tag{4.32}$$

allowing for a re-evaluation of the residual; the iterative procedure stops when the norm of the residual vector is lower that a prefixed tolerance.
The numerical procedure of the proposed PWUHS scheme is summarized in the pseudo-algorithm 1.

Algorithm 1 PWUHS Homogenization Scheme

- **Offline stage (Precomputations):**

Perform $3 \times m$ elastic analyses, get localization tensors $\bar{\mathbf{\Gamma}}^j$

- **Online stage at the typical time step t:**

1: Assign $\mathbf{E}$

2: With the history variables $\mathbf{\Pi}_n$ and $\boldsymbol{\alpha}_n$ at t_n, a trial state is evaluated in all the subsets via equations (4.11) (prediction)

3: **if** $f^j \leq 0$ for $j = 1, ..., m$ **then**

4: `exit` (elastic step)

5: **else**

6: Get residual $\mathbf{R}$ via equations (4.18)-(4.22) (correction)

7: **if** $|\mathbf{R}| > tol$ **then** (Newton loop)

8: Solve the linearized problem in equation (4.27) and get the variation of the unknows d$\mathbf{S}$ with respect to k-th iteration

9: Update the unknowns $\mathbf{S}$ via equation (4.32); go to line 6 for next iteration

10: **else**

11: store $\bar{\boldsymbol{\sigma}}^j$ and the history variable $\mathbf{\Pi}$ and $\boldsymbol{\alpha}$

12: **end if**

13: update $\mathbf{C}_0$ and $\bar{\mathbf{\Gamma}}^j$ via the secant modulus approach (optional)

14: **end if**

4.3.2 Numerical Results

In this section, some 2D numerical applications are developed to assess the effciency of the presented PWUHS homogenization technique, in the framework of elastoplasticity with history variables.
Due to the periodicity of the material at the microscopic level, a repetitive UC Ω having, for simplicity, a rectangular shape with dimensions $l_1 \times l_2$ and area A is considered subjected to periodic boundary conditions.
Taking into account the average relationship (2.6) and equation (2.9), the periodic part of the displacement gradient must have null average over the domain. This conditions is ensured prescribing the following conditions on the boundary of Ω:

$$\begin{aligned} \hat{\mathbf{u}}(l_1, x_2) &= \hat{\mathbf{u}}(0, x_2) \quad \forall x_2, \\ \hat{\mathbf{u}}(x_1, l_2) &= \hat{\mathbf{u}}(x_1, 0) \quad \forall x_1. \end{aligned} \tag{4.33}$$

Note that, in order to eliminate rigid displacement of the UC, it is necessary (and sufficient) to constrain the displacement of one point of Ω.
In order to get the localization tensors $\bar{\mathbf{\Gamma}}^j$ the precomputations are carried out using the software *FEAP* (Finite Element Analysis Program): $3 \times m$ elastic analyses are performed as illustrated in section 4.1, on the reference material UC; a 2D four-nodes plane strain linear elastic element has been implemented and used for the finite elements mesh.
The online stage of PWUHS homogenization scheme has been both implemented in `Fortran` and MATLAB® languages and two different geometries of the UC, with two possible material properties of the constituents, are considered subjected to prescribed load histories.
The UC's are here studied considering only two subsets corresponding to the material constituents, this means that both the elastic and plastic constituents are discretized in only one subsets.
A simple application adopting a single inclusion UC is followed by a a second application considering a more complex geometry. Two different load cases are considered: a uniaxial loading and a pure shear loading. The homogenized responses are compared to results of nonlinear finite elements micromechanical analyses, considered as reference solutions. A two-dimensional plane strain four-node *quad* elastoplastic element has been implemented to perform the comparison nonlinear analyses in *FEAP*.

Ceramic inclusions in a metal matrix composite

A periodic UC composed by an elastic inclusion embedded in an elasto-plastic matrix [33], denoted by UC-1 and represented in Fig.4.3, is introduced. This UC has dimensions $l_1 = 10\text{mm}$ and $l_2 = 10\text{mm}$ and is characterized by an inclusion volume fractions $c^2 = 0.54$. The constituents material properties reported in Table 4.1, resemble a composite made of stiff ceramics inclusions embedded in a metal plastic matrix.
A low number of elements (104) is used in the FE discretization of the UC, considered in both precomputations and FE reference solution. Please note that with the UC discretized in two subsets Ω^1 and Ω^2, corresponding respectively to the matrix and the inclusion, the number of internal variables in the PWUHS scheme is equal to $2 \times 4 = 8$ (considering the three components of the plastic strain and the accumulated plastic strain), that is much lower in comparison to the internal variables involved in the nonlinear FEA ($4 \times 104 = 416$).
The relative error measure equation (4.34) is introduced to estimate the difference between the macroscopic stress prediction $\boldsymbol{\Sigma}$ and the finite element macroscopic stress $\boldsymbol{\Sigma}^{FE}$:

$$\texttt{err} = \frac{\|\boldsymbol{\Sigma}_t - \boldsymbol{\Sigma}_t^{\text{FE}}\|}{\|\boldsymbol{\Sigma}_t^{\text{FE}}\|}. \tag{4.34}$$

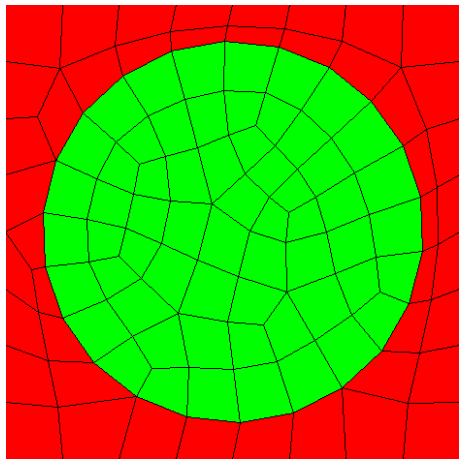

FIGURE 4.3: Single inclusion Microstructure (UC-1).

Two different loading histories are considered. First, the UC is subjected to a monotonic loading history in terms of the average macroscopic strain E_{11}, until

the value of 0.002 (Load Case 1, LC-1) is reached. PWUHS is used to determine the macroscopic stresses to compare with the average stress obtained from a FE micromechanical analysis. The overall nonlinear response of the composite material in terms of the macroscopic stress Σ_{11} versus E_{11} is reported in Fig.4.4. The PWUHS perfectly predicts the microscopic stress response of the composite in the elastic branch. On the contrary, the PWUHS suffer stiffness overprediction in the plastic branch in comparison to the FE solution, disregarding the choice of the reference material elasticity matrix $\mathbf{C}_0$. Indeed, better results are obtained adopting the correction of the reference material, according to the secant modulus approach 4.2.1, as can be observed in Fig. 4.4, even with a low number of subsets.

Since only two subsets are considered in the computations, the results can be sensibly improved adopting a finest subsets discretization as shown in Fig. 4.5.

E^1 [GPa]	ν^1	k [MPa]	σ_y [MPa]	E^2 [GPa]	ν^2
210	0.3	100	300	300	0.25

TABLE 4.1: Material parameters of the ceramic inclusions in a metal matrix composite.

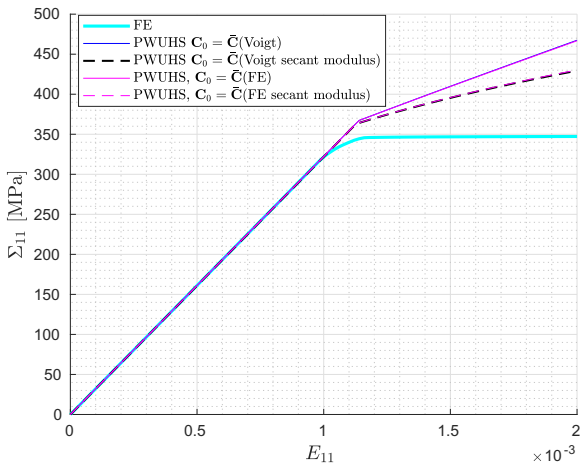

FIGURE 4.4: Macroscopic stress Σ_{11}, UC-1 with parameters in Table 4.1.

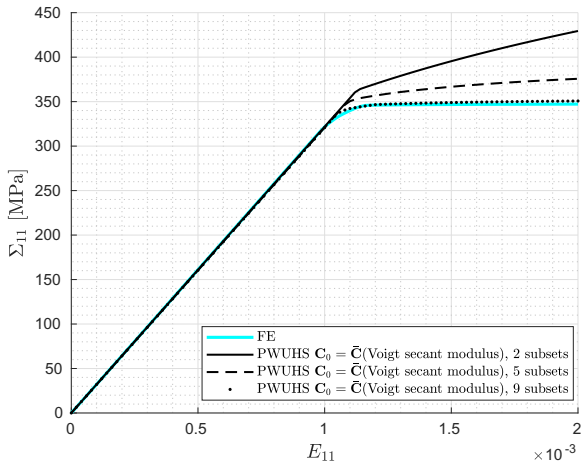

FIGURE 4.5: Macroscopic stress Σ_{11}, UC-1 with parameters in Table 4.1, divided in 2, 5, 9 subsets.

The UC-1 is then subjected to a loading history in terms of the average shear strain Γ_{12} that monotonically increases until the value of 0.01 is reached (Load Case 2, LC-2). In Fig. 4.6, the response of the UC is reported plotting the macroscopic stress component Σ_{12} with respect to the average strain Γ_{12}. This loading history confirms the previous observations regarding the difference with the FE solution. Anyway it can be remarked that computations performed using the proposed secant correction for the reference material leads to a significant improvement of the solution which results, indeed, very close to the FE reference solution, in fact the maximum relative error encountered at the final load step is equal to 0.193 using the computationally derived $\mathbf{C}_0$, 0.191 considering the elasticity matrix calculated according to Voigt. This is due to the similarity between the elastic matrices obtained analytically or numerically with this material properties and constituents volume fractions.

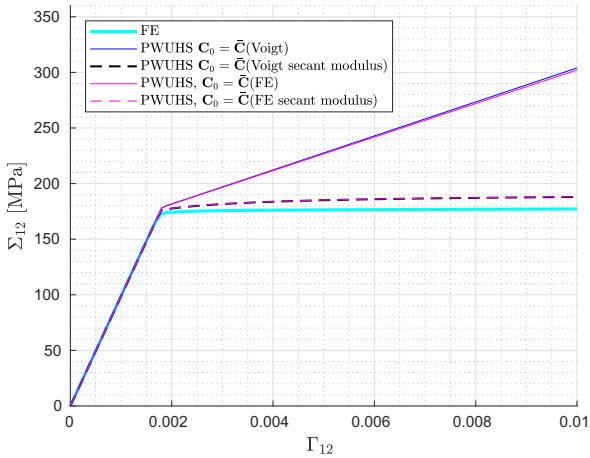

FIGURE 4.6: Macroscopic stress Σ_{12}, UC-1 with parameters in Table 4.1.

Another two dimensional UC is here introduced (UC-2, see Fig. 4.7); it is composed by elastic inclusions embedded in an elasto-plastic matrix and has dimensions $l_1 = 10$mm and $l_2 = 10$mm. In this UC a random distribution of the inclusions is simulated and periodic boundary conditions are applied for the numerical applications.

The volume fractions of the inclusions, corresponding to the sub-domain Ω^2, is $c^2 = 0.12$. With UC-2 discretized in two subsets, the number of internal variable involved in the PWUHS is still $2 \times 4 = 8$ while the internal variables involved in the nonlinear FEA is $4 \times 1214 = 2428$.

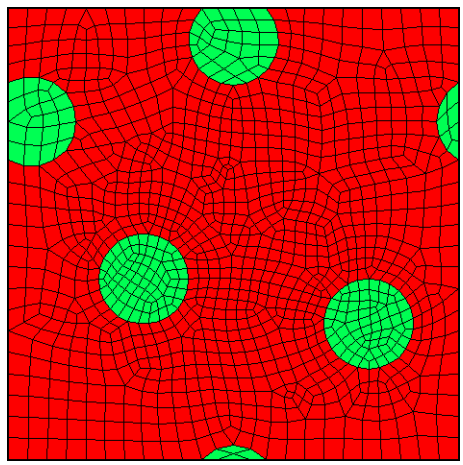

FIGURE 4.7: Periodic Microstructure UC-2.

Also in this application the UC is first subjected to a monotonic extension in x_1 direction (LC-1). The prediction of the macroscopic stress Σ_{11} with respect to E_{11} is reported in Fig.4.8.
In this application the PWUHS gives results close to the reference FE solution, wheter the correction of the reference elasticity matrix in adopted or not. This is due to the reduced volume fraction of the elastic phase that barely affects the overall response of the UC. Despite the coarse subsets division, the ROM technique delivers a good stress approximation disregarding the adopted elasticity matrix of the reference material (with $\mathbf{C_0} = \bar{\mathbf{C}}(FE)$, the maximum errors, obtained with and without the secant correction, are respectively 0.024 and 0.023).

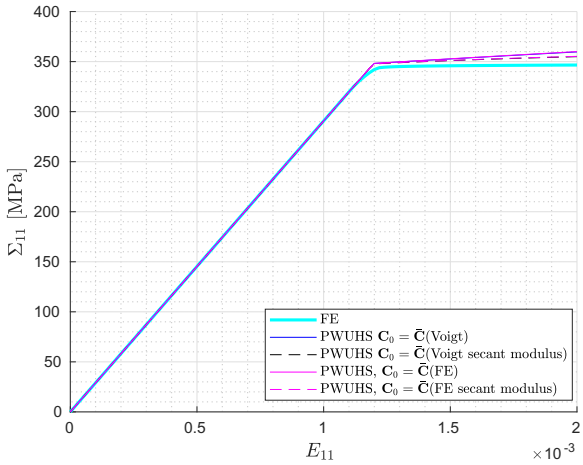

FIGURE 4.8: Macroscopic stress Σ_{11}, UC-2 with parameters in Table 4.1.

UC-2 is then subjected to monotonic shear loading LC-2. The considerations made for the previous application are here confirmed; using the secant correction of $\mathbf{C_0}$ is a big advantage in terms of accuracy, sensibly reducing the error when plasticity occurs.

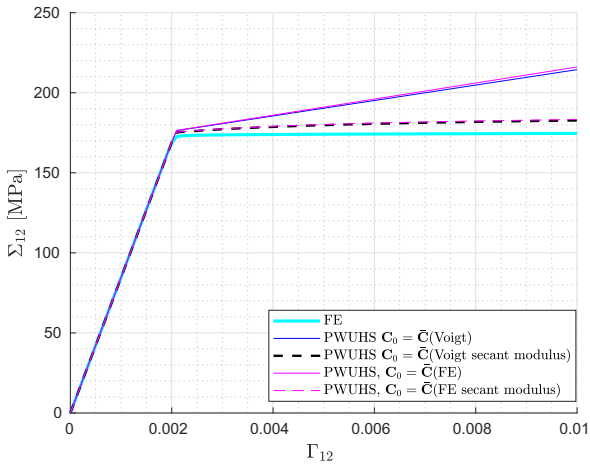

FIGURE 4.9: Macroscopic stress Σ_{12}, UC-2 with parameters in Table 4.1.

Fiber reinforced epoxy resin

The UCs introduced in the previous section are here studied using different material properties which can be traced back to a fiber reinforced epoxy resin composite. The characteristic material properties of the matrix and inclusions, corresponding to the subdomain Ω^1 and Ω^2, are reported in Table 4.2. The aim of these investigations is to understand how a bigger stiffness gap between the material phases affects the accuracy of the proposed PWUHS homogenization scheme.

E^1 [GPa]	ν^1	k [MPa]	σ_y [MPa]	E^2 [GPa]	ν^2
21	0.3	100	30	210	0.25

TABLE 4.2: Material parameters of fiber reinforced epoxy resin composite.

In Figs. 4.10 and 4.11 are respectively reported the macroscopic stress $\Sigma 11$ averaged on UC-1 subjected to the loading history LC-1 and the macroscopic stress $\Sigma 12$ averaged on UC-1 subjected to the loading history LC-2.
With a significant stiffness gap between the constituents, the computationally derived elastic reference matrix delivers a far better stress prediction in comparison to the Voigt derived matrix, especially if a fixed $\mathbf{C_0}$ is considered. If the secant modulus approximation is adopted, the accuracy improvement is relevant disregarding the applied strain. In particular, when LC-2 is applied, the FE

reference shear strain is captured with both the FE $\bar{\mathbf{C}}$ (err= 0.422) and Voigt $\bar{\mathbf{C}}$ (err= 0.664).

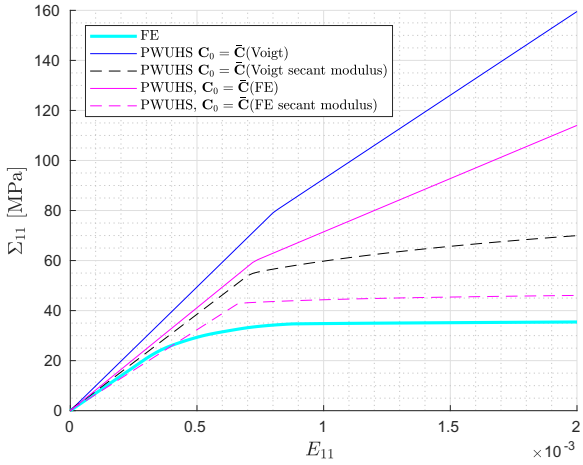

FIGURE 4.10: Macroscopic stress Σ_{11}, UC-1 with parameters in Table 4.2.

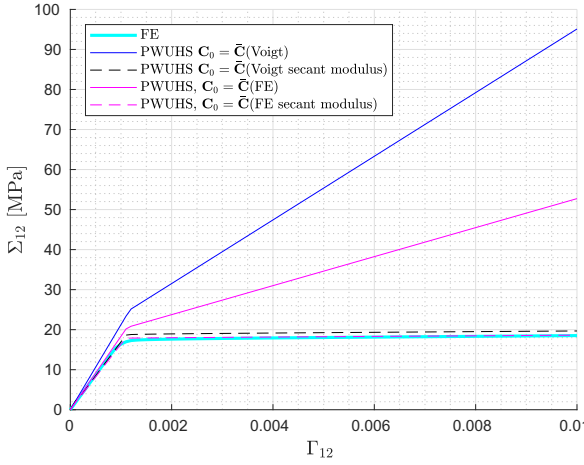

FIGURE 4.11: Macroscopic stress Σ_{12}, UC-1 with parameters in Table 4.2.

In Figs. 4.12 and 4.13 the overall stress-strain relationships for LC-1 and LC-2 are reported for UC-2, respectively. Similar consideration can be made in comparison with the previous applications, confirming the effectiveness of the secant modulus correction and of the numerical reference elasticity matrix.

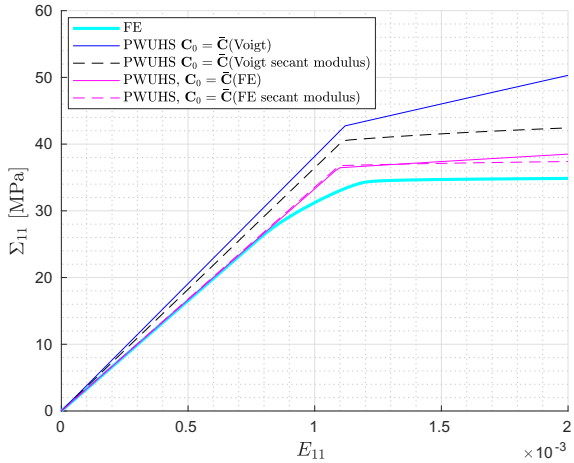

FIGURE 4.12: Macroscopic stress Σ_{11}, UC-2 with parameters in Table 4.2.

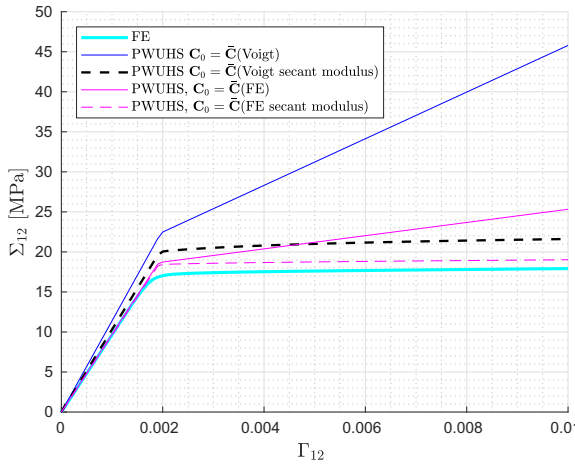

FIGURE 4.13: Macroscopic stress Σ_{12}, UC-2 with parameters in Table 4.2.

Furthermore, the computational time of the PWUHS scheme is compared to that of the FE analyses, considering the applications on UC-2, in Table 4.3. Using the $\mathbf{C_0}$ calculated according to Voigt gives a big advantage in terms of computational time, with a speed-up factor that is the highest, whether the secant modulus approach is considered or not. The numerically derived elastic reference matrix leads to a lower speed-up of the computation but with the higher accuracy.

Load Case	$\mathbf{C_0}$	CPU time FE [s]	PWUHS speed-up
LC-1	$\bar{\mathbf{C}}$ (Voigt)	711.07	4182.76
	$\bar{\mathbf{C}}$ (FE)		582.84
	$\bar{\mathbf{C}}$ (Voigt), secant		1341.64
	$\bar{\mathbf{C}}$ (FE), secant		470.90
LC-2	$\bar{\mathbf{C}}$ (Voigt)	855.31	4072.90
	$\bar{\mathbf{C}}$ (FE)		562.70
	$\bar{\mathbf{C}}$ (Voigt), secant		425.52
	$\bar{\mathbf{C}}$ (FE), secant		409.23

TABLE 4.3: Comparison between FE and PWUHS computational time: UC-2 UC-2 subjected to LC-1 and LC-2.

4.4 PWUHS in elastoplasticity with power law hardening

A very common deformation model with power law hardening is the Ramberg-Osgood law. According to this model, the total strain is obtained as sum of two components as:

$$\boldsymbol{\varepsilon} = \boldsymbol{\varepsilon}_e + \boldsymbol{\varepsilon}_p, \tag{4.35}$$

in which $\boldsymbol{\varepsilon}_e$ is the elastic part of the strain, following the Hooke's law, and $\boldsymbol{\varepsilon}_p$ is the plastic part of the strain. The power-law relation implies that the plastic part of the strain is bigger than zero even for low level of stresses, and is negligible in comparison to the elastic part.
Higher values for the inelastic strain are encountered when the stresses exceed a reference value, namely σ_0.
Ramberg-Osgood relation between stress and strain, having no history variables, reads:

$$\boldsymbol{\varepsilon} = \frac{1}{9\lambda}(\boldsymbol{\sigma} \bullet \mathbf{1})\,\mathbf{1} + \frac{\boldsymbol{\sigma}'}{2\mu} + \frac{3\varepsilon_0}{2}\left(\frac{q}{\sigma_0}\right)^p \frac{\boldsymbol{\sigma}'}{q}, \tag{4.36}$$

where λ and μ are the bulk and shear modulus of the plastic material, ε_0, σ_0, p are constant parameters typical of the material, being respectively the reference strain, reference stress and hardening exponent ($p > 1$).
The von Mises stress $q = \sqrt{\frac{3}{2}}\|\bar{\boldsymbol{\sigma}}'\|$, with $\boldsymbol{\sigma}'$ being the deviatoric stress, can be calculated according to equation (3.11).

Is important to note that the first and second terms in equation (4.36) represent the elastic part of the strain while the third term corresponds to the plastic strain.
This relation cannot be explicited with respect to the stresses but provides a continous curve in the strain field.
According to the subsetswise constant field approximation (3.1), the constitutive law is rewritten as:

$$\boldsymbol{\varepsilon}^j = \frac{1}{9\lambda}\left(\boldsymbol{\sigma}^j \bullet \mathbf{1}\right)\mathbf{1} + \frac{\boldsymbol{\sigma}'^j}{2\mu} + \frac{3\varepsilon_0}{2}\left(\frac{q^j}{\sigma_0}\right)^p \frac{\boldsymbol{\sigma}'^j}{q^j}, \tag{4.37}$$

4.4.1 Numerical Procedure

With the localization matrices $\bar{\mathbf{\Gamma}}^j$ at hand, the nonlinear system of equation to be solved during the online phase is assembled in order to evaluate the average stress $\bar{\boldsymbol{\sigma}}$ in the subsets.
A discrete time discretization is adopted for the evaluation of the *incremental* nonlinear stress-strain relation (4.37), where incremental means that the stress and strain fields are evaluated at the end of each time step, with the implicitly considered internal variables depending on $\boldsymbol{\varepsilon}$.
A Backward Euler technique is adopted for the time integration of the problem and a predictor-corrector approach is used to solve the time step.
At the beginning of each time step a macroscopic strain $\mathbf{E}$ is prescribed and a predictor-corrector approach is used to determine the unknowns.
An elastic prediction of the stress state $\bar{\boldsymbol{\sigma}}^j$ is carried out for all the subsets Ω^j with $j = 1, .., m$, and the additional unknowns $\bar{\hat{\boldsymbol{\varepsilon}}}^j$, $\bar{\boldsymbol{\tau}}^j$ and $\bar{\boldsymbol{\sigma}}^j$, with $j = 1, .., m$, are evaluated via the equations (4.2), (4.5), (4.37):

$$\bar{\boldsymbol{\tau}}^j = \bar{\boldsymbol{\sigma}}^j - \mathbf{C}_0\left(\mathbf{E} + \bar{\hat{\boldsymbol{\varepsilon}}}^j\right) \tag{4.38}$$

$$\bar{\hat{\boldsymbol{\varepsilon}}}^j = \bar{\boldsymbol{\Gamma}}^j \mathbf{T} \tag{4.39}$$

$$\boldsymbol{\varepsilon}^j = \frac{1}{9\lambda}\left(\boldsymbol{\sigma}^j \bullet \mathbf{1}\right)\mathbf{1} + \frac{\boldsymbol{\sigma}'^j}{2\mu} + \frac{3\varepsilon_0}{2}\left(\frac{q^j}{\sigma_0}\right)^p \frac{\boldsymbol{\sigma}'^j}{q^j}, \tag{4.40}$$

The elastic prediction is operated at the global level, solving the problem for all the subsets. Due to the implicit representation of the internal variables, a correction phase is needed at each time step. To this end the equations (4.38), (4.39), (4.40) are rewritten in their residual form in all the subsets:

$$\mathbf{r}_\tau^j = \bar{\boldsymbol{\tau}}^j - \left[\bar{\boldsymbol{\sigma}}^j - \mathbf{C}_0\left(\mathbf{E} + \bar{\hat{\boldsymbol{\varepsilon}}}^j\right)\right] = \mathbf{0} \tag{4.41}$$

$$\mathbf{r}_\sigma^j = \frac{1}{9\lambda}\left(\boldsymbol{\sigma}^j \bullet \mathbf{1}\right)\mathbf{1} + \frac{\boldsymbol{\sigma}'^j}{2\mu} + \frac{3\varepsilon_0}{2}\left(\frac{q^j}{\sigma_0}\right)^p \frac{\boldsymbol{\sigma}'^j}{q^j} - \left(\mathbf{E} + \bar{\hat{\boldsymbol{\varepsilon}}}^j\right) = \mathbf{0} \tag{4.42}$$

$$\mathbf{r}_\varepsilon^j = \hat{\boldsymbol{\varepsilon}}^j(\boldsymbol{x}) - \boldsymbol{\Gamma}^j(\boldsymbol{x})\mathbf{T} = \mathbf{0}. \tag{4.43}$$

A global system of $(3+3+3)\times m$ nonlinear equations is obtained and solved via the Newton-Raphson method. To this end the residual and unknowns vectors (4.23)-(4.24) are introduced, with their components respectively equal to:

$$\mathbf{r}^j = \left\{ \begin{array}{ccc} (r_\tau^j)^T & (r_\sigma^j)^T & (r_\varepsilon^j)^T \end{array} \right\}^T, \tag{4.44}$$

and:

$$\mathbf{s}^j = \left\{ \begin{array}{ccc} (\bar{\hat{\boldsymbol{\varepsilon}}})^T & (\bar{\boldsymbol{\tau}}^j)^T & (\bar{\boldsymbol{\sigma}}^j)^T \end{array} \right\}^T. \tag{4.45}$$

In order to evaluate the unknowns variations vector d$\mathbf{S}$ with respect to the k-th iterations, the linearized form (4.27) of the system 4.41-4.43 at the tipycal $k+1$-th iteration is introduced, with the extended form of the linearized problem equal to equation (4.28).
In the extended form of the linearized problem (4.28), the j-th component of the unknowns variation vector is:

$$\mathrm{d}\mathbf{s}^j = \left\{ \begin{array}{ccc} (\mathrm{d}\bar{\hat{\boldsymbol{\varepsilon}}})^T & (\mathrm{d}\bar{\boldsymbol{\tau}}^j)^T & (\mathrm{d}\bar{\boldsymbol{\sigma}}^j)^T \end{array} \right\}^T, \tag{4.46}$$

and the explicit form of the components in the $[(9 \times m) \times (9 \times m)]$ tangent matrix is:

$$\frac{\partial \mathbf{r}^j}{\partial \mathbf{s}^l} = \begin{bmatrix} \dfrac{\partial \mathbf{r}^j_{\boldsymbol{\tau}}}{\partial \bar{\boldsymbol{\tau}}^l} & \dfrac{\partial \mathbf{r}^j_{\boldsymbol{\tau}}}{\partial \bar{\boldsymbol{\sigma}}^l} & \dfrac{\partial \mathbf{r}^j_{\boldsymbol{\tau}}}{\partial \bar{\tilde{\boldsymbol{\varepsilon}}}^l} \\ \dfrac{\partial \mathbf{r}^j_{\boldsymbol{\sigma}}}{\partial \bar{\boldsymbol{\tau}}^l} & \dfrac{\partial \mathbf{r}^j_{\boldsymbol{\sigma}}}{\partial \bar{\boldsymbol{\sigma}}^l} & \dfrac{\partial \mathbf{r}^j_{\boldsymbol{\sigma}}}{\partial \bar{\tilde{\boldsymbol{\varepsilon}}}^l} \\ \dfrac{\partial \mathbf{r}^j_{\boldsymbol{\varepsilon}}}{\partial \bar{\boldsymbol{\tau}}^l} & \dfrac{\partial \mathbf{r}^j_{\boldsymbol{\varepsilon}}}{\partial \bar{\boldsymbol{\sigma}}^l} & \dfrac{\partial \mathbf{r}^j_{\boldsymbol{\varepsilon}}}{\partial \bar{\tilde{\boldsymbol{\varepsilon}}}^l} \end{bmatrix}. \tag{4.47}$$

The variation of the unknowns are obtained solving the system of equations:

$$\mathrm{d}\mathbf{S}_{(k+1)} = -\left.\frac{\partial \mathbf{R}}{\partial \mathbf{S}}\right|_{(k)} \mathbf{R}_{(k)}, \tag{4.48}$$

and the updated increment of the unknowns in the time step, at the iteration $k+1$ is evaluated as:

$$\Delta\mathbf{S}_{(k+1)} = \Delta\mathbf{S}_{(k)} + \mathrm{d}\mathbf{S}_{(k+1)}. \tag{4.49}$$

The updated residual is evaluated and the iterative procedure continues until the norm of the residual vector is lower than the prescribed tolerance.

4.4.2 Numerical Results

Some numerical applications considering different microstructures, are here reported considering a different stress-strain relationship for the matrix phase: the power law plasticity, introduced in the previous section is assigned to one of the material constituents.
Periodic boundary conditions are assigned to the studied UCs, according to equation (4.33) and, again, the repetitive UCs are discretized in two subsets Ω^1 and Ω^2, corresponding respectively to the matrix and the inclusions.

Ceramic inclusions in a metal matrix composite

The UCs previously introduced in Figs. 4.3 and 4.7 are studied in the following. The constituents material properties of the Ramberg-Osgood matrix Ω^1 and the elastic inclusions Ω^2, are reported in Table 4.4, where the reference strain, the reference stress and the hardening exponent are typical of a metal matrix.

In Fig. 4.14 are reported the curves $\Sigma_{11} - E_{11}$ for loading history LC-1 applied on UC-1. As already seen for Mises plasticity, the PWUHS suffer stiffness over-prediction using both the FE or Voigt elastic reference matrix $\mathbf{C_0}$. A better stress prediction is obtained using the secant modulus correction, however a refinement of the subsets seems to be necessary.
Similar considerations can be made applying LC-2 and plotting the curves $\Sigma_{12} - \Gamma_{12}$, as in Fig. 4.15. The secant correction of the elastic matrix $\mathbf{C_0}$ leads to an excellent stress prediction even with the lowest number of subsets, lowering the error until 0.237 ($\mathbf{C_0} = \bar{\mathbf{C}}$(Voigt)).

E^1 [GPa]	ν^1	p	σ_0 [MPa]	ε_0	E^2 [GPa]	ν^2
210	0.3	5	200	0.001	300	0.25

TABLE 4.4: Material parameters of the elastic inclusion embedded in a power-law hardening plastic matrix.

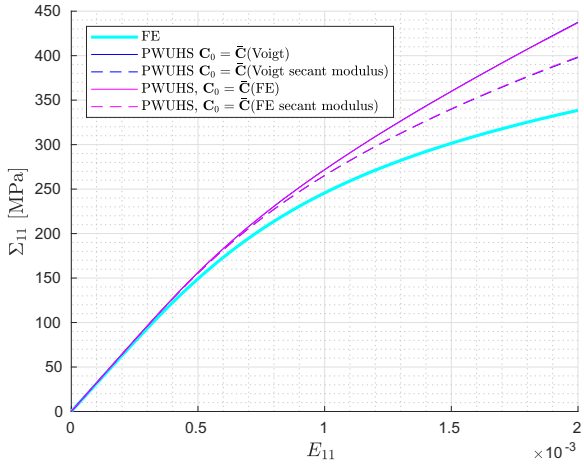

FIGURE 4.14: Macroscopic stress Σ_{11}, UC-1 with parameters in Table 4.4.

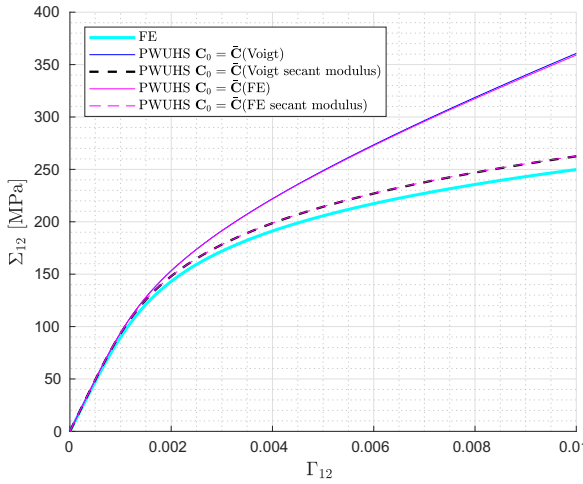

FIGURE 4.15: Macroscopic stress Σ_{12}, UC-1 with parameters in Table 4.4.

The UC-2 in then subjected to monotonic increasing uniaxial strain and the predicted macroscopic stress Σ_{11} is reported in Fig. 4.16. In this case the PWUHS homogenization shows high accuracy even using a fixed $\mathbf{C_0}$, wheter the used elastic reference matrix is analitycally or numerically derived. The larger error is obtained considering a fixed $\mathbf{C_0} = \bar{\mathbf{C}}$(Voigt).

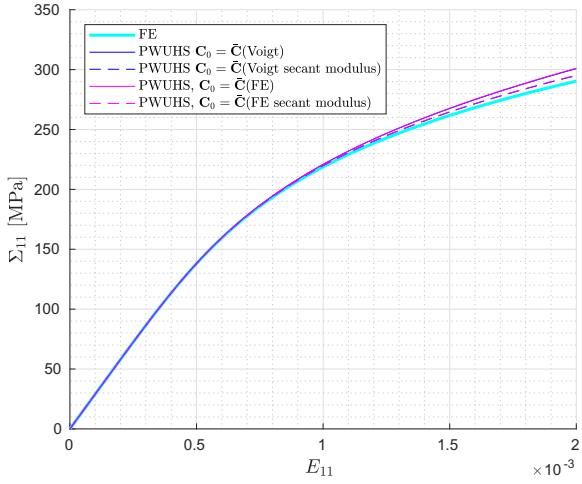

FIGURE 4.16: Macroscopic stress Σ_{11}, UC-2 with parameters in Table 4.4.

When LC-2 is applied to UC-2, a reasonable accuracy is obtained only if the secant modulus correction is implemented, otherwise the error increases until

the maximum value of 0.888 ($\mathbf{C_0} = \bar{\mathbf{C}}$, Voigt).

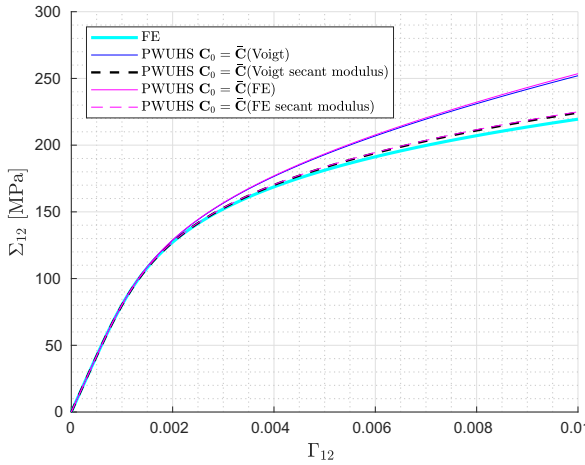

FIGURE 4.17: Macroscopic stress Σ_{12}, UC-2 with parameters in Table 4.4.

In order to understand how a change in the elastic constituents volume fraction affects the accuracy of the proposed PWUHS, a third UC, namely UC-3 (see Fig. 4.18) is introduced.
This UC has an elastic phase volume fraction $c^2 = 0.28$ and is divided in two subsets corresponding to the constituents. The results of the PWUHS are compared to the reference FE solution obtained discretizing the geometry in 1230 elements.

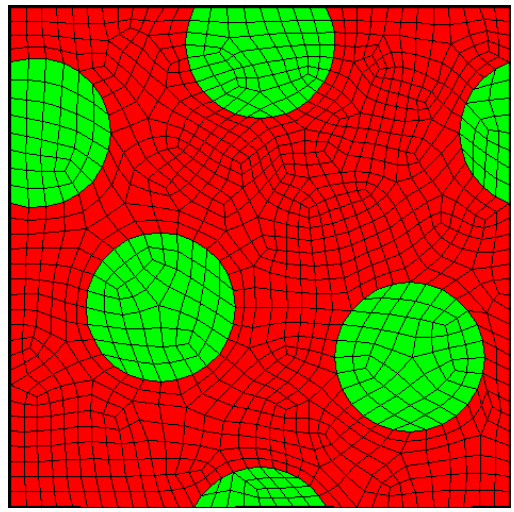

FIGURE 4.18: Periodic Microstructure UC-3.

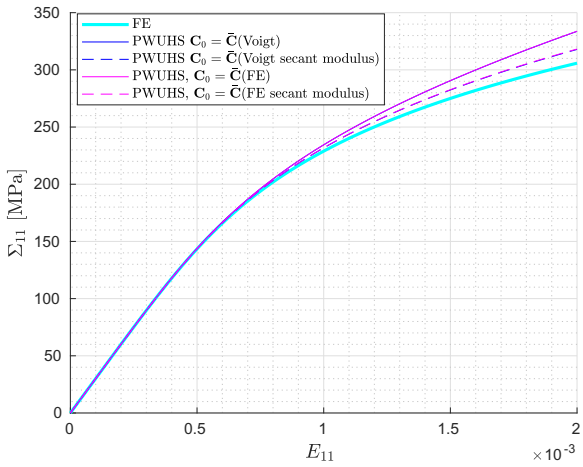

FIGURE 4.19: Macroscopic stress Σ_{11}, UC-3 with parameters in Table 4.4.

In Figs. 4.19 and 4.20 are respectively reported the curves $\Sigma_{11} - E_{11}$ for loading history LC-1 and $\Sigma_{12} - \Gamma_{12}$ for LC-2 on UC-3.
In comparison with the results obtained considering UC-2, the accuracy is generally lower, confirming that the elastic phase volume fraction influences the average response of the UC, causing an overprediction of the overall stiffness. Furthermore, the secant modulus approach confirms its efficiency, always leading to a drastical reduction of the error.

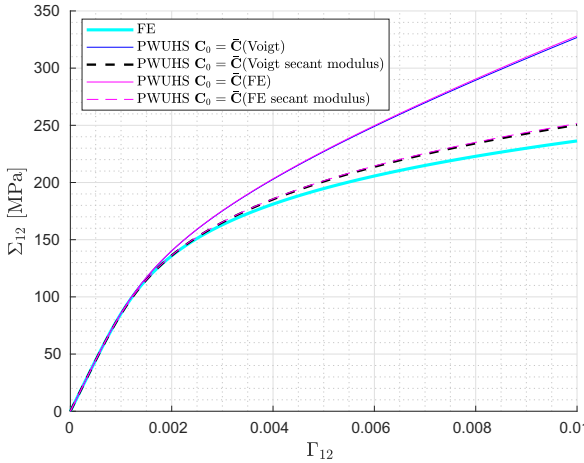

FIGURE 4.20: Macroscopic stress Σ_{12}, UC-3 with parameters in Table 4.4.

Fiber reinforced epoxy resin

The UCs composed by elastic inclusions and a Ramberg-Osgood matrix are also studied with material properties tipycal of a fiber reinforced epoxy resin, as reported in Table 4.5.

E^1 [GPa]	ν^1	p	σ_0 [MPa]	ε_0	E^2 [GPa]	ν^2
21	0.3	5	20	0.001	210	0.25

TABLE 4.5: Material parameters of the elastic inclusions embedded in a power-law hardening plastic matrix.

UC-1 is again subjected to the loading histories LC-1 and LC-2 and the respective curves $\Sigma_{11} - E_{11}$ and $\Sigma_{12} - \Gamma_{11}$ are reported in Figs. 4.21 and 4.22. As already seen in Figs. 4.10 and 4.11, when LC-1 is considered, PWUHS evidently lacks of accuracy, but if power law plasticity is considered, even the secant modulus correction is uneffective. On the other hand the $\mathbf{C_0}$ correction delivers a good prediction of the shear stress when LC-2 is applied (see Fig. 4.22).

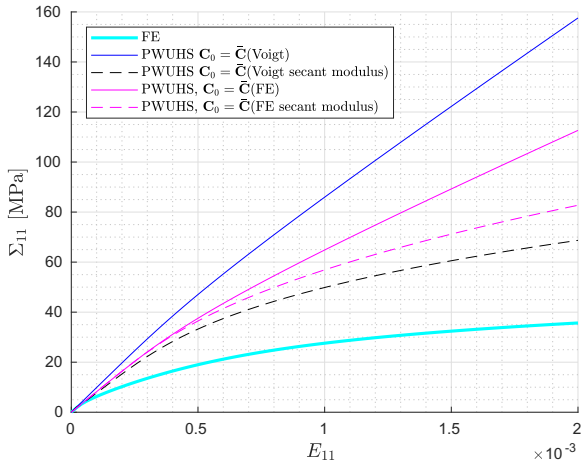

FIGURE 4.21: Macroscopic stress Σ_{11}, UC-1 with parameters in Table 4.5.

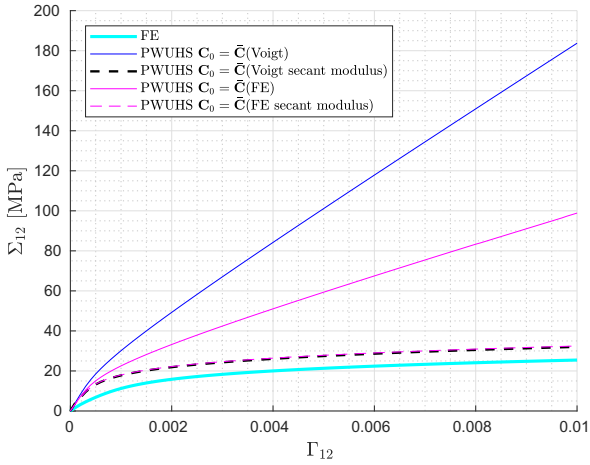

FIGURE 4.22: Macroscopic stress Σ_{12}, UC-1 with parameters in Table 4.5.

Considering UC-2, hence, lowering the volume fraction of the elastic constituents, the PWUHS allows for a stress prediction close to the reference FE solution as long as the secant modulus approach is applied to the numerical reference elastic matrix $\bar{\mathbf{C}}(FE)$, as reported in Fig. 4.23 for LC-1 and Fig. 4.24 for LC-2.

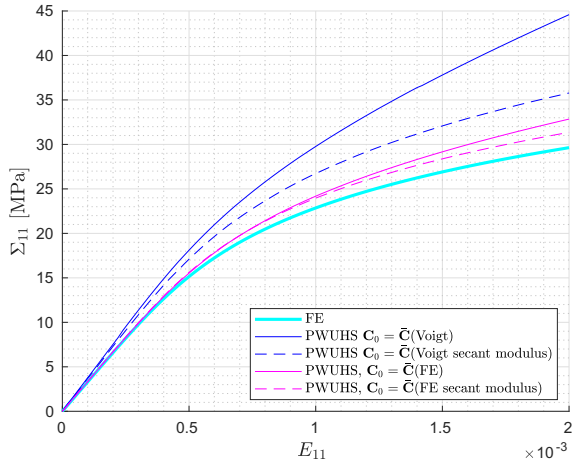

FIGURE 4.23: Macroscopic stress Σ_{11}, UC-2 with parameters in Table 4.5.

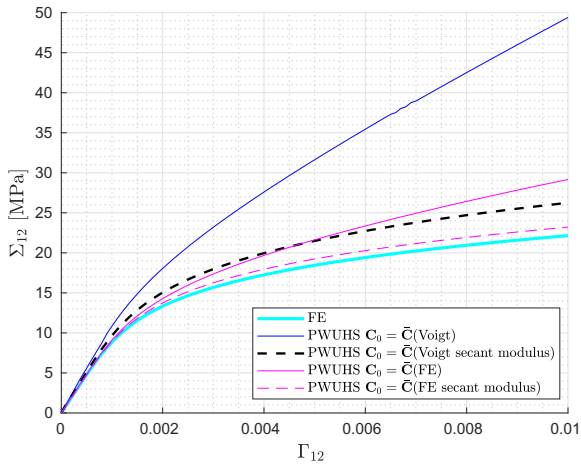

FIGURE 4.24: Macroscopic stress Σ_{12}, UC-2 with parameters in Table 4.5.

Similar consideration can be made considering the UC-3, having a slightly higher elastic volume fraction in comparison to UC-2, exposed to a uniaxial loading (Fig. 4.25) and a shear loading (Fig. 4.26). The secant modulus approach is confirmed to be a fundamental tool in lowering the error in comparison to the FE solution. A reasonable macroscopic stress prediction is obtained with no need of an higher number of subsets. Anyway, in the following section, the perfomances of the PWUHS scheme are illustrated with an increasing number of subsets, in order to find a resonable equilibrium between computational cost and accuracy.

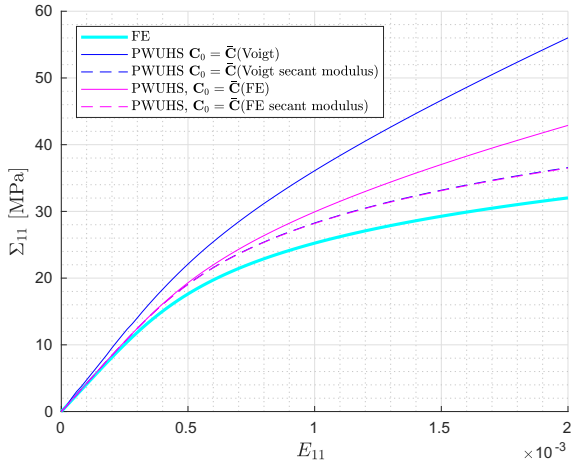

FIGURE 4.25: Macroscopic stress Σ_{11}, UC-3 with parameters in Table 4.5.

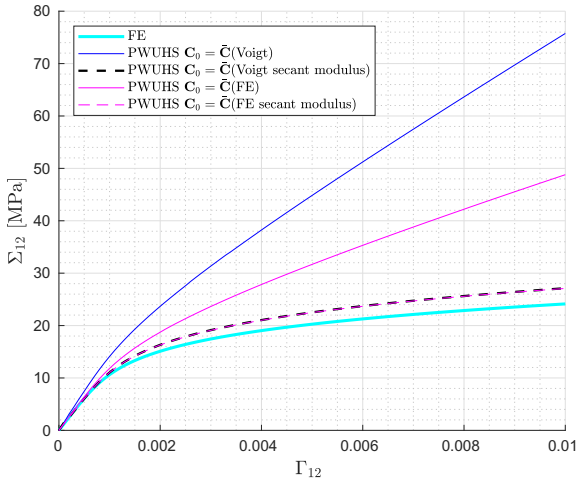

FIGURE 4.26: Macroscopic stress Σ_{12}, UC-3 with parameters in Table 4.5.

Load Case	$\mathbf{C_0}$	CPU time FE [s]	PWUHS speed-up
LC-1	$\bar{\mathbf{C}}$ (Voigt)	1183.75	4757.83
	$\bar{\mathbf{C}}$ (FE)		1594.70
	$\bar{\mathbf{C}}$ (Voigt), secant		986.45
	$\bar{\mathbf{C}}$ (FE), secant		917.63
LC-2	$\bar{\mathbf{C}}$ (Voigt)	1107.83	2702.02
	$\bar{\mathbf{C}}$ (FE)		1007.11
	$\bar{\mathbf{C}}$ (Voigt), secant		390.08
	$\bar{\mathbf{C}}$ (FE), secant		388.71

TABLE 4.6: Comparison between FE and PWUHS computational time: UC-3 subjected to LC-1 and LC-2.

Some considerations regarding the compuational time in PWUHS applications on UC-3 composed by a Ramberg-Osgood matrix are made. Speed-up factors of the homogenization scheme in comparison to the FE reference analyses are reported in Table 4.6, where the analytical derived elastic reference matrix demonstrates to be the best option in terms of computational time (see Fig. 4.25 and 4.26).

Numerical applications on different UCs show that, lowering the elastic inclusions volume fractions, the error decreases even considering more complex geometries. Furthermore, increasing the number of subsets, PWUHS results clearly tend toward to FE solution mantaining a big advantage in the low number of internal variables.
Numerical evidence of the reliability of the secant approach in the framework of PWUHS is given in all the applications; it can significantly improve the method accuracy with a neglectable increase of the computation time. This considerations are made disregarding the considered inelastic material model and both considering the Voigt or the finite element elastic reference material.

Chapter 5

Comparison between PWUHS and PWUTFA

Aim of this chapter is to compare the PWUTFA, which numerical procedure is presented in Section 3.2, with the PWUHS scheme presented in Chapter 4, for the homogenization of nonlinear composites. It is first proved that PWUTFA and PWUHS coincide in particular cases. Afterwards, the results of numerical applications on composites with different characteristics are discussed.

5.1 On the Equivalence between PWUTFA and PWUHS in special cases

In this section, it is proved that the PWUTFA and the PWUHS techniques coincide in particular cases. A UC composed by two materials is considered. Two subsets, denoted by Ω^1 and Ω^2, are introduced so that each material defines one subset. It is assumed that:

1. the material 1, occupying the subset Ω^1, is elastic, so that $\boldsymbol{\pi}^1 = 0$;
2. the material 2, occupying the subset Ω^2, is elasto-plastic, so that $\boldsymbol{\pi}^2 \neq 0$;
3. the two materials are characterized by the same elastic properties, i.e. $E^1 = E^2$, $\nu^1 = \nu^2$ and hence $\mathbf{C}^1 = \mathbf{C}^2 = \mathbf{C}$.

In the following, the main steps of both reduced order homogenization techniques are shown for the calculation of the average macroscopic stress $\boldsymbol{\Sigma}$.

PWUTFA

Because of the third condition, the localization matrices in the two subsets become identities, i.e. $\mathbf{L}_{\mathbf{E}}^1 = \mathbf{L}_{\mathbf{E}}^2 = \mathbf{I}$, i.e. it is the trivial matrix, so that recalling equation (3.7), the average fluctuation strains in the subsets are:

$$\begin{aligned} \bar{\hat{\boldsymbol{\varepsilon}}}^1 &= \bar{\mathbf{L}}_{\pi}^1 \boldsymbol{\Pi}, \\ \bar{\hat{\boldsymbol{\varepsilon}}}^2 &= \bar{\mathbf{L}}_{\pi}^2 \boldsymbol{\Pi}, \end{aligned} \tag{5.1}$$

where $\boldsymbol{\Pi} = \left\{\mathbf{0}, \boldsymbol{\pi}^2\right\}^T$.

The total average stresses obtained via the local stress-strain relationship are:

$$\begin{aligned} \bar{\boldsymbol{\sigma}}^1 =& \mathbf{C}\left(\mathbf{E} + \bar{\mathbf{L}}_{\pi}^1 \boldsymbol{\Pi}\right), \\ \bar{\boldsymbol{\sigma}}^2 =& \mathbf{C}\left(\mathbf{E} + \bar{\mathbf{L}}_{\pi}^2 \boldsymbol{\Pi} - \boldsymbol{\pi}^2\right). \end{aligned} \tag{5.2}$$

The evolutive problem is governed by the average stress $\bar{\boldsymbol{\sigma}}^2$ allowing to evaluate the inelastic strain $\boldsymbol{\pi}_2$ at the load step.

Finally, the macroscopic stress is obtained as:

$$\boldsymbol{\Sigma} = c^1 \bar{\boldsymbol{\sigma}}^1 + c^2 \bar{\boldsymbol{\sigma}}^2. \tag{5.3}$$

where c_1 and c_2 are the volume fractions of the two materials in the composite.

PWUHS

The third condition implies that:

$$\mathbf{C}^1 = \mathbf{C}^2 = \mathbf{C} = \mathbf{C}_0, \tag{5.4}$$

with $\mathbf{C}_0$ being the elasticity matrix of the elastic reference material. This has important consequences on the evaluation of the average stress polarizations $\bar{\boldsymbol{\tau}}^1$ and $\bar{\boldsymbol{\tau}}^2$ describing the stress gap between the heterogeneous materials and the homogeneous elastic reference material. Because of equation (4.2), the average polarization stresses assume the values:

$$\begin{aligned} \bar{\boldsymbol{\tau}}^1 &= \mathbf{0}, \\ \bar{\boldsymbol{\tau}}^2 &= -\mathbf{C}\boldsymbol{\pi}^2, \end{aligned} \tag{5.5}$$

According to equation (4.5), the average strain fluctuations $\bar{\hat{\boldsymbol{\varepsilon}}}^1$ and $\bar{\hat{\boldsymbol{\varepsilon}}}^2$ in each subset are:

$$\begin{aligned} \bar{\hat{\boldsymbol{\varepsilon}}}^1 &= \bar{\boldsymbol{\Gamma}}^1 \mathbf{T}, \\ \bar{\hat{\boldsymbol{\varepsilon}}}^2 &= \bar{\boldsymbol{\Gamma}}^2 \mathbf{T}, \end{aligned} \tag{5.6}$$

with $\mathbf{T} = \left\{\mathbf{0}, \bar{\boldsymbol{\tau}}^2\right\}^T$, hence the average stresses in the subsets obtained via the local stress-strain relationship are:

$$\begin{aligned} \bar{\boldsymbol{\sigma}}^1 =& \mathbf{C}\left(\mathbf{E} + \bar{\boldsymbol{\Gamma}}^1 \mathbf{T}\right), \\ \bar{\boldsymbol{\sigma}}^2 =& \mathbf{C}\left(\mathbf{E} + \bar{\boldsymbol{\Gamma}}^2 \mathbf{T} - \boldsymbol{\pi}^2\right). \end{aligned} \tag{5.7}$$

Finally, the macroscopic stress is obtained by equation (5.3).

Equations (5.5) and (5.6) allow to determine the average strain fluctuations in terms of the inelastic strain $\boldsymbol{\Pi}$, resulting:

$$\begin{aligned} \bar{\hat{\boldsymbol{\varepsilon}}}^1 &= \bar{\boldsymbol{\Gamma}}^1 \mathbf{T} = -\bar{\boldsymbol{\Gamma}}^1 \mathbb{C} \boldsymbol{\Pi} \\ \bar{\hat{\boldsymbol{\varepsilon}}}^2 &= \bar{\boldsymbol{\Gamma}}^2 \mathbf{T} = -\bar{\boldsymbol{\Gamma}}^2 \mathbb{C} \boldsymbol{\Pi} \end{aligned} \quad \text{with } \mathbb{C} = \begin{bmatrix} \mathbf{C} & \mathbf{0} \\ \mathbf{0} & \mathbf{C} \end{bmatrix} \tag{5.8}$$

Comparing these results with the expression of the average strain fluctuations given in equation (5.1) for the PWUFTA, it is:

$$\begin{aligned} \bar{\mathbf{L}}_\pi^1 &= -\bar{\boldsymbol{\Gamma}}^1 \mathbb{C} \\ \bar{\mathbf{L}}_\pi^2 &= -\bar{\boldsymbol{\Gamma}}^2 \mathbb{C} \end{aligned} \tag{5.9}$$

proving that the two localization operators are the same, net of the sign and constitutive matrix contribution. Thus, the average stresses in the subsets obtained according to (5.2) and (5.8) coincide, and both the procedures give the same macroscopic stress via equation (5.3).

5.2 Numerical applications

In this section, some 2D plane strain numerical applications are developed to assess the efficiency of the PWUTFA reduced order model and compare it to the PWUHS homogenization technique. In particular, results are compared with the ones obtained using nonlinear finite element (FE) micromechanical analyses.

Computations are performed for different geometries and material properties of the UC, comparing the main features of the two procedures. In particular, the computations concern:

- a homogeneous composite material, in order to verify the equivalence between the two ROM;
- convergence study of the PWUHS and PWUTFA schemes;
- heterogeneous composites with different mechanical properties, with the aim to estimate the accuracy of both reduced order models subjected to complex loading histories and increasing the number of subsets.

5.2.1 Homogeneous composite

Aim of this first application is to numerically verify the equivalence of the PWUTFA and PWUHS for a composite whose components are characterized by the same elastic properties, but one of them is plastic, as demonstrated in section 5.1.

The UC adopted for this ivestigation is the UC-1 reported in Fig 4.3. The elastic material properties are the same for the two subsets, thus $E^1 = E^2$ and $\nu^1 = \nu^2$, whose values are reported in Table 5.1.

The elasticity matrix of the reference material is $\mathbf{C}_0 = \mathbf{C}^1 = \mathbf{C}^2$, in agreement with equation (5.4).

E^1 [GPa]	ν^1	k [GPa]	σ_y [MPa]	E^2 [GPa]	ν^2
210	0.3	100	300	210	0.3

TABLE 5.1: Material parameters of plastic matrix '1' and elastic inclusion '2'.

The UC-1 is analyzed considering only two subsets Ω^1 and Ω^2, corresponding to the elastic inclusion and the plastic matrix, for the ROM approaches. The loading cases LC-1 and LC-2 introduced in section 4.3.2 are adopted in the

following applications.
Both homogenization procedures, PWUTFA and PWUHS, are used to determine the macroscopic stresses to compare with the average stress obtained from a FE micromechanical analysis. The overall nonlinear response of the composite material in terms of the macroscopic stress Σ_{11} versus E_{11} is reported in Fig. 5.1.

The results of the PWUTFA and PWUHS techniques perfectly match each other leading to the same overall response of the composite in both the elastic and plastic branches. It can be noted that both PWUTFA and PWUHS suffer stiffness overprediction, with respect to the FE reference solution, when plasticity occurs. Results given in Fig. 5.1 are, indeed, not in very good agreement with the FE reference solution, as only two subsets are considered in the computations. An improvement of the results can be achieved by increasing the number of subsets in the plastic matrix.

Then, computations are also performed adopting the PWUHS technique with the correction of the reference material during the nonlinear analysis. In Fig. 5.1 the results of the PWUHS with correction is also reported, demonstrating that the correction of $\mathbf{C}_0$ by means of the secant modulus approach is effective with a slight improvement of the macroscopic stress prediction, without increasing the number of subsets in the plastic matrix.

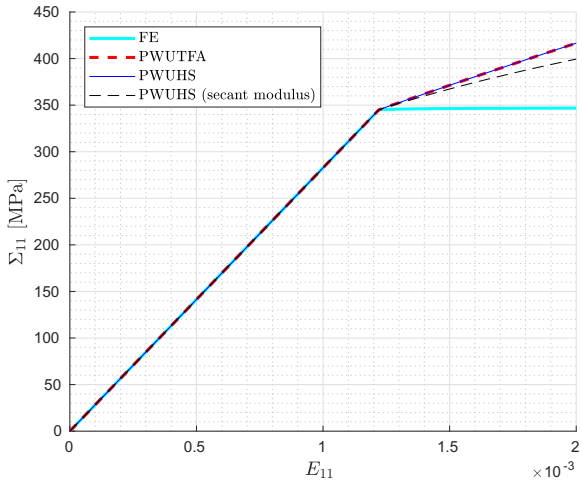

FIGURE 5.1: Overall response of the UC-1 in terms of Σ_{11} vs E_{11}.

Then, the UC in Fig. 4.3 is considered subjected to a loading history LC-2.

In Fig. 5.2, the shear response of the UC is reported plotting the overall stress Σ_{12}, obtained via PWUTFA and PWUHS, versus the average strain Γ_{12}. Also in this case, PWUTFA and PWUHS give exactly the same results, which are quite different from the FE reference solution. It can be remarked that computations performed using the proposed secant correction for the reference material leads to a significant improvement of the solution which results, indeed, very close to the FE reference solution.

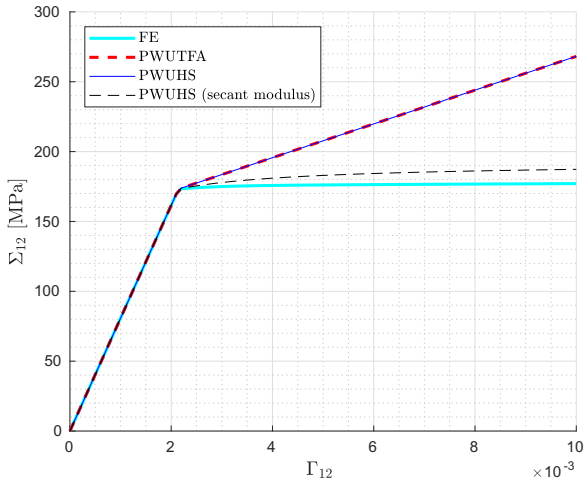

FIGURE 5.2: Macroscopic stress Σ_{12} in UC-1.

5.2.2 Convergence study

By increasing the number of subsets in the UC discretization it is, of course, expected that the solution converges towards the reference solution. In order to numerically investigate the rate of convergence of the PWUTFA and PWUHS techniques to the FE solution, two types of studies are developed for the cell UC-1, increasing the number of subsets to get a discretization that exactly matches the finite element mesh. Taking into account that the FE mesh consists in 60 elements for the inclusion and 45 elements for the matrix, the first study considers the inclusion as a unique subset and an increasing number of subsets is adopted for the matrix, up to 45; the second study considers 60 subsets for the inclusion and, again, an increasing number of subsets for the matrix, up to 45.

In Fig. 5.3 convergences curves for the two investigations above described are reported in terms of the overall stress Σ_{11} evaluated at the end of the loading phase versus the number of subsets in the matrix. As demonstrated above, the solutions obtained by the PWUTFA and PWUHS with initial reference material, coincide. For PWUHS, on the left the results are evaluated considering the elastic material properties as the reference material, while on the right the results are obtained updating the reference material adopting the secant stiffness approach. Figures demonstrate that both the approaches and inclusion discretizations converge towards the FE solution.

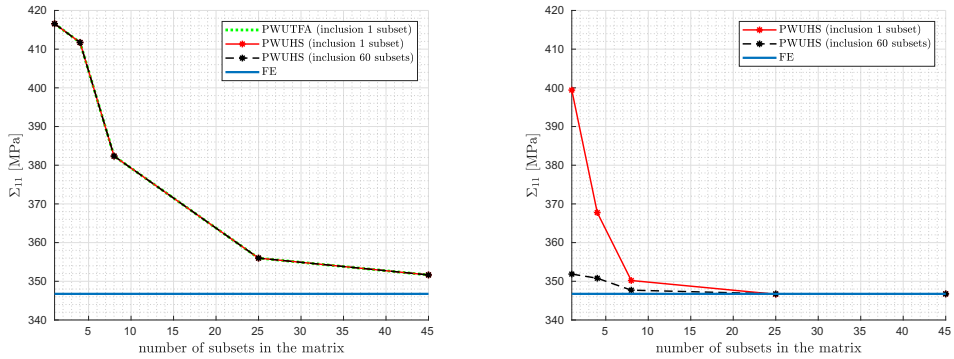

FIGURE 5.3: Convergence of PWUHS for the UC-1, using the initial $\mathbf{C}_0$ (left) and the secant modulus (right) approaches.

When the elastic reference matrix $\mathbf{C}_0$ is constant during the homogenization procedure (Fig. 5.3, left) no benefits arise increasing the number of subsets in the inclusion, but just the drawback of a higher computational time compared to the single subset for the inclusion. For the PWUHS this is due to the fact that the polarization stress is zero in all the elastic subsets representing the inclusion as, in this particular case, the reference material has the same elastic properties for the matrix and for the inclusion. For the PWUTFA the increasing of the number of subsets of the elastic inclusion does not lead to any benefit, as no further inelastic strains are activated. It can be remarked that the solutions of the homogenization techniques tend toward the reference solution without reaching it, even when the number of subsets is equal to the number of finite elements. In fact, both the techniques assume uniform inelastic effects in the subsets, while the FE considers nonuniform distribution of in elastic strain in each element.

When the secant modulus is used for $\mathbf{C}_0$ correction in the PWUHS, a fast convergence of the procedure clearly appears from Fig. 5.3 (right), obtaining almost the FE solution when about 25 matrix subsets are adopted. These results confirm the effectiveness of the secant modulus approach.

Very good results are obtained considering the fully refinement of the inclusion, i.e. introducing 60 subsets in the inclusion. In fact, a good macroscopic stress prediction is obtained even when the matrix is discretized by only one subset, corresponding to a discretization of the UC with 61 subsets. To obtain a better value of the macroscopic stress considering a unique subset for the inclusion, it is necessary to introduce at least 8 subsets for the matrix, leading to a UC discretization of 9 subsets. This results clearly remarks that it is more convenient from a computational point of view to increase the discretization of the matrix, where the nonlinear effects arise, with respect to the inclusion.

It is important to keep in mind that the number of unknowns of the problem is proportional to the number of subsets, as a consequence the more are the subsets, the more the computational burden increases.

Some considerations are made on the integration scheme used during the precomputations, in the framework of PWUHS and PWUTFA, and in the FE analyses.

It is known that a fully integrated 4-nodes element may exhibit *locking* and this is clearly confirmed in the present study. If a 4-GP integration scheme is adopted during the precomputations, the FEA results are not recovered even with the finest subset refinement (Fig. 5.4) disregarding the considered Reduced Order Model. On the other hand, the hypothesis of subset-wise constant variables suggests that a single Gauss point integration could be adopted to emulate the uniform quantities in the subsets: this integration scheme, usually known as Uniform Reduced Interation (URI) [64] avoids locking phenomena but introduces the possible arising of *spurious modes*, also known as *hourglass* deformation patterns.

Another reduced integration scheme is the so-called Selective Reduced Integration (SRI) technique [65, 66]. In comparison with URI, only the volumetric part of the material response is underintegrated, leaving the full integration scheme for the deviatoric part. These formulation do not suffer the appearance of hourglass modes, anyway only the volumetric locking is eliminated and a residual stiffness overprediction persists.

Further stabilization strategies may be applied to avoid non physical effects anyway this is not within the scope of the present work and further developements are left to future research.

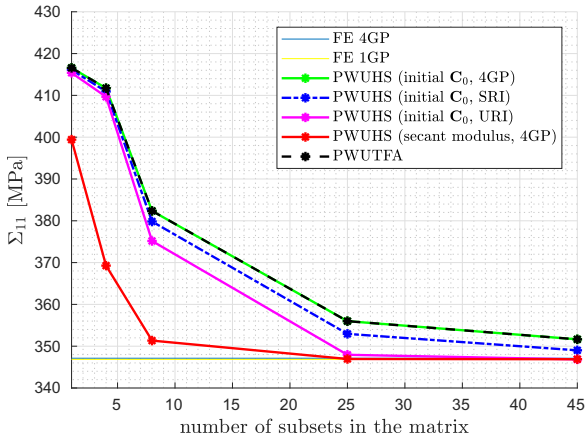

FIGURE 5.4: Convergence study on UC-1, comparison between PWUTFA and PWUHS using different integration schemes.

5.2.3 Heterogeneous composite material

Aim of this section is to investigate the mechanical behavior of a two phase composite material with different mechanical properties of the constituents, comparing the results obtained by PWUTFA and PWUHS reduced order models with the FE ones. This application is carried out in order to verify the effectiveness of the two procedures for composites characterized by different elastic properties, investigating the effect of the stiffness ratio of the constituents on the performances of the two ROM techniques.

The analyzed composite materials are made by a plastic matrix and elastic inclusions.

The considered UC's geometries are UC-1 and UC-3 (see Fig. 4.18) introduced in Chapter 4. Periodic boundary conditions are applied for all the numerical applications. Each UC is subjected to different loading histories, being monotonic or complex. Both the UCs are first discretized in two subsets representing the plastic matrix and the elastic inclusions; afterwards the plastic matrix is progressively refined, adopting a discretization in four and eight subsets.

Computations are performed adopting the PWUTFA, PWUHS with $\mathbf{C}_0 = \bar{\mathbf{C}}$ evaluating $\bar{\mathbf{C}}$ by Voigt or FE homogenization; moreover, PWUHS results obtained by the secant modulus approach are also carried out. Finally, all the ROM results are compared with the FE ones that are considered as a reference solution.

5.2.3.1 Ceramic inclusions in a metal matrix composite

A metal matrix composite with ceramic inclusions, whose material parameters are reported in Table 4.1, is considered for the two introduced UCs.

First, UC-1 is subjected to the loading history LC-1 and both homogenization procedures are adopted, comparing the macroscopic stresses, obtained from ROM techniques, with the average stress recovered by the micromechanical FE analysis.

Results in terms of the macroscopic stress Σ_{11} versus the average strain E_{11} are reported in Fig. 5.5. Both the methods suffer high stiffness overprediction in the nonlinear branch, even due to a rough subset discretization, as expected. the macroscopic stress obtained with the two methods are different from each other and from the micromechanical results.

In the PWUHS evaluating the overall elasticity matrix $\bar{\mathbf{C}}$ by Voigt or FE homogenization does lead to negligible differences in the results.

The PWUTFA results are slightly better than the PWUHS solution when the reference material is kept constant during the analysis, while a significant improvement of the PWUHS average stress evaluation is achieved adopting the secant approach to update the reference material.

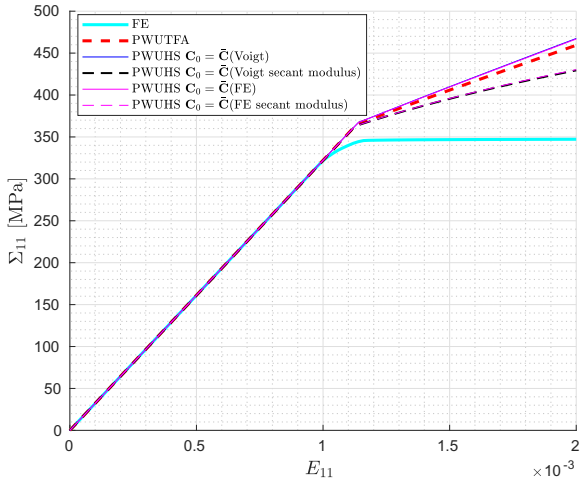

FIGURE 5.5: Macroscopic stress Σ_{11}, UC-1 with parameters in Table 4.1.

Then, UC-1 is studied considering LC-2 and the overall shear response is represented in Fig. 5.6. The same considerations reported for the previous loading condition can be made; the PWUTFA gives a slightly better macroscopic stress Σ_{12} prediction compared to PWUHS. The secant modulus approach sensibly increases the accuracy of the PWUHS approach giving results very close to the reference solution. This satisfactory results is mostly due to effect of the shear modulus correction of the reference material during the analyses.

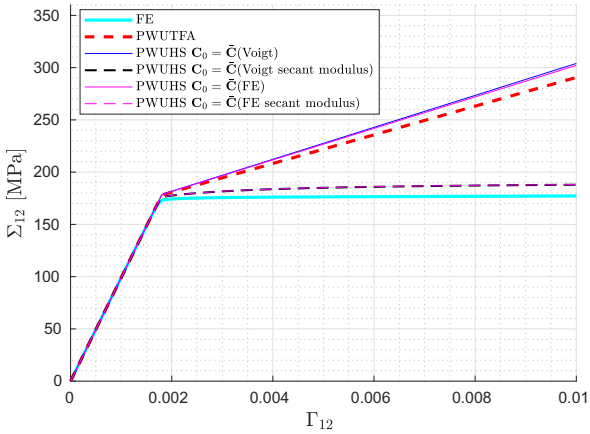

FIGURE 5.6: Macroscopic stress Σ_{12}, UC-1 with parameters in Table 4.1.

Then, the response of the UC-3 is investigated for the two loading histories

LC-1 and LC-2. The results in terms of the macroscopic stress components Σ_{11} and Σ_{12} are illustrated in Figs.5.7 and 5.8, respectively.

As for the results of UC-1 the PWUTFA and PWUHS give close results, where the first approach leads to a slight improvement. No advantages come computing the overall elasticity matrix $\bar{\mathbf{C}}$ by FE homogenization with respect to Voigt approach. The secant approach for updating the reference material allows to obtain more reliable results than a constant reference material approach for both the considered loading cases. Some other additional considerations are made comparing the numerical investigations on UC-1 and UC-3. Both methods, PUTFA and PWUHS, show similar results; increasing the elastic phase volume fraction causes loss of accuracy in both reduced order approaches. Furthermore, a stiffness correction approach like the secant modulus is efficient regardless the volume fractions of the material constituents.

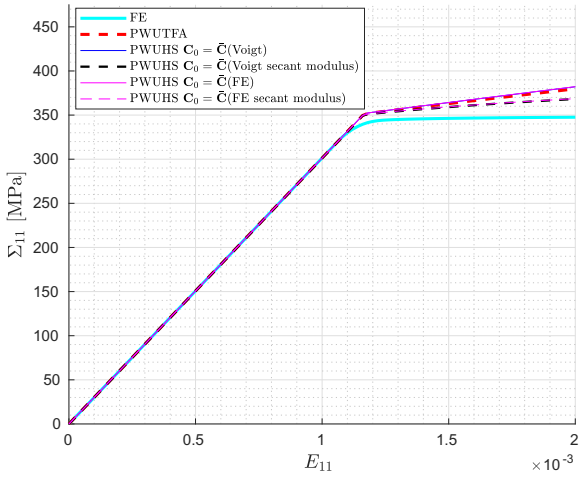

FIGURE 5.7: Macroscopic stress Σ_{11}, UC-3 with parameters in Table 4.1.

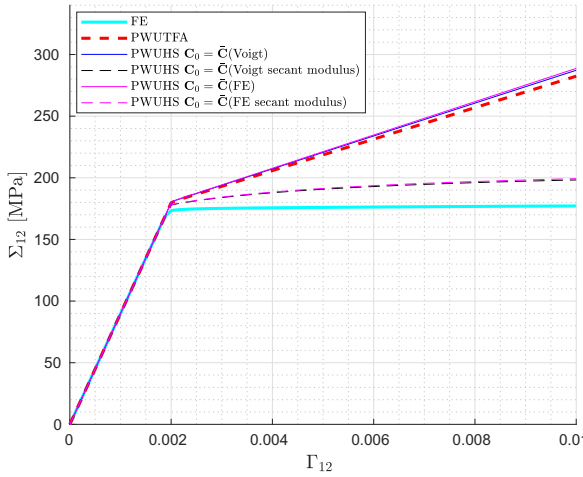

FIGURE 5.8: Macroscopic stress Σ_{12}, UC-3 with parameters in Table 4.1.

5.2.3.2 Fiber reinforced epoxy resin composite

A fiber reinforced epoxy resin composite, whose material properties are reported in Table 4.2, is studied considering the two UCs introduced in the previous sections.

In Figs. 5.9 and 5.10 the curves $\Sigma_{11} - E_{11}$ for loading history LC-1 and $\Sigma_{12} - \Gamma_{12}$ for LC-2 are plotted for UC-1, respectively.

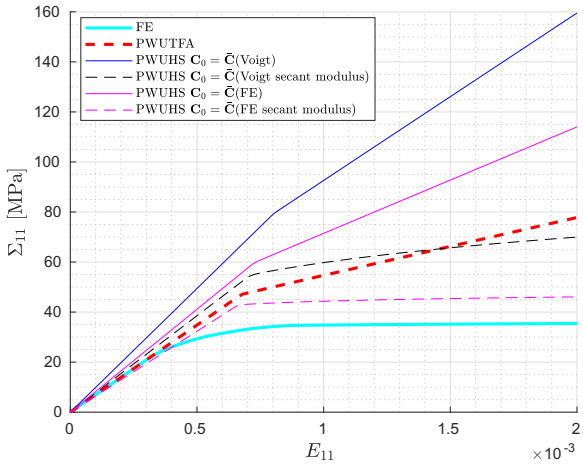

FIGURE 5.9: Macroscopic stress Σ_{11}, UC-1 with parameters in Table 4.2.

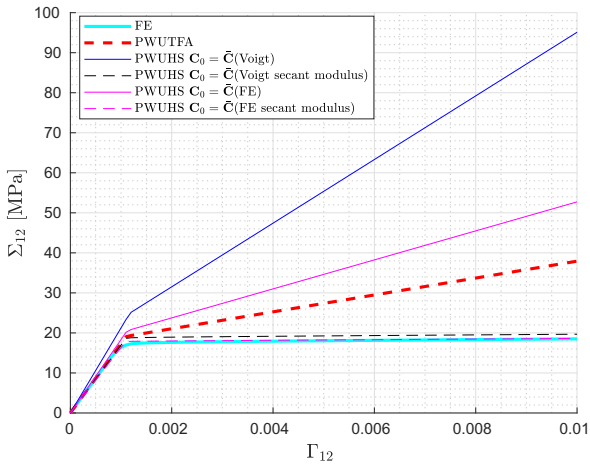

FIGURE 5.10: Macroscopic stress Σ_{12}, UC-1 with parameters in Table 4.2.

In these applications, where the difference between the constituents elastic parameters is significant (see Table 4.2), the PWUTFA leads to a significantly better macroscopic stress prediction in comparison with PWUHS when the reference material is kept constant during the analysis. The PWUHS results are improved by evaluating the reference elastic matrix $\mathbf{C}_0 = \bar{\mathbf{C}}$ by the FE homogenization, mainly for LC-1. Furthermore, when the secant modulus approach is used, the PWUHS results are in very good agreement with the micromechanical analyses, especially for the shear loading case LC-2.

In figure 5.11 and 5.12 the overall stress-strain relationships for LC-1 and LC-2 are reported for UC-3, respectively.

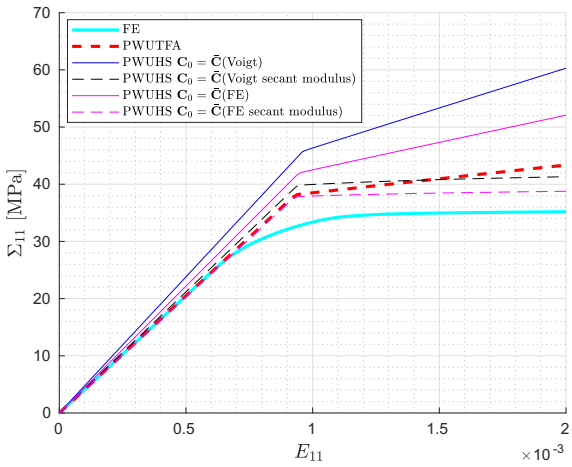

FIGURE 5.11: Macroscopic stress Σ_{11}. UC-3 with parameters in Table 4.2.

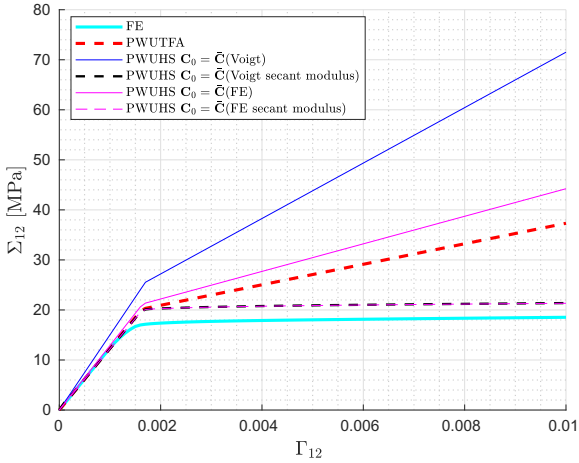

FIGURE 5.12: Macroscopic stress Σ_{12}, UC-3 with parameters in Table 4.2

Similar considerations can be made. The PWUTFA results are more accurate with respect to PWUHS ones when the reference material is kept constant. The best results with respect to FE solution are achieved adopting the PWUHS with the secant approach.

Then, the response of UC-1 subjected to loading/unloading strain history, with constant strain rate, is investigated. To this end two loading cases, namely

LC-3 and LC-4 are introduced. In LC-3 both axial and shear strain are considered, as shown in Table 5.2; a biaxial loading history is considered in LC-4, as shown in 5.3.
Results obtained via the two ROM approaches, with an increasing number of inelastic subsets, are reported in Fig. 5.14 for LC-3 and in Fig. 5.15 for LC-4, where the evolution of the macroscopic stress components, with respect to the loading history, is illustrated.

The error estimates of PWUHS and PWUTFA, captured in the time steps of major interest via equation (4.34), are given in Tables 5.4-5.6 for LC-3 and in Tables 5.7-5.8 for LC-4, for all the macroscopic stress components $\Sigma_{11}, \Sigma_{22}, \Sigma_{12}$ with the UC discretized in 2,5,9 subsets; only the maximum relative errors are reported and when constant null values of the macroscopic FE stresses are encountered, the evaluation of the error is ignored.
With the UC discretized in only two subsets corresponding to the material constituents, results are in agreement with the previous investigations; PWUHS with fixed reference material elastic matrix is slightly less accurate if compared to PWUTFA.
Additional information are obtained when the number of subsets is increased. A refinement of the plastic matrix division benefits both ROM approaches; the results of the PWUHS are in general more accurate in comparison to PWUTFA, for the same subsets amount.
The evolution of the macroscopic stress is captured along the whole loading/unloading path especially via the PWUHS with the finest subsets discretization. In this case, all the macroscopic stress components predictions are close to the FE results, disregarding the considered loading history.
The relative error dicreases dividing the matrix material in both ROM techniques, reaching its minimum when PWUHS is applied to a 9 subsets UC.
The best results in comparison to FE solution are obtained adopting the secant approach in the framework of the PWUHS. Even considering the coarsest subsets division the macroscopic stress prediction is close to the FE recovered values with low error estimates, barely exceeding the 1%.
Furthermore, the error get close to null values for all the stress components and disregarding the considered loading history, if a refined discretization of the UC is adopted. The secant modulus approach allows for a accurate stress prediction along both the loading and unloading branches.

t [s]	E_{11}	E_{12}
0	0	0
1	0.002	0
2	0.002	0.01
3	-0.002	0.01
4	-0.002	0

TABLE 5.2: Loading case 3, LC-3.

t [s]	E_{11}	E_{22}
0	0	0
1	0.002	0
2	0.002	0.002
3	-0.002	0.002
4	-0.002	0

TABLE 5.3: Loading case 4, LC-4.

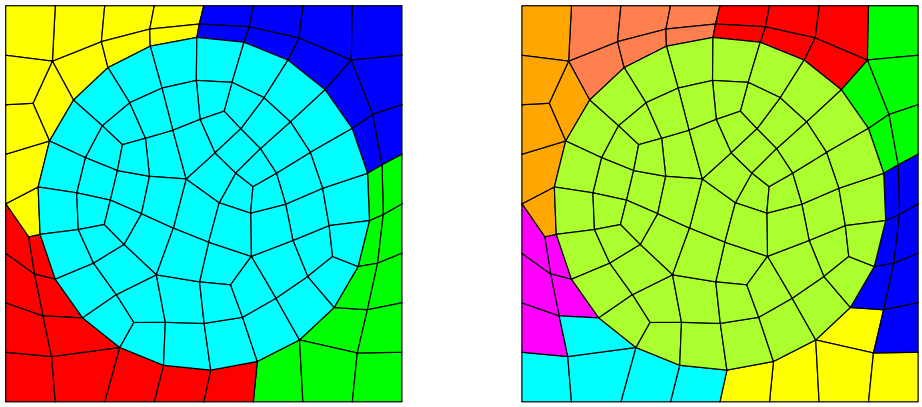

(a) (b)

FIGURE 5.13: (a) UC-1 divided in 5 subsets, (b) UC-1 divided in 9 subsets.

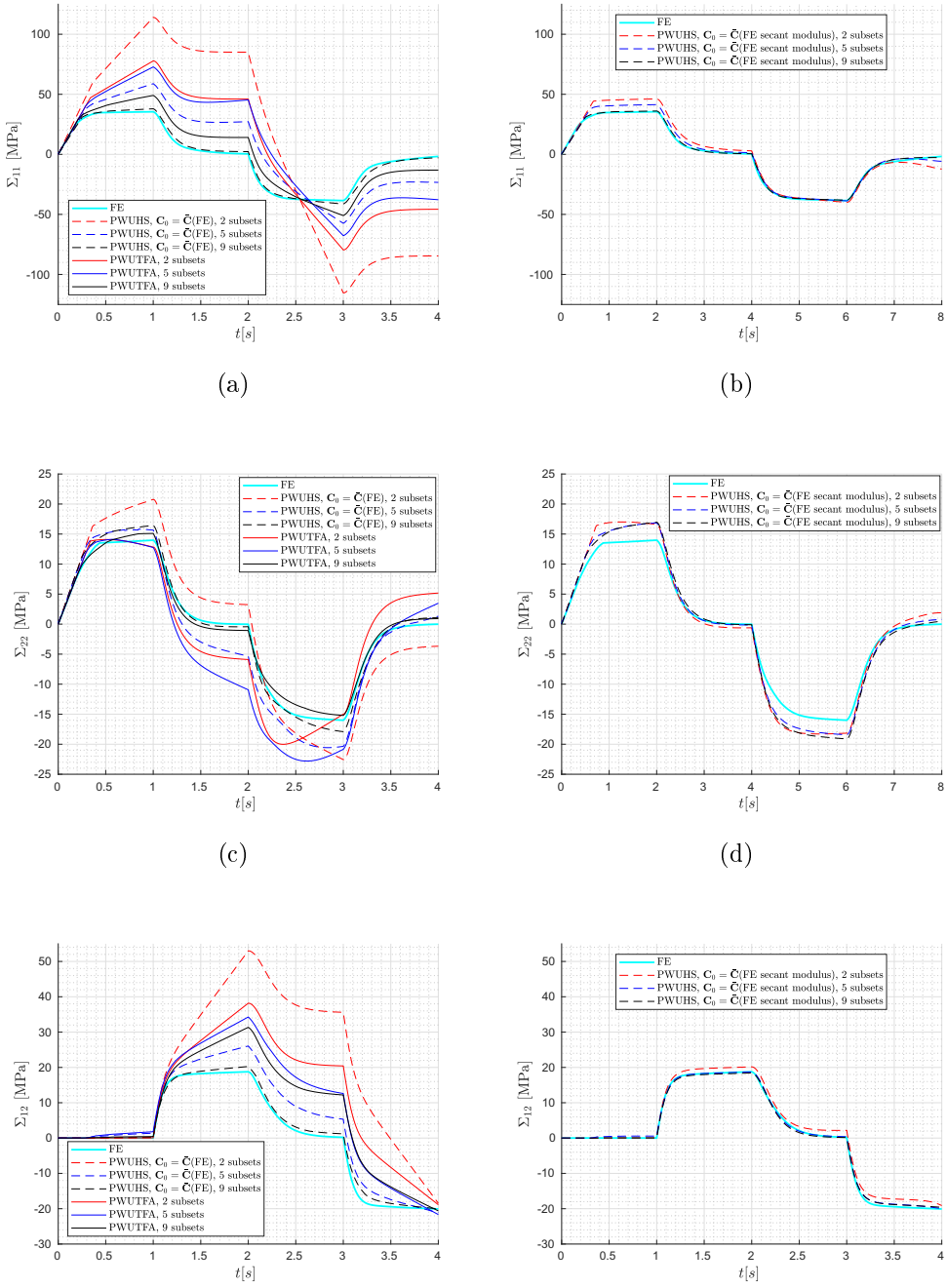

FIGURE 5.14: Macroscopic stress of UC-1 discretized in 2, 5, 9 subsets, having material parameters in Table 4.2 and subjected to loading history LC-3: (a) Σ_{11} with fixed $\mathbf{C}_0 = \bar{\mathbf{C}}$; (b) Σ_{11} with secant updated $\mathbf{C}_0 = \bar{\mathbf{C}}$; (c) Σ_{22} with fixed $\mathbf{C}_0 = \bar{\mathbf{C}}$; (d) Σ_{22} with secant updated $\mathbf{C}_0 = \bar{\mathbf{C}}$; (e) Σ_{12} with fixed $\mathbf{C}_0 = \bar{\mathbf{C}}$; (f) Σ_{12} with secant updated $\mathbf{C}_0 = \bar{\mathbf{C}}$.

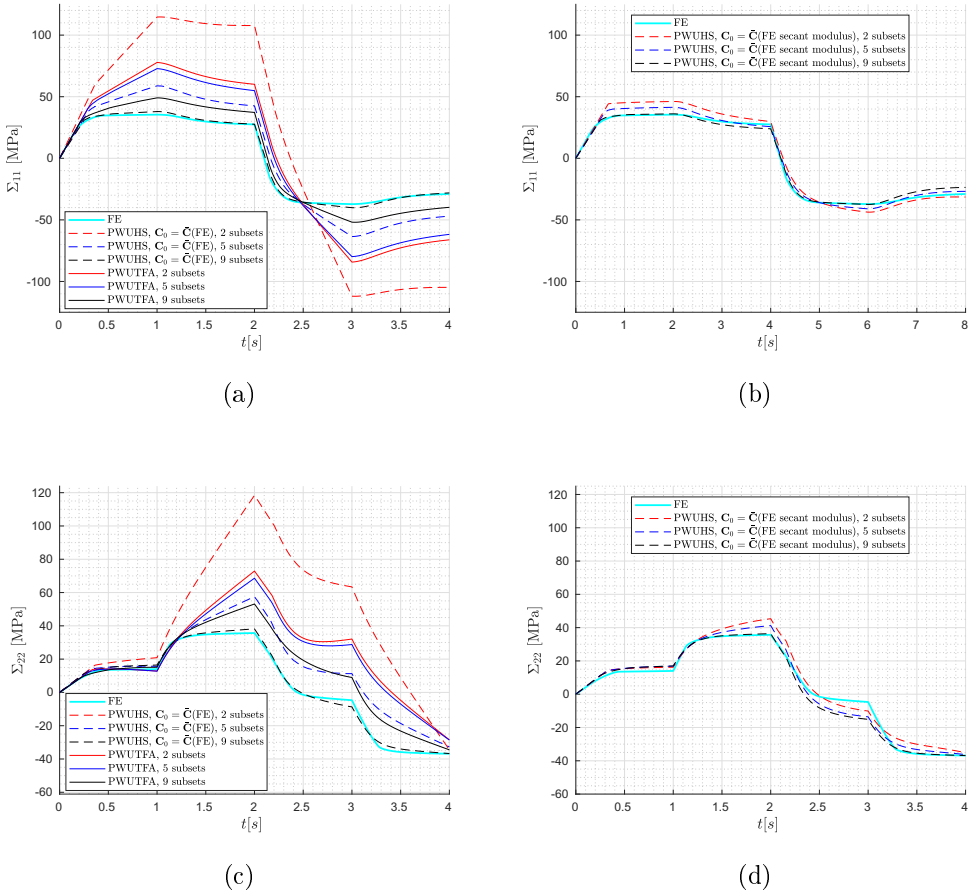

FIGURE 5.15: Macroscopic stress of UC-1 discretized in 2, 5, 9 subsets, having material parameters in Table 4.2 and subjected to loading history LC-4: (a) Σ_{11} with fixed $\mathbf{C}_0 = \bar{\mathbf{C}}$; (b) Σ_{11} with secant updated $\mathbf{C}_0 = \bar{\mathbf{C}}$; (c) Σ_{22} with fixed $\mathbf{C}_0 = \bar{\mathbf{C}}$; (d) Σ_{22} with secant updated $\mathbf{C}_0 = \bar{\mathbf{C}}$.

	$t=1$			$t=2$			$t=3$			$t=4$		
subsets	2	5	9	2	5	9	2	5	9	2	5	9
PWUHS, $\mathbf{C}_0 = \bar{\mathbf{C}}$	2.216	0.659	0.069	199.099	63.095	4.288	1.997	0.491	0.075	47.951	12.532	0.665
PWUHS, $\mathbf{C}_0 = \bar{\mathbf{C}}$, secant	0.301	0.167	0.017	5.790	2.251	0.250	0.038	0.006	0.009	6.066	2.363	0.586
PWUTFA	1.194	1.053	0.383	107.205	105.600	32.084	1.067	0.758	0.324	25.458	20.865	6.600

TABLE 5.4: Relative Error of PWUHS and PWUTFA with respect of FE analyses, UC-1 discretized in 2-5-9 subsets and subjected to loading/unloading history LC-3, stress component Σ_{11}.

	$t=1$			$t=2$			$t=3$			$t=4$		
subsets	2	5	9	2	5	9	2	5	9	2	5	9
PWUHS, $\mathbf{C}_0 = \bar{\mathbf{C}}$	0.486	0.120	0.176	134.447	219.465	16.600	0.409	0.271	0.119	316.208	114.960	92.263
PWUHS, $\mathbf{C}_0 = \bar{\mathbf{C}}$, secant	0.188	0.206	0.213	24.106	4.502	2.906	0.134	0.151	0.194	163.867	67.057	42.529
PWUTFA	0.082	0.087	0.080	241.957	449.935	42.721	0.063	0.302	0.050	447.873	301.884	79.570

TABLE 5.5: Relative Error of PWUHS and PWUTFA with respect of FE analyses, UC-1 discretized in 2-5-9 subsets and subjected to loading/unloading history LC-3, stress component Σ_{22}.

	$t=1$			$t=2$			$t=3$			$t=4$		
subsets	2	5	9	2	5	9	2	5	9	2	5	9
PWUHS, $\mathbf{C}_0 = \bar{\mathbf{C}}$	–	–	–	1.824	0.388	0.079	160.854	23.243	4.378	0.079	0.053	0.001
PWUHS, $\mathbf{C}_0 = \bar{\mathbf{C}}$, secant	–	–	–	0.074	0.002	0.018	8.944	0.717	0.278	0.048	0.005	0.024
PWUTFA	–	–	–	1.034	0.825	0.670	91.878	56.333	54.449	0.059	0.078	0.027

TABLE 5.6: Relative Error of PWUHS and PWUTFA with respect of FE analyses, UC-1 discretized in 2-5-9 subsets and subjected to loading/unloading history LC-3, stress component Σ_{12}.

	$t=1$			$t=2$			$t=3$			$t=4$		
subsets	2	5	9	2	5	9	2	5	9	2	5	9
PWUHS, $\mathbf{C}_0 = \bar{\mathbf{C}}$	2.234	0.659	0.069	2.921	0.547	0.004	2.008	0.706	0.077	2.616	0.619	0.030
PWUHS, $\mathbf{C}_0 = \bar{\mathbf{C}}$, secant	0.301	0.167	0.017	0.084	0.066	0.129	0.175	0.102	0.005	0.085	0.073	0.185
PWUTFA	1.194	1.053	0.383	1.184	0.997	0.354	1.264	1.144	0.393	1.283	1.130	0.373

TABLE 5.7: Relative Error of PWUHS and PWUTFA with respect of FE analyses, UC-1 discretized in 2-5-9 subsets and subjected to loading/unloading history LC-4, stress component Σ_{11}.

	$t=1$			$t=2$			$t=3$			$t=4$		
subsets	2	5	9	2	5	9	2	5	9	2	5	9
PWUHS, $\mathbf{C}_0 = \bar{\mathbf{C}}$	0.493	0.120	0.176	2.318	0.612	0.069	14.577	3.416	0.860	0.063	0.112	0.003
PWUHS, $\mathbf{C}_0 = \bar{\mathbf{C}}$, secant	0.159	0.206	0.213	0.271	0.155	0.019	1.168	1.908	2.235	0.047	0.016	0.0003
PWUTFA	0.082	0.087	0.080	1.043	0.923	0.489	7.869	7.163	2.921	0.227	0.223	0.064

TABLE 5.8: Relative Error of the PWUHS with respect of FE analyses, UC-1 discretized in 2-5-9 subsets and subjected to loading/unloading history LC-4, stress component Σ_{22}.

Chapter 6

Multiscale Analysis using PWUHS

In this Chapter the PWUHS homogenization technique introduced in Chapter 4 is used in the framework of a Multiscale Analysis, as presented in Chapter 2. In particular, the behaviour of a nonlinear heterogeneous structure having auxetic properties is investigated. To this end a brief introduction to this class of *Metamaterials* is made first. In the following, the PWUHS homogenization scheme is used in a multiscale analysis of a foam-filled auxetic honeycomb. A detailed description of the multiscale procedure is made. Material and geometrical properties of the adopted microstructure are then presented and numerical applications are carried out. Finally, an experimental validation, with a focus on the specimens manufacturing process, is presented.

6.1 Auxetic materials

A large amount of composite materials have been developed during the past decades in order to meet the requirements of many structural engineering applications. The increasing interest in composite materials has resulted in their usage in aerospace, automotive, sports and leisure sectors. Nevertheless, composite materials show some disadvantages in relation to mechanical properties such as shear modulus, impact resistance, and energy absorption capabilities [67]. Thus, a new class of materials, regarded as auxetic materials [68], have been designed since the middle 80's in order to achieve the desired requirements [69, 70, 71, 72, 73]. Auxetic materials are characterized by a negative Poisson ratio : in short, this means that if strectched longitudinally they expand in the perpendicular direction.

Materials with auxetic properties exist in nature (i.e. arsenic and cadmium crystals, cat or cow skins) and plenty of them have been produced in industry, from PU foams to polymers and metals. This class of *metamaterials* is especially used to enhance the mechanical properties of crash absorbers [74]. In particular, auxetic materials can be the cellular core of crash absorbers or a filler material, e.g. in sandwich panels, where a low stiffness filler material is bounded by rigid plates.
The several types of auxetic cellular materials can be classified in three main categories [75]: auxetic honeycombs, being the conventional and most common types, polymers with auxetic microstructures, obtained from conventional foams or specifically designed (e.g. PTFE, UHMWPE) and auxetic composites, obtained laminating unidirecrional composites or embedding rod and hinge structures in a matrix.
Auxetic honeycombs can be further divided according to the deformation mechanism [76] in three main groups:

- Re-entrant type: this kind of auxetic structures were the first to be developed. The most common geometry was introduced by Gibson et al. [77] and is commonly regarded as *Inverted hexagons* (see Fig. 6.1, a). The geometry is designed so that when a load is applied in a direction, the diagonal ribs move in the perpendicular direction leading to the auxetic behaviour. Other kind of re-entrant geometries having a common defomation mechanism are the double-arrow and star shaped geometries;

- Chiral type: these auxetic structures are composed of bars tangentially connected to circular or polygonal rings (see Fig. 6.1, b). The term *chiral* indicates non-mirroring and non-superimposable geometries. The auxetic behaviour is caused from the rotation of the rings, and the consequent wrapping-unwrapping of the rigidly connected bars, due to the application of an external load. Chiral auxetic structures are usually considered delivering a Poisson ratio close to -1.

- Rotating polygons: these auxetic geometries are composed by rigid polygons (squares, rectangles, rhombi or others) that are connected each other by hinges. On the other hand, this kind of geometries can be interpreted, according to their manufacturing process, as perforated sheets, having, for example, rhomboidal holes (see Fig. 6.1, c). The auxetic behaviour is clearly caused from the rotation of the connected polygons.

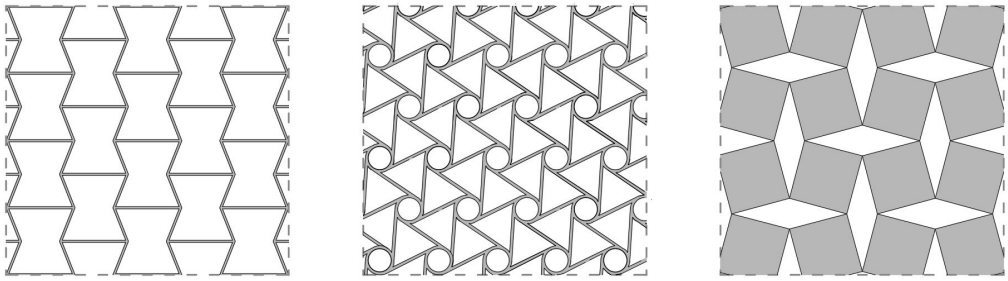

FIGURE 6.1: Auxetic structures: (a) re-entrant type, (b) chiral type, (c) rotating polygons.

Many experimental and numerical investigations have been carried out in order to study the response of materials with auxetic behaviour. In particular, research has focused on the energy absorption capabilities of cellular auxetic materials under compressive loads in dynamic [73, 78, 79] or quasi static [80, 81] conditions.

Various material properties of the cellular structure have been considered: in [78]-[80] a hollow auxetic core is adopted for the investigations. On the contrary, foam-filled auxetic structures are considered in [81, 82]; the foam filler, being a polymeric, aluminium or concrete based material, is proven to improve the energy dissipation capabilities of the auxetic cores.

Re-entrant hexagonal and chiral geometries are mostly considered for both numerical and experimental investigations. In [81], a concrete foam filled auxetic aluminium honeycomb is experimentally and numerically investigated if subjected to low velocity compression; the response of a chiral auxetic structure is studied by empirical and numerical tests for both static loads [83] and impact loads [84].

Further research is oriented in determine the average properties of auxetic structures with various geometrical and material properties.

Many analytical and computational tecniques for the determination of the effective properties of hollow or foam-filled cores have been proposed. First, theoretical [85] and FE-based approaches [86] were used to determine the homogenized response of hollow non-auxetic honeycomb structures.

In [87] a computational homogenization scheme is used to determine the effective material properties of aluminium re-entrant hexagonal honeycomb with PVC foam filler. A FE-homogenization technique for periodic materials is used to compute effective elastic properties of auxetic microstructures and compare

different geometries [72].
Both computational and analytical predictions of the elastic modulus are made in [88], where a parametric study of a re-entrant hexagonal honeycomb with varying geometrical properties is carried out.

6.2 Foam-Filled Auxetic Honeycomb

Honeycomb structures are usually combined with a filler material, e.g. polymer, concrete or metallic foams, in order to enhance the mechanical capabilities of final product, as sandwich panels. In particular, using a foam filler leads to a sensible increment of the energy absorption capabilities of frames made of ductile materials.
A large amount of research has focused on the properties prediction of hollow honeycombs. A small number of investigations have been carried out on filled honeycombs structures: among them, aluminium honeycomb frames have been considered filled by a PVC foam [87] or a concrete foam [81].
In other very recent studies, hollow 3D-printed auxetic cores have been numerically and empirically investigated under different load conditions [89, 90]. At best of author's knowledge, only in Airoldi et al. [82] a polymeric 3D printed chiral topology auxetic structrure filled with urethane pre-cut foam inserts have been investigated, performing numerical and experimental studies. No consideration on the homogenized response of the composite auxetic material were made.
A similar combination of materials is here considered: a 3D Printed polymeric frame filled with a Polyurethane (PU) foam is considered in the framework of Multiscale analysis, in order to derive the homogenized response of the composite material.

6.2.1 3D-Printed Polymeric Frame

The auxetic re-entrant hexagonal frame is considered made of PA12, a 3D printable Polyamide, also known as nylon. PA12 is the most common material in additive manufacturing; it is an high performance alternative in comparison to ABS or PA6 and it is usually preferred due to the higher tensile modulus [91] allowing for manufacturing of robust, durable and resistant parts.
Its chemical and physical properties make it extremely versatile: applications

in industry go from prototyping to series production parts, especially in the electrical, automotive industries as well as in mechanical engineering, moulding, sports, biological and food related uses.
PA 12 is a thermoplastic material usually commercialized in powder, having a characteristic particle size of $60\mu m$ and a melting point of $176-187°C$. It is primarily used in the additive Powder Bed Fusion (PBF) processes to form objects with high strength and stiffness. It is used for production of robust high-density parts with uniform properties and long-term reliable behaviour. The obtained parts have excellent chemical resistance to greases, oils and alkalies.
The main advantage in using PA 12 in manufacturing relies in the possibility to recicle up to the 80% of the unused powder and process resulting wastes, leading to a big advantage in terms of costs per produced part.
It is generally considered as the best option in terms of costs and performances, and is engineered for production of final parts with smooth details and high dimensional accuracy.
The properties of interest of the PA 12 can be easily found thanks to the large availability on the market; this means that no characterization of the material is needed. In the following numerical and experimental applications the "3D High Reusability PA 12" produced by HP is referred for the material properties.
Although different kind of inelastic material models can be adopted, the classical associated Mises perfect plasticity is considered for PA 12 and the Mises yield criterion is adopted. The material properties of interest for the next applications are extrapolated from the techical datasheet provided from the producer [92] and are reported in Table 6.1.

E [MPa]	ν	σ_y [MPa]
1700	0.41	48

TABLE 6.1: Mechanical properties of HP 3D High Reusability PA 12.

6.2.2 Rigid Polyurethane Foam Filler

Polyurethanes are a group of polymers obtained from the interaction between two ingredients, a polyol and an isocyanate. For the production of PU foams, water is intentionally added to the mixture; the isocyanate reacts with the water in the compound and forms a urea linkage and carbon dioxide gas. The resulting polymer contains urethane and urea linkages. The reaction is heavily exothermic

and the time depends on the stechiometric ratio and the catalyst.
With an accurate selection and calibration of the reactants is possible to desing products having the desired characteristics, going from soft expanded foams to high mechanical perfomances rigid polyurethanes.
The auxetic Polymeric frame is here considered filled by a rigid PU foam which adheres to the 3D printed PA 12 walls. A material characterization of PU foams is required in order to obtain the mechanical properties herein considered for the numerical investigation of the foam-filled auxetic honeycomb.
The commercial materials chosen for the characterization are two bi-component pourable PU foams provided by BCI Polyurethane Europe S.R.L. (VA, Italy). In both cases the resulting product is an high density rigid foam, with an high percentage of closed cells and a considerable strenght in both compression and tension.
The two materials, coming in two components (Fig. 6.5, a), adopt the same isocyanate which commercial name is Isotem® P200. The polyols suggested for the scope are the Promol® DP 25/10B1 [93] and Promol® VA 50/6A3 [94], delivering respectively foams with a final density of 25 kg/m^3 and 145 kg/m^3.

The mechanical characterization of the rigid PU foams is performed according to the standards prescribed by the American Society for Testing and Materials (ASTM). In particular, the '*"Standard Test Method for Compressive Properties of Rigid Cellular Plastics"* [95] is considered.
This standard prescribes the procedure for determining the compressive mechanical porperties of rigid cellular materials (e.g. rigid foams) by using universal testing machines to study the response of specimens to the movement of the cross head. The main goal is to obtain a complete load-deformation curve from which relevant informations are derived for the numerical investigations on the foam filled auxetic honeycomb; in this case the aim is to compute the modulus of elasticity and the yield stress.
The apparatus used for the compression tests is the MTS Insight Testing System (MTS System Corporation) equipped with a 10KN load cell and two steel compression plates 6.2.

The specimens are circular in cross section (ϕ = 60 mm) and 40 mm high, with the loaded faces parallel to each other and perpendicular to the sides. In order to produce specimens which surfaces are free from imperfections, custom

FIGURE 6.2: The MTS Insight Testing System used for the compression tests.

made 3D printed molds are designed and produced, having the desired dimensions and a easy unmolding system (see Fig. 6.5, c and d). Furthermore, when the foam is cast into the mold, a 3D printer with heated chamber is used to mantain the optimal reaction temperature of $40°C$.
Four specimens for each of the two samples are prepared (Fig. 6.5, e and f) and tested. The specimens are uniformly loaded over the top surface with a loading rate of 5 mm/min, until 40% deformation is reached. The cross-head diplacements are assumed as measure of deflection and an automatic recorder is used; a load-displacement curve is directly obtained.
A suitable point is chosen along the straight portion of the of the load-displacement curves for the calculation of the apparent elastic modulus, as:

$$E = \frac{Fh}{A\varepsilon_h} \tag{6.1}$$

where F (N) is the load, h (mm) is the height of the specimen, A is the initial horizontal cross-sectional area (mm^2) and ε_h is the axial strain along the loading direction.

The load-displacements curves used for the determination of the material properties of DP 25/10B1 and VA 50/6A3 foams, are respectively reported in Figs. 6.3 and 6.4. Responses are characterized by an initial elastic behaviour followed by yielding and plastic deformation.

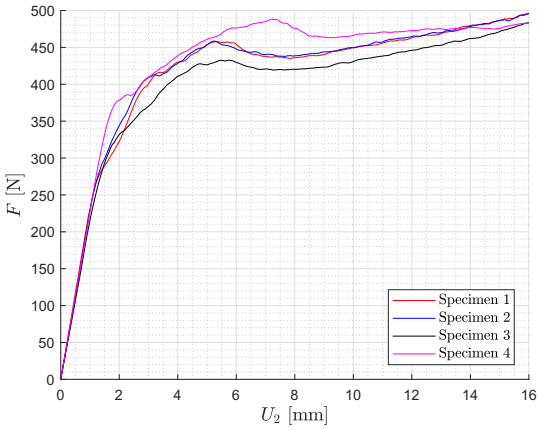

FIGURE 6.3: Load-displacements curves of the compression tests on DP 25/10B1 specimens.

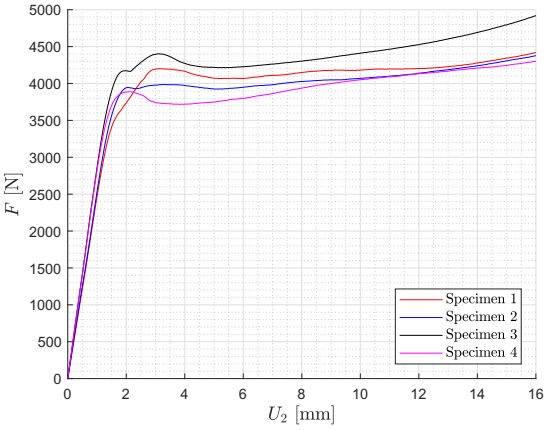

FIGURE 6.4: Load-displacements curves of the compression tests on VA 50/6A3 specimens.

The characteristic dimensions of the specimens and results in terms of the measured apparent Elastic Modulus E are reported in Table 6.3 for DP 25/10B1 foam and in Table 6.4 for VA 50/6A3 foam.
The results, combined with the experimental load-displacements curves, allow for

a complete characterization of the foams that exhibit an elastoplastic behaviour. The average elastic modulus of the low and high density foams are, respectively, 3.22 ± 0.13 and 37.82 ± 3.02 MPa.
The low density PU foam (DP 25/10B1 - Isotem P200) is adopted in the following numerical and experimental applications on the foam filled auexetic honeycomb. To this end, additional information are required in order to consider the PU foam following a Mises plasticity law with linear isotropic hardening. In particular, average yield stress and an hardening parameter are obtained from the curves in Fig. 6.3 and reported in Table 6.2.

E [MPa]	ν	σ_y [MPa]	k [MPa]
3.22	0.27	0.13	0.1

TABLE 6.2: Mechanical properties of low-density DP 25/10B1 foam.

DP 25/10B1 - Isotem P200				
	Diameter ϕ [mm]			
Measurement n	1	2	3	Average
Specimen 1	59.48	60.07	59.89	59.81
Specimen 2	59.55	59.58	59.99	59.71
Specimen 3	59.84	59.4	59.44	59.56
Specimen 4	59.59	59.71	59.78	59.69
	Height h [mm]			
Measurement n	1	2	3	Average
Specimen 1	40.09	40.09	40.22	40.13
Specimen 2	39.88	39.99	40.10	39.99
Specimen 3	40.11	40.30	40.56	40.32
Specimen 4	41.05	40.99	40.76	40.93
	Base Area A [mm^2]		Elastic Modulus E [MPa]	
Specimen 1	2809.87		3.34	
Specimen 2	2799.85		3.12	
Specimen 3	2786.12		3.09	
Specimen 4	2798.60		3.32	

TABLE 6.3: DP 25/10B1 Foam: dimensions of the specimens and apparent Elastic Modulus E calculated according to equation (6.1).

VA 50/6A3 - Isotem P200				
	Diameter ϕ [mm]			
Measurement n	1	2	3	Average
Specimen 1	60.05	60.42	60.04	60.17
Specimen 2	59.84	59.85	59.83	59.84
Specimen 3	60.51	60.55	60.55	60.54
Specimen 4	59.71	59.77	60.28	59.92
	Height h [mm]			
Measurement n	1	2	3	Average
Specimen 1	39.72	40.08	40.30	40.03
Specimen 2	40.92	40.00	40.16	40.36
Specimen 3	40.27	39.97	40.11	40.12
Specimen 4	40.48	40.51	40.56	40.52
	Base Area A [mm^2]		Elastic Modulus E [MPa]	
Specimen 1	2843.48		34.43	
Specimen 2	2812.37		36.15	
Specimen 3	2878.24		39.93	
Specimen 4	2819.90		40.76	

TABLE 6.4: VA 50/6A3 Foam: dimensions of the specimens and apparent Elastic Modulus E calculated according to equation (6.1).

(a)

(b)

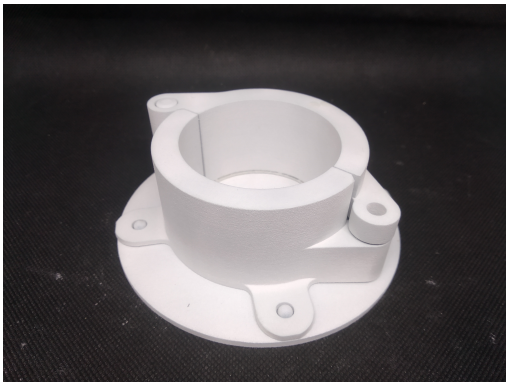

(c)

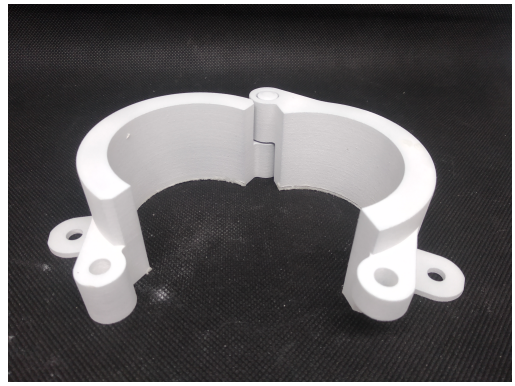

(d)

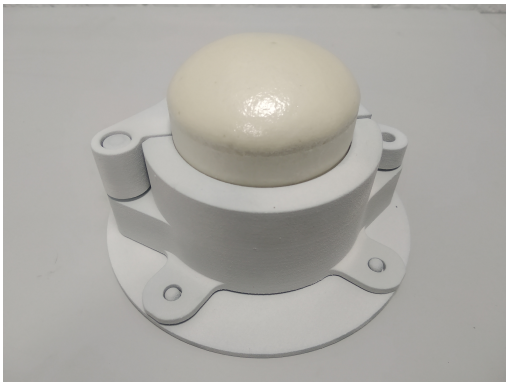

(e)

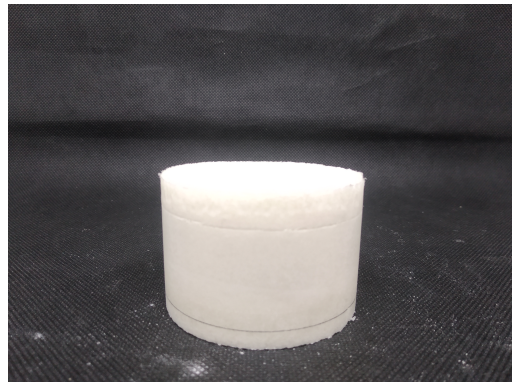

(f)

FIGURE 6.5: Foam specimen preparation: (a) a bi-component foam sample; (b) heated chamber; (c) 3D printed molds; (d) hinge of the mold; (e) foam specimen after expansion; (f) trimmed specimen ready for testing.

6.3 Multiscale Procedure

In the following, the numerical procedure of two-scale scheme involving PWUHS is illustrated. As already mentioned in Chapter 2, in a multiscale analysis, the macroscopic stress $\mathbf{\Sigma}$ is not calculated from $\mathbf{E}$ via a constitutive law but it is obtained solving the microscopic (BVP).
In this procedure the macroscopic stress is obtained from the macroscopic strain $\mathbf{E}$ exploiting the PWUHS scheme illustrated in Chapter 4.
The multiscale procedure can be decomposed in two main parts.
During the precomputations, the average localization matrices $\bar{\mathbf{\Gamma}}^j$ are built according to Section 4.1. To this end a periodic UC of the heterogeneous microstructure is introduced and it is divided in a prescribed amount of m subsets. Three micromechanical linear elastic analyses for each of the m subsets of the UC are performed on the homogeneous elastic *reference material* with elastic matrix $\bar{\mathbf{C}}$, being the overall elastic matrix of the composite material. The three micromechanical problems to solve for the typical s-th subset consist in applying a unit value to each of the polarization stress components, which is homogeneous in the subset according to equation (4.1).
The vectors collecting the average strain fluctuations in the j-th subset due to the polarization stress in Ω^s, according to the approximation in equation (4.5), are stored in the corresponding localization matrix $\bar{\mathbf{\Gamma}}^j$.
The online stage of the multiscale procedure correspond to the solution of the structural problem. To this end the PWUHS scheme is implemented in a finite element code. In this case the ROM homogenization technique has been implemented in a finite element routine in FEAP [96].
The macroscopic structure is discretized in N_e quadrilateral elements with 4 Gauss Points, suitable loads and boundary conditions are assigned.
At the generic time step t the problem is solved simultaneosly at the macroscopic scale and at the coupled microscopic scale, as represented in Fig. 6.6. A UC, divided in subsets, is associated to each macroscopic integration point. The macroscopic strain $\mathbf{E}$ is calculated at each GP and assigned to the corresponding UC as periodic BC, operating the scale transition in equation (2.6).
The microscopic BVP is solved via the PWUHS scheme providing the macroscopic stress value $\mathbf{\Sigma}$ at the integration point and the history variables that have to be stored and passed to the next step.
At this point the global equilibrium at the macroscopic scale can be computed

according to the usual FE scheme:

$$\mathbf{KU} = \mathbf{F}, \tag{6.2}$$

where $\mathbf{K}$ and $\mathbf{F}$ are respectively the global stiffness matrix at the structural scale and the nodal forces vector. The latter can be expresses as:

$$\mathbf{F} = -\sum_{e=1}^{N_e} \int_{\Omega_e} \mathbf{B}^T \boldsymbol{\Sigma} \, dA, \tag{6.3}$$

with $\mathbf{B}$ being the strain matrix and $\boldsymbol{\Sigma}$ being the average stress obtained using the PWUHS scheme; in a usual FE scheme, the stress would have been obtained calling the local constitutive law.
In the present work, a constant tangent stiffness $\bar{\mathbf{C}}$ is adopted at the macroscale during the loading process. A different approach can be to compute the consistent effective tangent stiffness or the algorithmic tangent stiffness at the end of each time step.

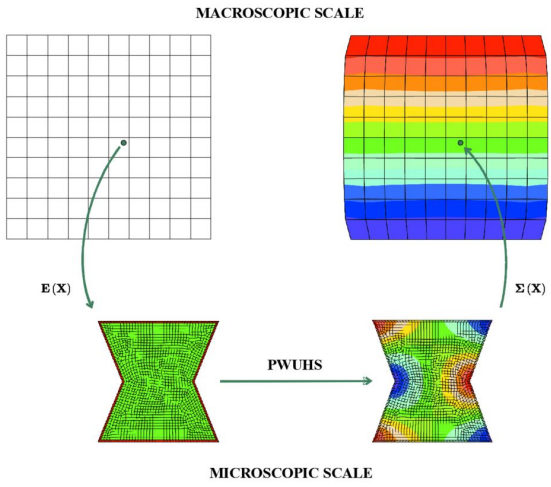

FIGURE 6.6: Multiscale procedure scheme.

6.4 Numerical applications

In this Section, numerical applications are developed in order to evaluate the accuracy of the proposed multiscale scheme.

The two-scale technique described in the previous subsection is tested on a periodic auxetic structure composed by two different constituents; in particular, a foam-filled auxetic honeycomb with a re-entrant hexagonal frame is considered. First, a focus on the microstructure is made in order to identify a UC satisfying the periodicty conditions, allowing the application of periodic boundary conditions. The response of the UC, divided in subsets and subjected to simple loading cases, is studied adopting the PWUHS approximation. Results are compared to the FEA reference solution.
A homogeneous macroscopic model is then introduced in order evaluate the performaces of the two-scale procedure. The auxetic UC is associated to each structural integration point and the multiscale analysis are carried out using the software FEAP, in which a "user element" for the solution of the microstructural BVP on the UC via the PWUHS approach, has been implemented.
The results of the Multi-Scale analyses are compared to the results of Nonlinear Finite Element Analyses carried out on the heterogeneous auxetic honeycomb model.

6.4.1 UC Homogenization

The identification of the UC strongly depends on the geometry of the composite material. In order to identify a periodic UC, a periodicity direction running through the microstructure, must be provided.
In the case of re-entrant hexagonal honeycombs, non-orthogonal periodicity directions can be identified for the generation of a generic auxetic pattern, that is obtained by the periodic repetion of a single re-entrant hexagon along the skewed directions x_1 and x_2:

$$x_1 = h_1 e_1 + h_2 e_2, \qquad x_2 = H e_2, \tag{6.4}$$

where h_1 is the UC translation in the horizontal direction, h_2 is the vertical overlapping between the UC's, H il the height of the UC, as shown in Fig. 6.7.
Similar approaches for the generation of repetitive patterns are commonly used in the framework of masonry structures homogenization [97, 98].
In order to do not violate the material continuity along the skewed periodicity directions, the UC is considered having half the wall thickness of the auxetic frame (see Fig. 6.8).

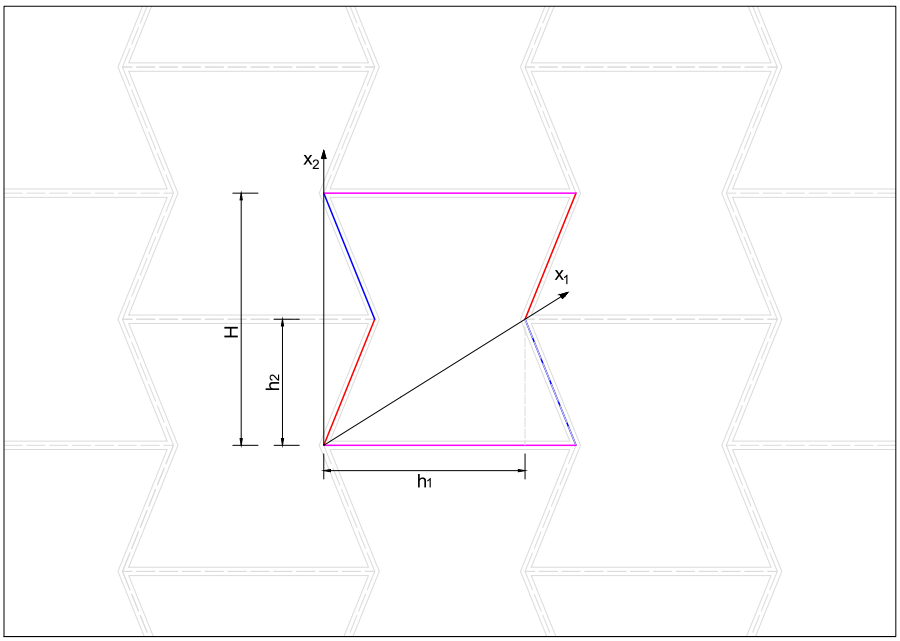

FIGURE 6.7: UC identification in re-entrant hexagonal auxetic honeycomb pattern; skewed periodicity directions x_1 and x_2.

The re-entrant hexagonal UC has been modeled according to the geometrical parameters in [76]: the resulting characteristic lengths of the UC in the longitudinal and transversal directions, the wall thickness of the frame and the inclination angles of the oblique rods are reported in Fig. 6.8.

The re-entrant hexagonal periodic unit cell with auxetic behaviour, denoted by UC-A, is represented in Fig. 6.9. It is composed by a plastic re-entrant hexagonal frame with volume fraction $c^1 = 0.09$, having the characteristic material properties of a 3D printable PA 12 reported in Table. 6.1 and the geometrical properties in Fig. 6.8, filled with an elastoplastic PU Foam having material properties reported in Table. 6.2 and volume fraction $c^2 = 0.91$.
The two constituents are respectively discretized in 6 subsets, corresponding to the external elastoplastic rods, and a single subset for the foam filler, thus, the total amount of internal variables for the single UC is $(3 + 1) \times 7 = 28$.
UC-A is analyzed under both plane strain and plane stress condition, considering a monotonic loading history in terms of the average macroscopic strain E_{22}, until the value of 0.1 (Load Case 5, LC-5) is reached. Results obtained via PWUHS are compared to the FE reference solution, obtained discretizing the UC-A in a

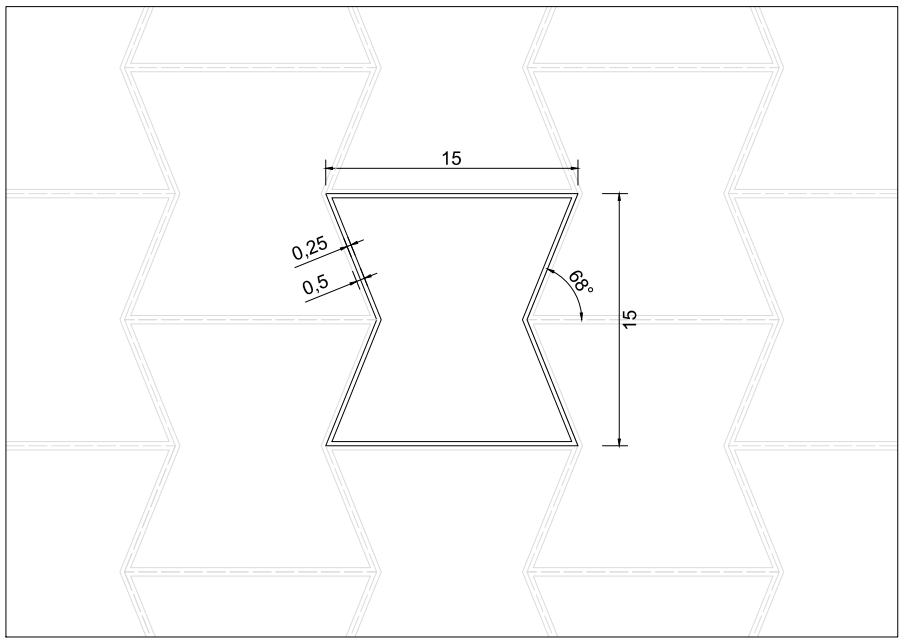

FIGURE 6.8: Geometrical properties of the Foam-filled Auxetic Honeycomb UC-A.

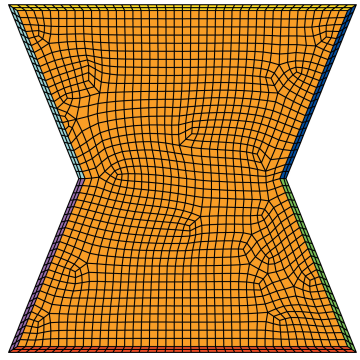

FIGURE 6.9: UC-A discretized in 7 subsets.

mesh of 1790 elements ($4 \times 1790 = 7160$ history variables).
The overall nonlinear response of the auxetic composite material in terms of the macroscopic stress Σ_{22} versus E_{22} and Σ_{11} versus E_{22}, in plane strain framework, are respectively illustrated in Figs. 6.10-6.11. Results are compared to a FE reference solution adopting 2D plane strain four-nodes elements implemented in FEAP.
Numerical results show that the PWUHS homogenization technique, using the computationally derived reference elastic matrix $\mathbf{C}_0 = \bar{\mathbf{C}}$, succeeds in predicting the auxetic behaviour of the foam filled honeycomb; the stress response of the UC in x_1 direction (Fig. 6.11), have opposite sign in comparison to the stress in the loading direction, being perpendicular to x_1, due to the overall negative poisson's ratio of the composite material.
The stresses along the loading direction are underestimated in the initial linear phase, while in the plastic branch stresses converge to FE solution.
The stresses along x_1 direction are roughly predicted during the whole loading history. Even if a sensible relative error occurs at the final step (0.148), the overall trend is captured with a considerable reduction of the degrees of freedom, which amount are respectively $13 \times 7 = 91$ in the PWUHS scheme and $2 \times 4 \times 1790 = 14320$ in the FE model.

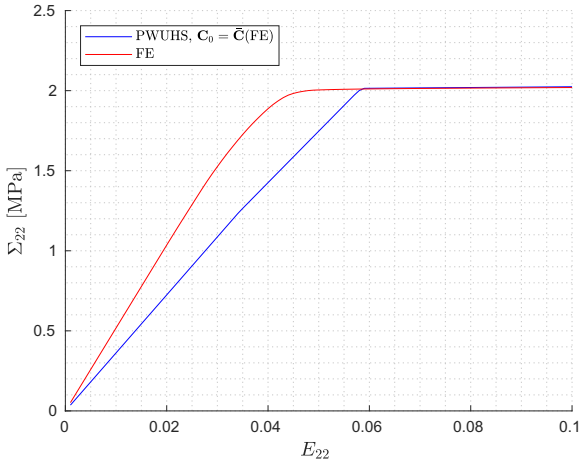

FIGURE 6.10: Macroscopic stress Σ_{22} in auxetic UC-A considering plane strain condition.

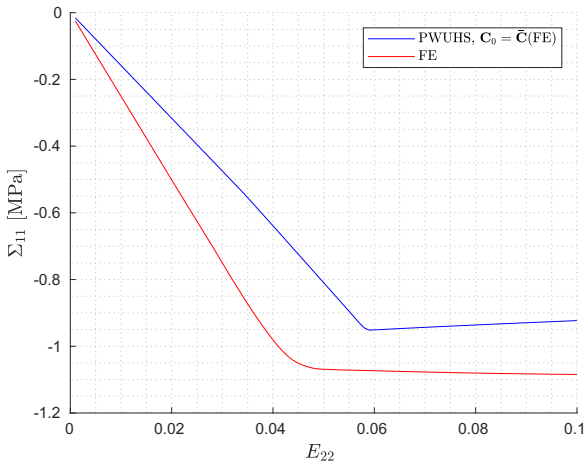

FIGURE 6.11: Macroscopic stress Σ_{11} in auxetic UC-A considering plane strain condition.

UC-A is then considered, under the hypothesis of plane stress condition, subjected to LC-5; results are compared to a FE solution adopting 2D plane stress four nodes quadrilateral user defined element in FEAP. Similar considerations can be made in comparison to the plane strain problem. A slight increase of the error is observed in the elastic response for the approximation of both macroscopic stress components Σ_{11} and Σ_{22}.

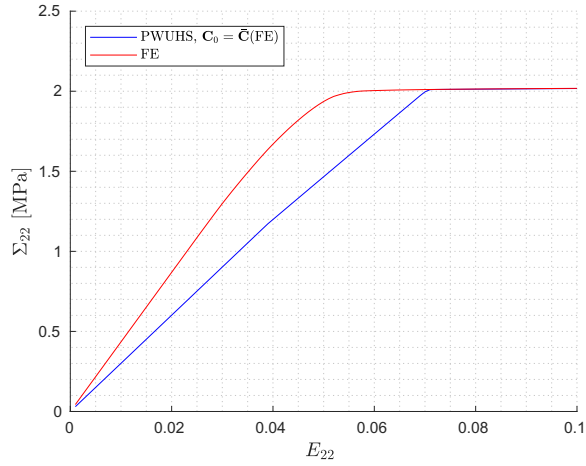

FIGURE 6.12: Macroscopic stress Σ_{22} in auxetic UC-A considering plane stress condition.

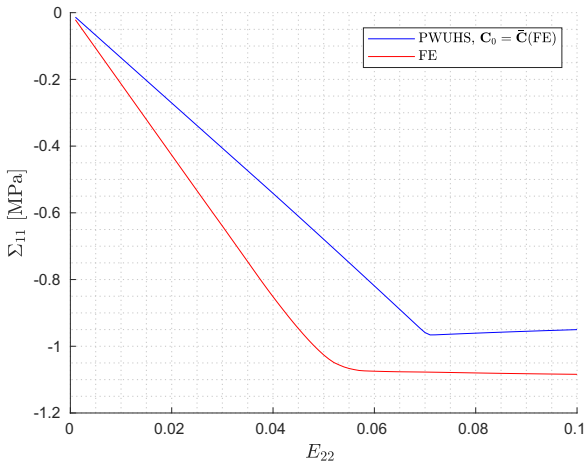

FIGURE 6.13: Macroscopic stress Σ_{11} in auxetic UC-A considering plane stress condition.

6.4.2 Multiscale Analysis of Auxetic Honeycomb

A structural problem is here introduced and solved according to the multiscale procedure illustrated in Section 6.3. In particular, the two-dimensional auxetic honeycomb structure in Fig. 6.14, is considered subjected to a uniformly distributed vertical displacement on the top edge, with the bottom edge fully constrained.

The structural model is composed by 99 re-entrant hexagonal honeycomb which dimensions are reported in Fig. 6.15, left.

In order to solve the multiscale analysis of the auxetic structure, an homogeneous macroscopic model discretized in 100 elements is introduced (Fig. 6.15, right). The UC-A microstructure introduced in the previous section (Fig. 6.9), which is made of a PA 12 auxetic frame filled with PU foam, is discretized in 7 subsets and associated to each integration point of the homogeneous macroscopic model (400 Gauss Points). At each Gauss point, the history variables of the UC-A are stored, thus, the total number of history variables is $7 \times 4 \times 400 = 11200$. The macroscopic model is subjected to a uniformly distributed vertical displacement $U_0 = -10$ mm (7.5% of deformation in compression), applied on the top edge during a quasi-static analysis. The results of the multiscale analysis, alternately assuming plane strain and stress condition, are compared to a reference nonlinear FE solution, obtained using the commercial software Abaqus®.

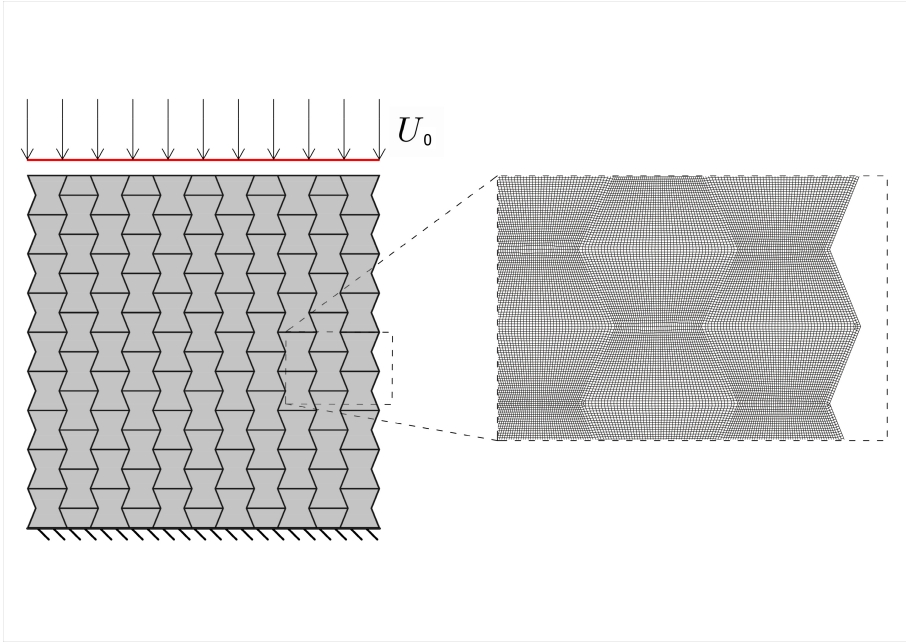

FIGURE 6.14: Heterogeneous structure composed by a foam filled auxetic frame and its FE discretization in 320286 quad elements; a close-up view of the reference mesh generated in Abaqus is shown.

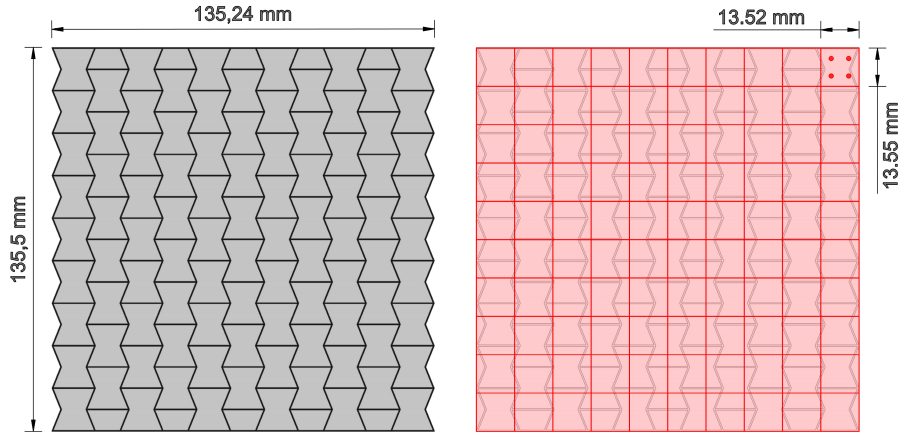

FIGURE 6.15: Heterogeneous structure dimensions (left); homogeneous macroscopic model dimensions and discretization in a mesh of 10×10 elements.

In order to obtain a proper discretization, the reference mesh has been progressively refined in order to avoid elements' excessive distortion and to ensure mesh independency. Finally, the structural geometry (Fig. 6.14, left) has been discretized in a mesh of 320286 quadrilateral finite elements.
Considering 4 history variables for each Gauss point, the total number of history variables of the FE model is $4 \times 4 \times 320286 = 5124576$. The number of history variables that have to be stored at each time step is reduced up to 99.781 % and the number of equations which defines the computational effort, is significantly lower in the multiscale approach.
Results in terms of the resultant force F, obtained under plane strain hypothesis as of the sum of the nodal reactions on the constrained top edge, are plotted in Fig. 6.16 with respect to the prescribed displacement U_0 .

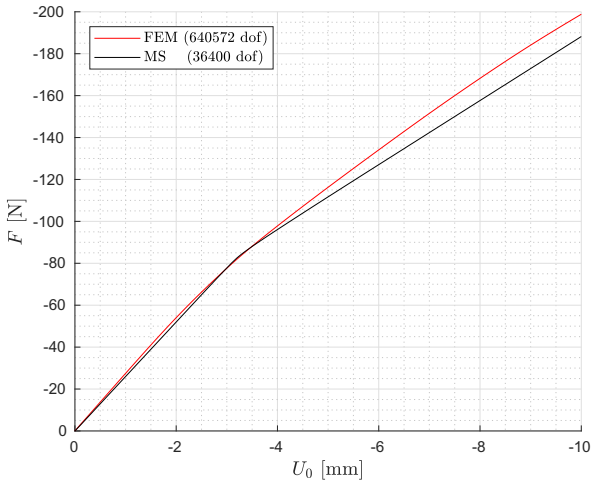

FIGURE 6.16: Comparison between FE analysis and the proposed Multiscale Analysis scheme: force-displacements curve in plane strain condition.

The results of the Multiscale analysis are in agreement with the reference nonlinear FE analysis. A low stiffness underestimation is observed in the final part of the loading history, with a maximum relative error equal to 0.07. The overall response of the heterogeneous structure is definetely captured, with the benefit of a drastic reduction of the degrees of freedom and, hence, of the computational cost.
Figures 6.17 and 6.18 show the distributions of displacements along the X_1 direction at the final step, respectively obtained from Multiscale analysis and

nonlinear FE analysis. In both cases a concentration of the horizontal displacements, in correspondence of the unconstrained vertical edges, is observed. Due to the axial symmetry of the geometry, opposite values of the displacements are observed along the vertical parallel edges, leading to the consequent reduction of the middle horizontal section, according to the auxetic behaviour. Maximum values of the horizontal displacements, got via the Multiscale analysis, are comparable to the FE reference results.

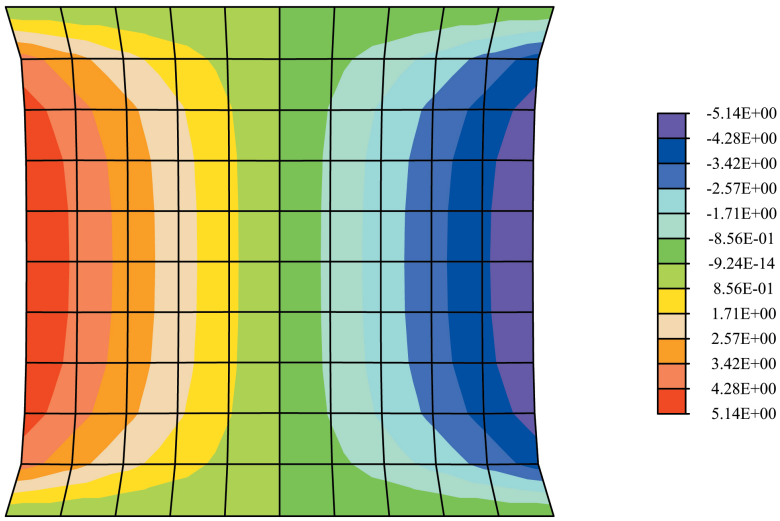

FIGURE 6.17: Distribution of the horizontal displacements U_1 at the end of Multiscale analysis.

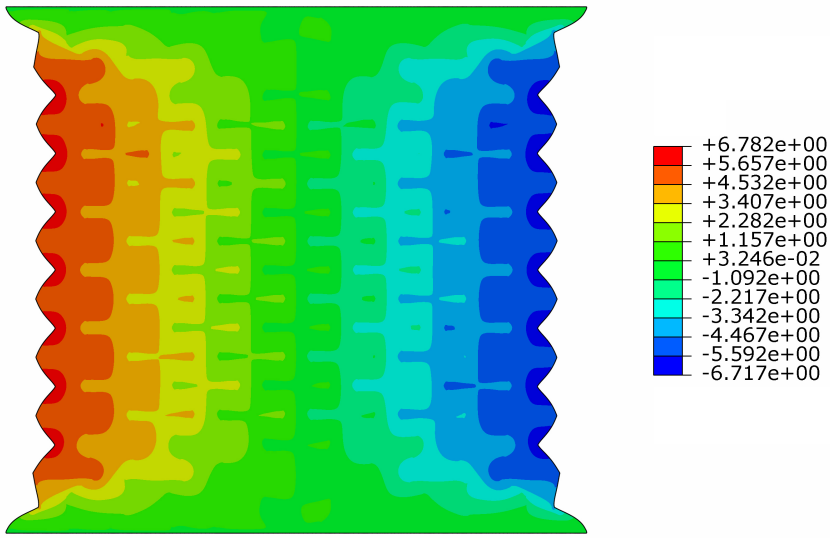

FIGURE 6.18: Distribution of the horizontal displacements U_1 at the end of nonlinear FE analysis.

The multiscale analysis of the auxetic structure is then performed assuming plane stress condition and results in terms of the resultant force F, versus the prescribed displacement U_0, are plotted in Fig. 6.19.

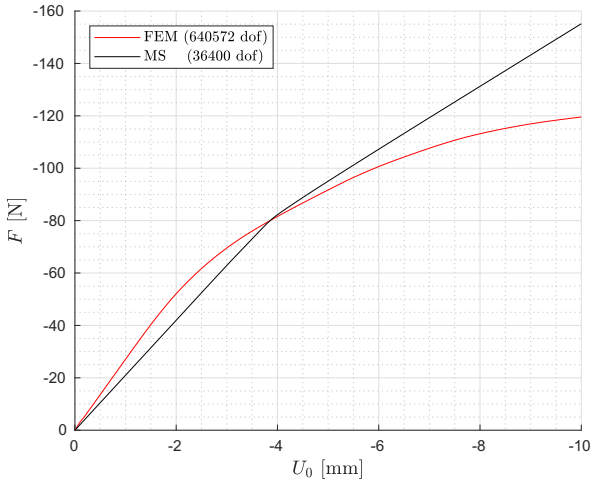

FIGURE 6.19: Comparison between FE analysis and the proposed Multiscale Analysis of auxetic structure: force-displamcements curve in plane stress conditon.

The accuracy of the proposed multiscale scheme is lower in comparison to the

equivalent application under plane strain condition; as seen in the homogenization of the UC-A (see Fig. 6.12), the response in the elastic regime is coarsely approximated and, in addition, the smooth increase of the plastic deformation of the reference FE analysis is not captured due to an overprediction of the overall stiffness. The results are probably influenced from the arising of locking phenomena, limiting the deformation of the auxetic structure and causing the element to reach the equilibrium with smaller displacements, as can be noted comparing the displacement maps of the structure at the last step of the multiscale analysis 6.20 and of the FE reference analysis 6.21.

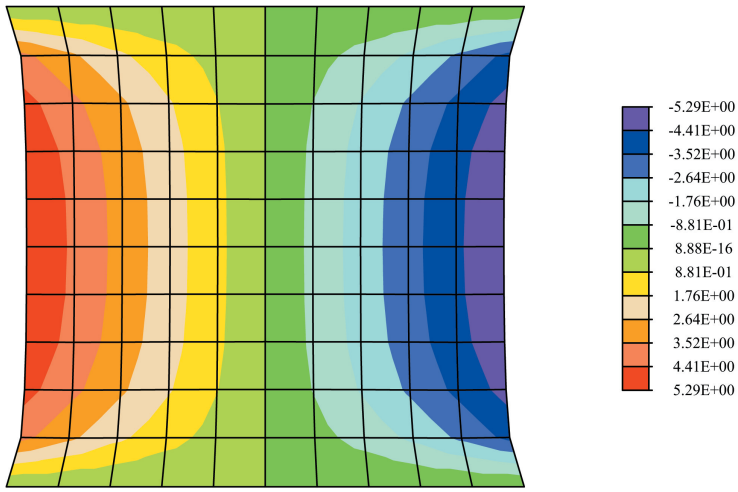

FIGURE 6.20: Distribution of the horizontal displacements U_1 at the end of Multiscale analysis.

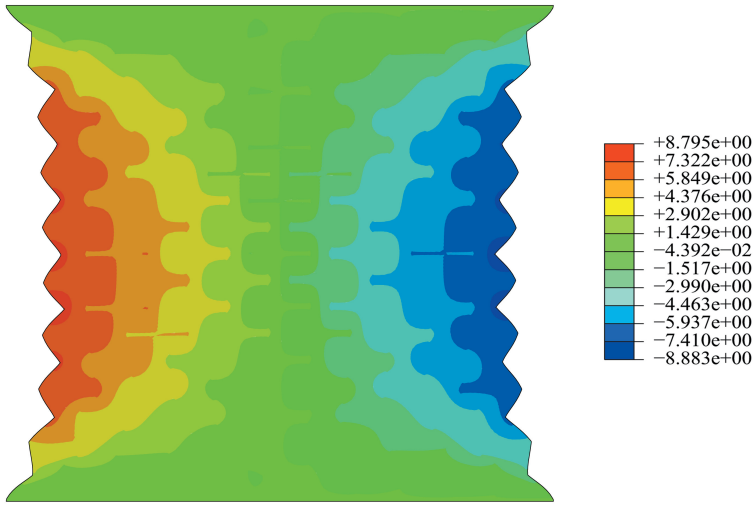

FIGURE 6.21: Distribution of the horizontal displacements U_1 at the end of nonlinear FE analysis.

Equal and opposite results are obtained subjecting the macroscopic model to a uniformly distributed vertical displacement $U_0 = 10$ mm (7.5% of deformation in tension), alternately assuming plane strain (Fig. 6.22 a, c, e) and plane stress (Fig. 6.22 b, d, f) conditions; the main difference lies in the deformation mode of the auxetic structure, which expand at right angles to the applied tension.

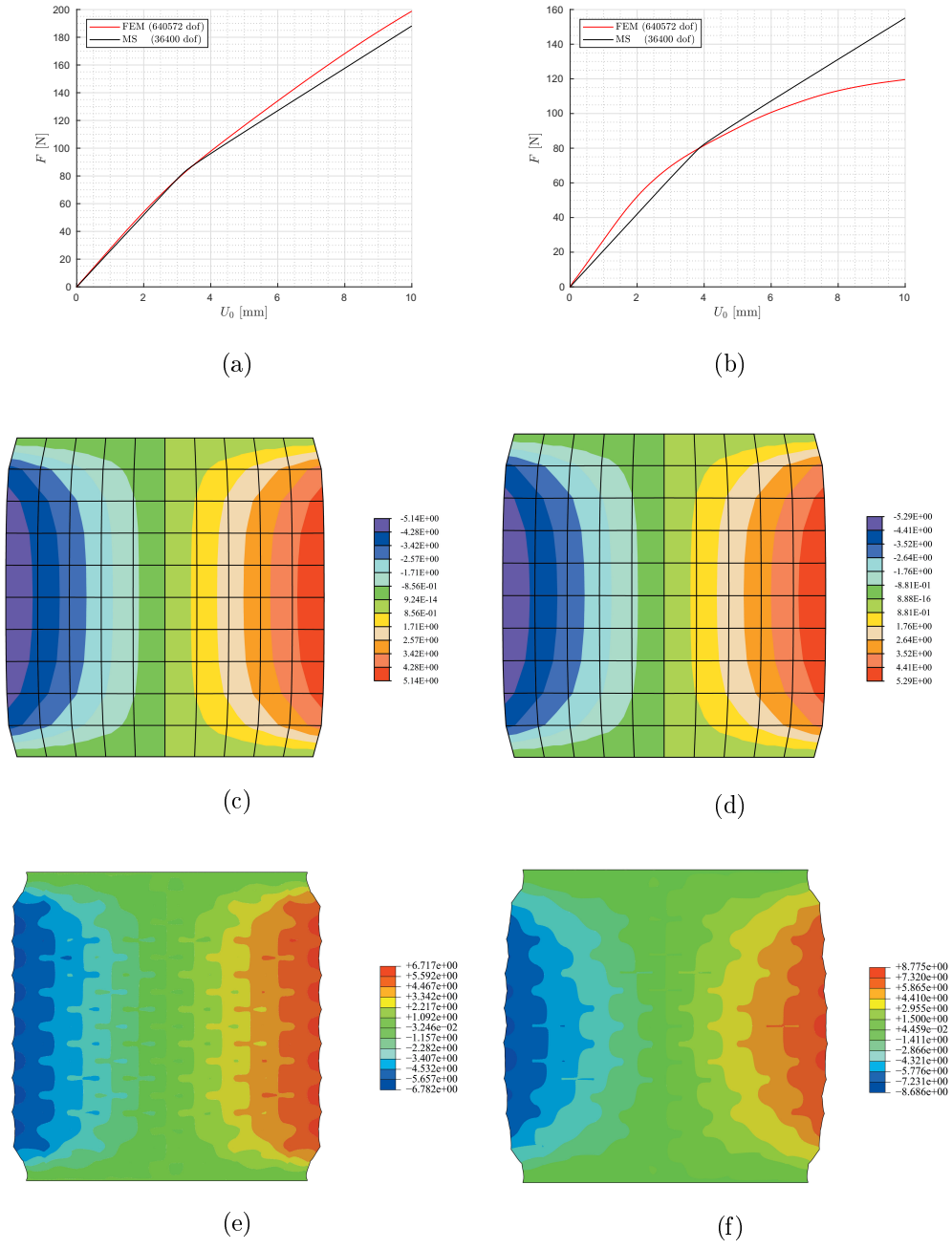

FIGURE 6.22: Comparison between FE analysis and the proposed Multiscale Analysis scheme: force-displacements curve in plane strain (a) and plane stress (b) condition; maximum horizontal displacements U_1 of Multiscale and FE analyses in plane strane condition (c, e) and plane stress condition (d, f).

In order to numerically demonstrate mesh independency of the proposed model, an additional computation, under plane strain hypothesis is performed adopting a coarser discretization at the structural level (see Fig. 6.23). The macroscopic model in Fig. 6.15, left, is discretized in 25 quadrilateral elements with 4 Gauss Points, thus, the total number of history variables is $7\times4\times4\times25 = 2800$. This macroscopic discretization, having a total amount of 100 GP with each point associated to a single UC, reproduce to the fullest the geometry of the structural model composed by 99 re-entrant hexagonal honeycombs.
Despite the further reduction in the number of degrees of freedom, the result of the multiscale analysis is close enough to the FE reference solution (Fig. 6.24), proving that the proposed multiscale scheme is not affected by mesh-dependency issues.
According to results in Fig. 6.24 it is possible to state that in multiscale analyses, in the limit of the principle of scale separation, a relative coarse mesh in relation to the overall structural dimensions can be adopted without affecting the method accuracy.

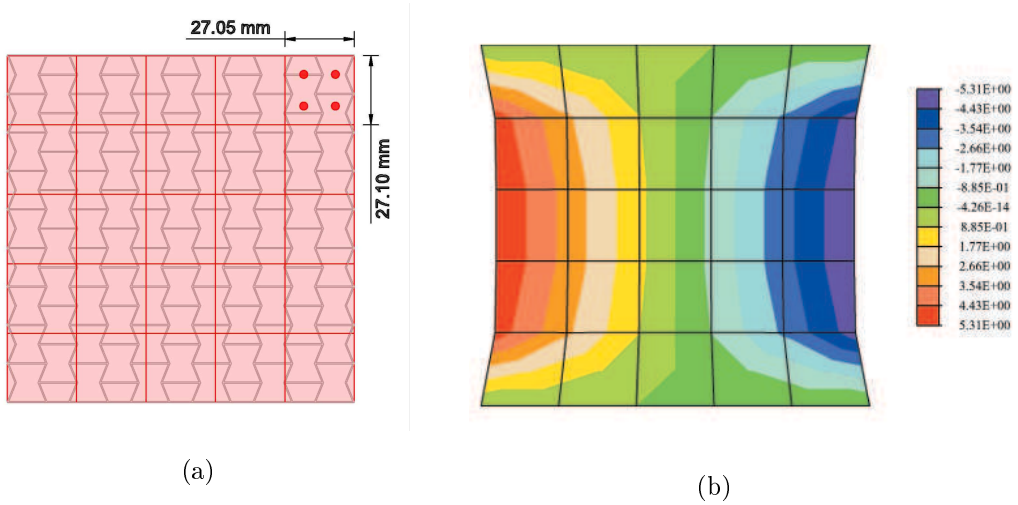

(a) (b)

FIGURE 6.23: Homogeneous macroscopic model elements dimensions and discretization in a mesh of 5×5 elements (left); maximum horizontal displacements U_1 of Multiscale analysis in plane strane condition, obtained using a 25 elements discetization (right).

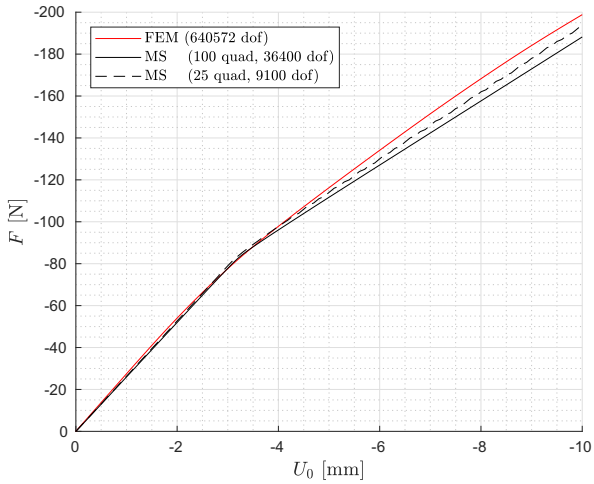

FIGURE 6.24: Comparison between FE analysis and the proposed Multiscale Analysis of auxetic structure under compression: force-displamcements curve (in plane strain conditon) obtained performing Multicale Analyses using different discretizations at the structural level.

Numerical validation of the proposed multiscale scheme is given comparing the structural behaviour of a macroscopic model to the response of a single homogenized UC (Fig. 6.9). In particular, a large macroscopic composite structure (271x271 mm), discretized in 400 quadrilateral 4 GP elements, is considered undergoing a prescribed displacement in compression ($U_0 = -20$mm, 0.074 strain); the obtained stress-strain curve is compared to the results obtained considering UC-A (Fig.6.10) periodically constrained, thus, consistent BC are chosen at the macroscopic level. In this case the structure is horizontally constrained along the vertical edges. The results shown in Fig. 6.25 prove that results of multiscale analysis of an auxetic composite structure are in agreement with the response of a homogenized UC.

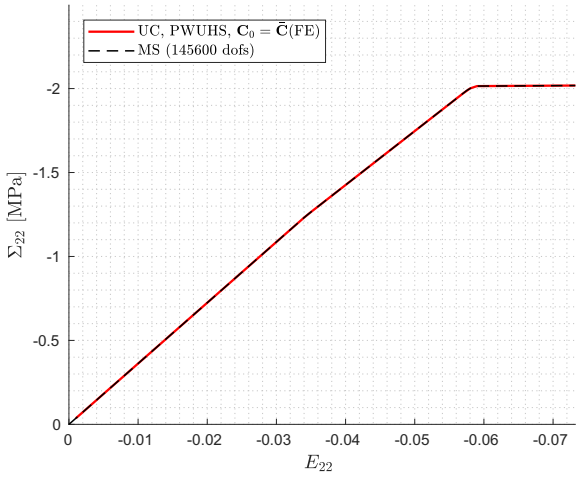

FIGURE 6.25: Comparison between the stress-strain curves obtained from Multiscale analysis of a composite structure (foam-filled auxetic haneycomb) with dimensions 271x271mm, discretized in 400 elements and the PWUHS homogenization on the underlying UC with periodic BC.

6.5 Experimental Validation

The response of the auxetic structure considered in Section 6.4.2, is experimentally evaluated, with the aim of validating the proposed Multiscale analysis scheme. A focus on the manufacturing process of the composite specimen is first made. Then, the results of the experimental investigations are presented and compared to the numerical counterpart.

6.5.1 Design and manufacturing of Foam-filled Auxetic Honeycomb

A 3D printed polymeric honeycomb with re-entrant hexagonal geometry, filled with the DP 25/10B1 elastoplastic foam characterized in Section 6.2.2, is subjected to uniaxial compression and tension in quasi-static regime. The specimen geometry is obtained from extrusion of the planar model in Fig. 6.14 (left), resulting in a "primastic" body with a length of 135.24 mm, a height of 135.5 mm and a depth of 31 mm (Fig. 6.26).

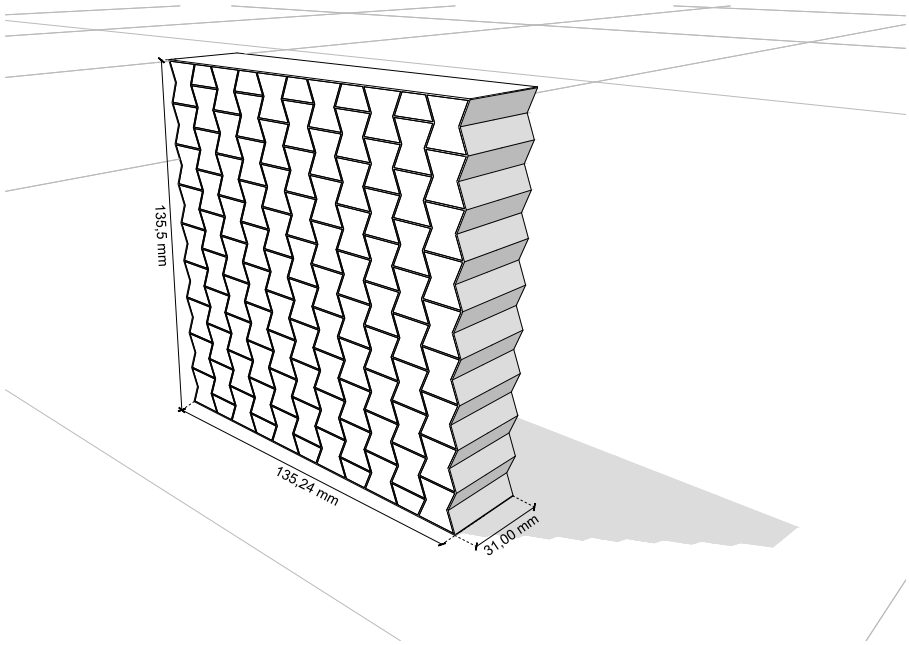

FIGURE 6.26: Dimensions of the 3D specimen.

The polymeric honeycomb frame is 3D-printed using the HP Multi Jet Fusion (MJF) technology, a Powder Bed Fusion (PBF) additive manufacturing (AM) technique for the manufacture of polymeric components made of PA 12 (see Section 6.2.1), having the mechanical properties reported in Table 6.1. In contrast to the other most common PBF technolgies, such as Selective Laser Sintering, the energy source in MJF is a group of infrared lamps which activate the fusing agent, previously applied on the interest areas in combination to a defining agent, which is applied on the surrounding areas in order to prevent the fusion of the polyamide. This technique allows for the production of smooth and sharp edges with a dimensional accuracy of $\pm 0.2\%$, a fundamental requirement for the production of the desired thin-walled frame having a thickness of 0.5 mm.
In order to replicate the numerical boundary conditions employed in the multiscale analysis of the foam-filled honeycomb, where the horizontal displacements at both the upper and lower limits of the specimen are constrained, attention is payed to the design of the upper and lower faces of the specimen. In particular, the auxetic frame is 3D printed with the addition of two solid *undeformable* bars at the top and bottom ends of the specimen (Fig. 6.27) which role is to uniformly distibute the imposed vertical displacement all over the horizontal faces, constraining the displacements in X_1 direction. Two cylindrical elements,

designed for the collocation of the specimen in the testing machine, are solidly printed at the top and bottom ends.

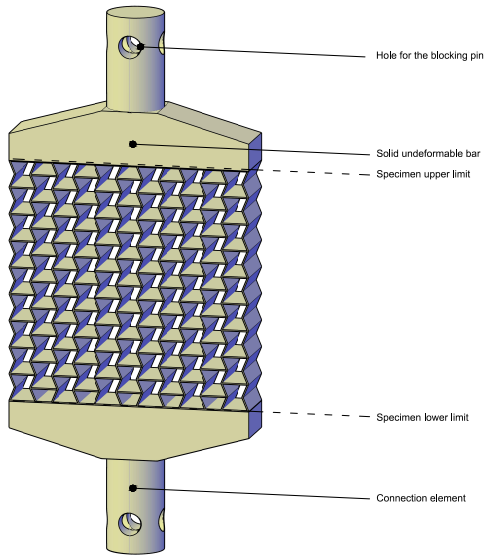

FIGURE 6.27: Design of the polymeric frame for the experimental tests.

6.5.2 Results and Discussion

Two specimens of the 3D printed auxetic honeycomb are manufactured and filled with the rigid DP 25/10B1 PU foam, having material properties reported in Table 6.2. The specimens are used for the experimental evaluation of the proposed multiscale procedure: aim of the tests is to compare the experimental results with the numerical counterpart, in terms of the resultant force F, obtained as of the sum of the reactions on the top edge, and in terms of the maximum displacements along the X_1 direction, detected at the end of the loading process. The specimens are respectively tested in compression and tension, using the MTS Insight Testing System (MTS System Corporation), equipped with a 10KN load cell and presented in section 6.2.2.

The first specimen (Specimen-1) undergoes a prescribed vertical displacement $U_0 = -10$ mm (7.5% of deformation in compression) with constant load-rate 8 mm/min.

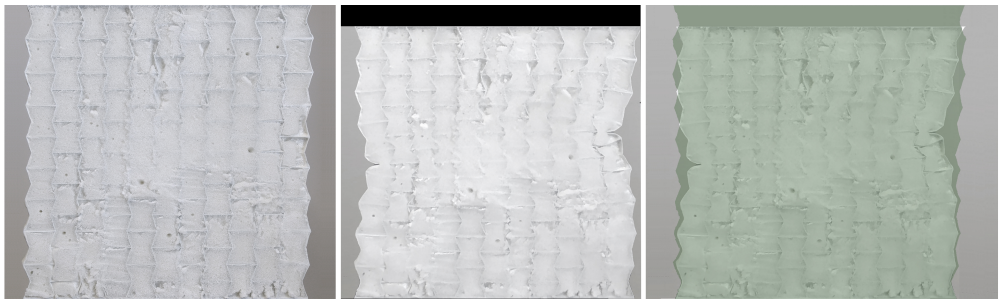

FIGURE 6.28: Specimen-1 tested in compression: undeformed configuration (left), deformed configuration at the end of the loading process (middle), comparison between the undeformed configuration, in green, and the deformed configuration at the end of the loading process (right).

Experimental investigation of the foam-filled auxetic honeycomb under compression shows the arising of buckling phenomena, influencing the collapse of the structure. First, the specimen cross-section undergoes a progressive thinning along the X_1 direction, according to the auxetic behaviour. As the imposed displacements increase, the inelastic deformations concentrate at points along the specimen sides, causing the formation of plastic hinges (Fig. 6.28, middle). Two non-aligned hinges (one per side) approximately located in the central part of the specimen, become dominant, causing the relaxation of the loads at the other locations of the specimen.

It follows that a comparison of the experimental results with the numerical counterpart, which is obtained assuming small strain regime, is unnecessary. Further research is needed for the formulation of the proposed ROM technique and Multiscale analysis scheme in the framework of finite strain.

The second specimen (Specimen-2) undergoes a prescribed vertical displacement $U_0 = 10$ mm (7.5% of deformation in tension) with constant load-rate 8 mm/min.

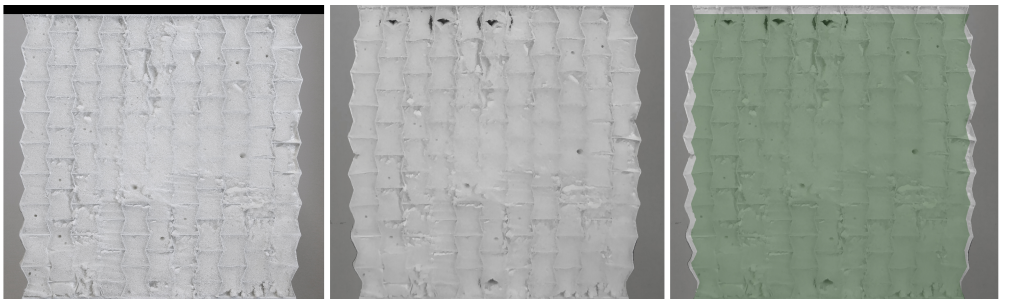

FIGURE 6.29: Specimen-2 tested in tension: undeformed configuration (left), deformed configuration at $U_0 = 4.6$ mm (middle), comparison between the undeformed configuration, in green, and the deformed configuration at $U_0 = 4.6$ mm (right).

Experimental investigation of the foam-filled auxetic honeycomb subjected to uniaxial tension delivers results for a comparison with the numerical counterpart. The deformation of Specimen-2 is in agreement with the numerical analysis and shows auxetic behaviour during the first part of the loading process, as shown in Fig. 6.29; when the value of $U_0 = 4.6$ mm is reached, the failure of the composite honeycomb occurs due to the decohesion at the interphase between the PA12 frame and the foam filler. Forces converge in the auxetic frame that brakes due to the concentrated loads.

A comparison between the numerical and experimental results in terms of the resultant force F, obtained as of the sum of the reactions on the top edge, is illustrated considering the experimetal output collected before failure at $U_0 = 4.6$ mm. In Fig. 6.30 experimental results in terms of the resultant force F, versus the prescribed displacement U_0, are compared to the Multiscale analysis results and to the FE reference solution, assuming plane stress condition (Fig. 6.30, left) and plane strain condition (Fig. 6.30, right). Since the thickness of the model is far smaller in comparison to the planar dimensions (see Fig. 6.26), the specimen can be imagined as thin plate with stresses acting along its plane, thus, a comparison with numerical results obtained in the framework of plane stress may be assumed the most suitable. The maximum gap between the experimentally derived reaction force F and the Multiscale analysis results in plane stress condition, measured as a relative error, is equal to 0.084. Is interesting to note that the results of Multiscale analysis are even closer to the tensile test output in comparison to the FE reference solution (error equal to 0.108).

Similar considerations are made considering the plane strain numerical counterpart. In this case the maximum gap between Multiscale analysis and the tensile test results is just 0.072, even lower of the gap regarding the FE reference solution (0.107).

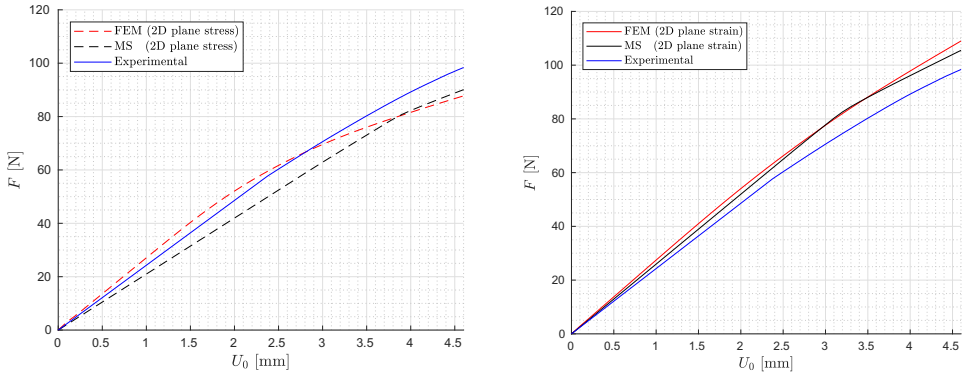

(a) (b)

FIGURE 6.30: Comparison between experimental results of tensile test on Specimen-2 and numerical results obtained via Multiscale analysis and FE analysis assuming plane stress (a) and plane strain (b) condition.

Further considerations are made comparing the maximum displacements along the horizontal direction at the last available experimental loading step ($U_0 = 4.6$ mm), detected at prescribed points referred as A and B in the undeformed configuration (see Fig. 6.31, a), with the displacement maps of the numerical FE analysis (Figs. 6.32 and 6.33).
The distances between the couple of points A-A' and B-B', along X_1 direction, are respectively equal to 3.3 mm and 3.2 mm, hence in agreement with the FE reference solution.

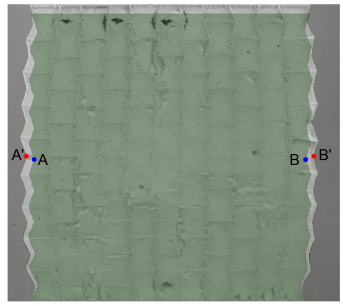

FIGURE 6.31: Position of the points for horizontal displacements measure on Specimen-2, in the undeformed configuration (A, B) and in the deformed configuration (A', B').

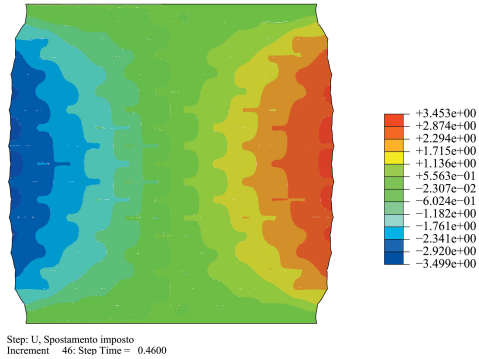

FIGURE 6.32: Displacement map at $U_0 = 4.6$mm, 2D FE analysis of the auxetic honeycomb in plane stress condition.

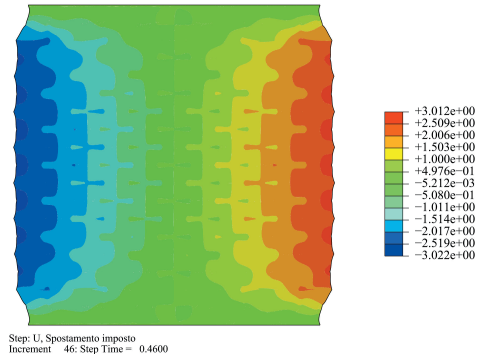

FIGURE 6.33: Displacement map at $U_0 = 4.6$mm, 2D FE analysis of the auxetic honeycomb in plane strain condition.

Both the values of the maximum reaction force F and of the pointwise horizontal displacements in A and B, have values in between the numerical counterparts, obtained via Multiscale Analysis, in plane strain and plane stress condition. This suggests that neither the first nor the second assumption suit the experimental layout; a possible solution could be provided from 3D analysis of the auxetic foam-filled honeycomb, considering the true thickness of the specimen.

Experimental investigations prove the efficiency of the proposed PWUHS homogenization in the framework of Multiscale analysis; the behaviour of composite materials is approximated with a drastically reduced number of internal variables and computational cost, coming at the expense of a reasonable error in comparison to the FE analyses.

Chapter 7

Conclusions

In line with the increasing usage and performance requirements of structures made of heterogeneous materials, the need of efficient numerical tools to adopt during the design process has became an open issue in both scientific and industrial research. Multiscale modeling has gained popularity in the analysis of heterogeneous materials, also referred as composites, as a powerful tool considering two coexisting scales: the macroscale at the structural level and the microscale tipycal of the material level. With the structural response strongly depending from the inelastic phenomena arising at the microscale, an efficient homogenization scheme is needed, in the framework of multiscale analysis of composite material, in order to obtain the macroscopic response of an equivalent homogeneous material from the solution of a micromechanical problem. Among the homogenization schemes, Reduced Order Models combine the accuracy of the computational homogenization schemes and the efficiency of the analytical homogenization schemes.

The main scope of the research reported in this dissertation is to provide an efficient tool for the multiscale analysis of composite materials characterized by nonlinear response. A reduced order homogenization scheme, namely the Piecewise Uniform Hashin-Shtrikman (PWUHS) has been introduced in Chapter 4 with the aim of developing a novel multiscale scheme in which PWUHS is adopted for the solution of the problem at the microscopic level. The problem is formulated for a large class of periodic composites and different Unit Cells, representative of randomly distributed heterogeneous material, are studied. Following the Hashin-Shtrikman variational formulation, a homogeneous elastic reference media is introduced together with a polarization stress (an eigenstress) describing the stress gap between the heterogeneous material and the reference material. A novel approach for the calculation of the elastic reference matrix during an

offline phase is proposed, adopting the FE homogenization of the composite. A piecewise uniform distribution of the eigenstress is considered for the coupling of the reference material with the heterogeneous material, which is divided in subsets according to the constituents distribution. The evolution of the inelastic strain is governed by the average stress in each subset and it is solved simultaneously in all the subsets via a Newton Raphson procedure for the correction phase in the predictor-corrector algorithm within the finite step. With the dimension of the problem depending on the low number of subsets, a noticeable advantage in terms of computational cost and time is provided for the homogenization of composite materials, in comparison to FE analyses. The advantages of the proposed PWUHS are confirmed from various numerical applications even for complex loading-unloading histories. The main novelty of the proposed ROM technique is the possibility to consider materials which behaviour is in agreement with the Mises plasticity model with linear isotropic hardening. The PWUHS presents another great advantage as it can be significantly improved by implementing the secant approach to update the reference material, leading to a very fast convergence towards the FE solutions and to very accurate numerical results in all the performed applications.

In Chapter 5 a comparative study between the proposed PWUHS and the PWUTFA homogenization schemes is illustrated, starting from the similarities between the two techniques. In both homogenization procedures the UC is discretized in subsets, inside which the PWUTFA assumes the inelastic strain constant, while the PWUHS assumes the polarization stress constant. In both PWUTFA and PWUHS an offline calculation is required for the construction of the localization matrices and, during the online phase, the evolution of the inelastic strain is governed by the average stress in each subset and it is simultaneously solved in all the subsets. The equivalence between the two approaches is proven and verified through numerical investigations, furnishing numerical evidences of the equivalence between the two reduced order methods for composites having the same elastic properties. To the author knowledge, no such evidences are found in the literature. For the same composite material a convergence study is carried out for both model order reduction techniques highlighting that increasing the number of subsets PWUTFA and PWUHS results tend toward to FE solution. Numerical applications have been carried out on composites having different material properties; all the presented numerical results show that for a low number of subsets, the PWUTFA results are more accurate with respect to

the PWUHS solution, while increasing the subset number the PWUHS is more effective. Furthermore, implementing the secant modulus correction of the reference elastic matrix, leads to very accurate numerical results in all the performed applications in comparison to the PWUTFA, at the expense of a negligible increase of the computational time. In Chapter 6 the proposed PWUHS is used in the framework of Multiscale analysis to derive the overall response of auxetic composites, in order to assess the efficiency of the proposed homogenization technique. The PWUHS homogenization is implemented in a finite element code (FEAP). The macroscopic structure is discretized in quadrilateral elements and at each time step the problem is solved simultaneosly at the macroscopic scale and at the coupled microscopic scale. A UC, divided in subsets, is associated to each macroscopic integration point and the microscopic problem is solved via the PWUHS scheme, providing the homogenized response at the coresponding macroscopic material point. The composite material considered for the numerical applications is made by a 3D printed auxetic honeycomb frame, filled with a polyurethane foam being much less stiff in comparison to the outer frame. The results of the numerical applications show the accuracy of the proposed Multiscale analysis scheme. The overall response of the auxetic structure is predicted with the benefit of a drastically reduced number of the degrees of freedom and computational cost, at the expense of a reasonable error, in comparison to the FE reference solution. The results of the Multiscale scheme are validated via experimental tests made on foam-filled auxetic honeycomb. The response of the investigations are compared to the results of the two dimensional Multiscale analyses, proving the capability of the two-scale scheme in predicting the failure in composite materials.
The agreement between numerical and experimental findings is a valuable target for the proposed reduced order homogenization scheme and for the research presented in this dissertation. A reliable tool for the Multiscale analysis of composite materials is provided; it represents a resanonable compromise between efficiency and numerical accuracy but indeed additional improvements may be introduced in both respect. Future developments may include:

- introduction of a clustering technique during the precomputations for the divison of the RVE in optimized subsets;

- further research regarding the integration scheme used during the precomputations, in the framework of both PWUHS and PWUTFA, in order to

investigate the *locking* related issues arising using full integration elements;

- investigating the influence of UC's dimensions, with respect to the structural size, on the model capability to naturally account for size effects;

- extension of the FE code with implemented PWUHS homogenization to parallel computing;
- extension to finite-strain at both the macroscopic and microscopic level.

Bibliography

[1] A. Hershey, "The elasticity of an isotropic aggregate of anisotropic cubic crystals," *Journal of Applied mechanics-transactions of the ASME*, vol. 21, no. 3, pp. 236–240, 1954.

[2] J. D. Eshelby, "The determination of the elastic field of an ellipsoidal inclusion, and related problems," *Proceedings of the Royal Society of London A: Mathematical, Physical and Engineering Sciences*, vol. 241, no. 1226, pp. 376–396, 1957.

[3] R. Hill, "A self-consistent mechanics of composite materials," *Journal of the Mechanics and Physics of Solids*, vol. 13, no. 4, pp. 213–222, 1965.

[4] Z. Hashin and S. Shtrikman, "On some variational principles in anisotropic and nonhomogeneous elasticity," *Journal of the Mechanics and Physics of Solids*, vol. 10, no. 4, pp. 335–342, 1962.

[5] Z. Hashin and S. Shtrikman, "A variational approach to the theory of the elastic behaviour of multiphase materials," *Journal of the Mechanics and Physics of Solids*, vol. 11, no. 2, pp. 127–140, 1963.

[6] D. Talbot and J. Willis, "Variational principles for inhomogeneous nonlinear media," *IMA Journal of Applied Mathematics*, vol. 35, no. 1, pp. 39–54, 1985.

[7] P. Ponte Castañeda, "The effective mechanical properties of nonlinear isotropic composites," *Journal of the Mechanics and Physics of Solids*, vol. 39, no. 1, pp. 45–71, 1991.

[8] P. Ponte Castañeda, "New variational principles in plasticity and their application to composite materials," *Journal of the Mechanics and Physics of Solids*, vol. 40, no. 8, pp. 1757–1788, 1992.

[9] P. Ponte Castañeda and P. Suquet, *Nonlinear composites*, vol. 34. Elsevier, 1998.

[10] V. Kouznetsova, W. Brekelmans, and F. Baaijens, "Approach to micro-macro modeling of heterogeneous materials," *Computational Mechanics*, vol. 27, pp. 37–48, 01 2001.

[11] V. Kouznetsova, M. Geers, and W. Brekelmans, "Multi-scale second-order computational homogenization of multi-phase materials: a nested finite element solution strategy," *Computer Methods in Applied Mechanics and Engineering*, vol. 193, no. 48, pp. 5525 – 5550, 2004. Advances in Computational Plasticity.

[12] M. Geers, V. Kouznetsova, and W. Brekelmans, "Multi-scale computational homogenization: Trends and challenges," *Journal of Computational and Applied Mathematics*, vol. 234, no. 7, pp. 2175 – 2182, 2010.

[13] F. Feyel and J.-L. Chaboche, "Fe2 multiscale approach for modelling the elastoviscoplastic behaviour of long fibre sic/ti composite materials.," *Computer Methods in Applied Mechanics and Engineering*, vol. 183, pp. 309–330, 2000.

[14] J. Cognard and P. Ladeveze, "The large time increment method applied to cyclic loadings," in *Creep in Structures* (M. Zyczkowski, ed.), (Berlin, Heidelberg), pp. 555–562, Springer Berlin Heidelberg, 1991.

[15] F. Chinesta, A. Ammar, A. Leygue, and R. Keunings, "An overview of the proper generalized decomposition with applications in computational rheology," *Journal of Non-Newtonian Fluid Mechanics*, vol. 166, no. 11, pp. 578 – 592, 2011.

[16] M. Signorini, S. Zlotnik, and P. Diez, "Proper generalized decomposition solution of the parameterized helmholtz problem: application to inverse geophysical problems.," *International Journal for Numerical Methods in Engineering*, vol. 109, 2016.

[17] P. Diez, S. Zlotnik, A. Garcia-Gonzalez, and A. Huerta, "Algebraic pgd for tensor separation and compression: An algorithmic approach," *Comptes Rendus Mecanique*, vol. 346, no. 7, pp. 501 – 514, 2018. Model reduction, data-based and advanced discretization in computational mechanics.

[18] F. Chinesta, A. Leygue, F. Bordeu, J. V. Aguado, E. Cueto, D. Gonzalez, I. Alfaro, A. Ammar, and A. Huerta, "Pgd-based computational vademecum for efficient design, optimization and control," *Archives of Computational Methods in Engineering*, vol. 20, 2013.

[19] K. Matou, M. G. Geers, V. G. Kouznetsova, and A. Gillman, "A review of predictive nonlinear theories for multiscale modeling of heterogeneous materials," *Journal of Computational Physics*, vol. 330, pp. 192 – 220, 2017.

[20] G. J. Dvorak, "Transformation field analysis of inelastic composite materials," *Proceedings of the Royal Society of London. Series A: Mathematical and Physical Sciences*, vol. 437, no. 1900, pp. 311–327, 1992.

[21] J. Chaboche, L. Kruch, J. Maire, and T. Pottier, "Towards a micromechanics based inelastic and damage modeling of composites," *International Journal of Plasticity*, vol. 17.

[22] E. Sacco, "A nonlinear homogenization procedure for periodic masonry," *European Journal of Mechanics - A/Solids*, vol. 28, no. 2, pp. 209 – 222, 2009.

[23] S. Marfia and E. Sacco, "Multiscale technique for nonlinear analysis of elastoplastic and viscoplastic composites," *Composites Part B: Engineering*, vol. 136, pp. 241 – 253, 2018.

[24] J. Michel and P. Suquet, "Nonuniform transformation field analysis," *International Journal of Solids and Structures*, vol. 40, no. 25, pp. 6937 – 6955, 2003. Special issue in Honor of George J. Dvorak.

[25] J.-C. Michel and P. Suquet, "Non-uniform transformation field analysis: A reduced model for multiscale non-linear problems in solid mechanics," *Multiscale Modeling in Solid Mechanics*, pp. 159–206, 2009.

[26] F. Fritzen and T. Bohlke, "Nonuniform transformation field analysis of materials with morphological anisotropy," *Composites Science and Technology*, vol. 71, no. 4, pp. 433 – 442, 2011.

[27] V. Sepe, S. Marfia, and E. Sacco, "A nonuniform TFA homogenization technique based on piecewise interpolation functions of the inelastic field," *International Journal of Solids and Structures*, vol. 50, no. 5, pp. 725 – 742, 2013.

[28] F. Fritzen, S. Marfia, and V. Sepe, "Reduced order modeling in nonlinear homogenization: a comparative study," *Computers & Structures*, vol. 157, pp. 114–131, 2015.

[29] S. Marfia and E. Sacco, "Computational homogenization of composites experiencing plasticity, cracking and debonding phenomena," *Computer Methods in Applied Mechanics and Engineering*, vol. 304, pp. 319 – 341, 2016.

[30] F. Covezzi, S. de Miranda, S. Marfia, and E. Sacco, "Homogenization of elastic-viscoplastic composites by the mixed TFA," *Comput Methods Appl Mech Eng*, vol. 318, pp. 701–723, 2017.

[31] G. Alaimo, F. Auricchio, S. Marfia, and E. Sacco, "Optimization clustering technique for PieceWise Uniform Transformation Field Analysis homogenization of viscoplastic composites," *Computational Mechanics*, vol. 64, pp. 1495–1516, dec 2019.

[32] R. Luciano and J. Willis, "Hashin-Shtrikman basedFEanalysis of the elastic behaviour of finite random composite bodies," *International Journal of Fracture*, vol. 137, pp. 261–273, 01 2006.

[33] S. Wulfinghoff, F. Cavaliere, and S. Reese, "Model order reduction of nonlinear homogenization problems using a Hashin-Shtrikman type finite element method," *Computer Methods in Applied Mechanics and Engineering*, vol. 330, pp. 149 – 179, 2018.

[34] D. Jaworek, C. Gierden, J. Waimann, S. Wulfinghoff, and S. Reese, "A Hashin-Shtrikman type semi-analytical homogenization procedure in multiscale modeling to account for coupled problems," *TECHNISCHE MECHANIK*, vol. 40, no. 1, pp. 45–52, 2020.

[35] F. Cavaliere, S. Reese, and S. Wulfinghoff, "Efficient two-scale simulations of engineering structures using the Hashin-shtrikman type finite element method," *Computational Mechanics*, vol. 65, pp. 159–175, aug 2019.

[36] Z. Liu, M. Bessa, and W. K. Liu, "Self-consistent clustering analysis: An efficient multi-scale scheme for inelastic heterogeneous materials," *Computer Methods in Applied Mechanics and Engineering*, vol. 306, pp. 319 – 341, 2016.

[37] R. Hill, "Elastic properties of reinforced solids: Some theoretical principles," *Journal of the Mechanics and Physics of Solids*, vol. 11, no. 5, pp. 357 – 372, 1963.

[38] S. Li, "On the unit cell for micromechanical analysis of fibre-reinforced composites," *Proceedings of The Royal Society A: Mathematical, Physical and Engineering Sciences*, vol. 455, pp. 815–838, 03 1999.

[39] B. Budiansky, "Thermal and thermoelastic properties of isotropic composites," *Journal of Composite Materials*, vol. 4, no. 3, pp. 286–295, 1970.

[40] "On bounds for the overall elastic moduli of inhomogeneous systemsi," *Journal of the Mechanics and Physics of Solids*, vol. 14, no. 3, pp. 151 – 162, 1966.

[41] L. Walpole, "Elastic behavior of composite materials: Theoretical foundations," vol. 21 of *Advances in Applied Mechanics*, pp. 169 – 242, Elsevier, 1981.

[42] J. Willis, *Mechanics of Composites:*. Ecole polytechnique, Département de mécanique, 2002.

[43] "Bounds and self-consistent estimates for the overall properties of anisotropic composites," *Journal of the Mechanics and Physics of Solids*, vol. 25, no. 3, pp. 185 – 202, 1977.

[44] W. Voigt, "Ueber die beziehung zwischen den beiden elasticitconstanten isotroper krper," *Annalen der Physik*, vol. 274, no. 12, pp. 573–587, 1889.

[45] A. Reuss, "Berechnung der flierenze von mischkristallen auf grund der plastizitbedingung fr einkristalle .," *ZAMM - Journal of Applied Mathematics and Mechanics / Zeitschrift fr Angewandte Mathematik und Mechanik*, vol. 9, no. 1, pp. 49–58, 1929.

[46] "Bounds for effective elastic moduli of disordered materials," *Journal of the Mechanics and Physics of Solids*, vol. 25, no. 2, pp. 137 – 155, 1977.

[47] C. Tucker and E. Liang, "Stiffness predictions for unidirectional short-fiber composites: Review and evaluation," *Journal of Computer Science and Technology*, 1998.

[48] P. Wall, "A comparison of homogenization, hashin-shtrikman bounds and the halpin-tsai equations," *Applications of Mathematics*, vol. 42, pp. 245–257, 1997.

[49] F. Feyel, "Multiscale fe2 elastoviscoplastic analysis of composite structures," *Computational Materials Science*, vol. 16, no. 1, pp. 344 – 354, 1999.

[50] K. Terada and N. Kikuchi, "Nonlinear homogenization method for practical applications," *American Society of Mechanical Engineers, Applied Mechanics Division, AMD*, vol. 212, pp. 1–16, 01 1995.

[51] R. Smit, W. Brekelmans, and H. Meijer, "Prediction of the mechanical behavior of nonlinear heterogeneous systems by multi-level finite element modeling," *Computer Methods in Applied Mechanics and Engineering*, vol. 155, no. 1, pp. 181 – 192, 1998.

[52] C. Miehe, J. Schrder, and J. Schotte, "Computational homogenization analysis in finite plasticity simulation of texture development in polycrystalline materials," *Computer Methods in Applied Mechanics and Engineering*, vol. 171, no. 3, pp. 387 – 418, 1999.

[53] F. Feyel, "A multilevel finite element method (fe2) to describe the response of highly non-linear structures using generalized continua," *Computer Methods in Applied Mechanics and Engineering*, vol. 192, no. 28, pp. 3233 – 3244, 2003. Multiscale Computational Mechanics for Materials and Structures.

[54] L. Kaczmarczyk, C. J. Pearce, N. Bicanic, and E. de Souza Neto, "Numerical multiscale solution strategy for fracturing heterogeneous materials," *Computer Methods in Applied Mechanics and Engineering*, vol. 199, no. 17, pp. 1100 – 1113, 2010.

[55] A. Bacigalupo and L. Gambarotta, "Second-order computational homogenization of heterogeneous materials with periodic microstructure," *ZAMM - Journal of Applied Mathematics and Mechanics / Zeitschrift fr Angewandte Mathematik und Mechanik*, vol. 90, no. 10?11, pp. 796–811, 2010.

[56] J. Bonet and R. Wood, "Nonlinear continuum mechanics for finite element analysis," 1997.

[57] J. Simo and T. Hughes, *Computational inelasticity*. Interdisciplinary applied mathematics Mechanics and materials, New York: Springer.

[58] J. C. Simo and R. L. Taylor, "A return mapping algorithm for plane stress elastoplasticity," *International Journal for Numerical Methods in Engineering*, vol. 22, no. 3, pp. 649–670, 1986.

[59] J. Aboudi, *Mechanics of composite materials : a unified micromechanical approach*. Elsevier Amsterdam ; New York, 1991.

[60] M. Schwarze and S. Reese, "A reduced integration solid-shell finite element based on the eas and the ans concept geometrically linear problems," *International Journal for Numerical Methods in Engineering*, vol. 80, no. 10, pp. 1322–1355, 2009.

[61] G. P. Tandon and G. J. Weng, "A theory of particle-reinforced plasticity," *Journal of Applied Mechanics*, vol. 55, pp. 126–135, 03 1988.

[62] P. Suquet, "Overall properties of nonlinear composites: a modified secant moduli theory and its link with ponte castañeda's nonlinear variational procedure," 1995.

[63] O. Pierard, C. Gonzalez, J. Segurado, J. LLorca, and I. Doghri, "Micromechanics of elasto-plastic materials reinforced with ellipsoidal inclusions," *International Journal of Solids and Structures*, vol. 44, no. 21, pp. 6945 – 6962, 2007.

[64] O. C. Zienkiewicz, R. L. Taylor, and J. M. Too, "Reduced integration technique in general analysis of plates and shells," *International Journal for Numerical Methods in Engineering*, vol. 3, no. 2, pp. 275–290, 1971.

[65] W. P. Doherty, E. L. Wilson, and R. L. Taylor, "Stress analysis of axisymmetric solids utilizing higher-order quadrilateral finite elements," *University of California, Structural Engineering Laboratory*, 1969.

[66] D. Griffiths and G. Mustoe, "Selective reduced integration of four-node plane element in closed form," *Journal of Engineering Mechanics-asce - J ENG MECH-ASCE*, vol. 121, 06 1995.

[67] A. Alderson and K. L. Alderson, "Auxetic materials," *Proceedings of the Institution of Mechanical Engineers, Part G: Journal of Aerospace Engineering*, vol. 221, no. 4, pp. 565–575, 2007.

[68] K. E. Evans and M. A. Nkansah, "Molecular network design," *Nature*, vol. 353, no. 6340, p. 124, 1991.

[69] R. F. Almgrem, "An isotropic three-dimensional structure with poisson's ratio = -1," *Journal of Elasticity*, vol. 15, pp. 427–430, 12 1985.

[70] R. LAKES, "Foam structures with a negative poisson's ratio," *Science*, vol. 235, no. 4792, pp. 1038–1040, 1987.

[71] D. Prall and R. Lakes, "Properties of a chiral honeycomb with a poisson's ratio of 1," *International Journal of Mechanical Sciences*, vol. 39, no. 3, pp. 305 – 314, 1997.

[72] J. Dirrenberger, S. Forest, and D. Jeulin, "Effective elastic properties of auxetic microstructures: Anisotropy and structural applications," *International Journal of Mechanics and Materials in Design*, vol. 9, 03 2012.

[73] P. Ramaiah Budarapu, S. Yb, and R. Natarajan, "Design concepts of an aircraft wing: composite and morphing airfoil with auxetic structures," *Frontiers of Structural and Civil Engineering*, vol. 10, pp. 1–15, 11 2016.

[74] S. Hou, T. Liu, Z. Zhang, X. Han, and Q. Li, "How does negative poissons ratio of foam filler affect crashworthiness?," *Materials & Design*, vol. 82, pp. 247 – 259, 2015.

[75] N. Novak, M. Vesenjak, and Z. Ren, "Auxetic cellular materials - a review," vol. 62, pp. 485–493, 09 2016.

[76] K. Saxena, R. Das, and E. Calius, "Three decades of auxetics research ? materials with negative poisson's ratio: A review," *Advanced Engineering Materials*, vol. 18, pp. n/a–n/a, 06 2016.

[77] L. J. Gibson, M. F. Ashby, G. S. Schajer, and C. I. Robertson, "The mechanics of two-dimensional cellular materials," *Proceedings of the Royal Society of London. Series A, Mathematical and Physical Sciences*, vol. 382, no. 1782, pp. 25–42, 1982.

[78] X. Jin, Z. Wang, J. Ning, G. Xiao, E. Liu, and X. Shu, "Dynamic response of sandwich structures with graded auxetic honeycomb cores under blast loading," *Composites Part B: Engineering*, vol. 106, pp. 206 – 217, 2016.

[79] N. Novak, K. Hokamoto, M. Vesenjak, and Z. Ren, "Mechanical behaviour of auxetic cellular structures built from inverted tetrapods at high strain rates," *International Journal of Impact Engineering*, vol. 122, pp. 83 – 90, 2018.

[80] Y. Xue, X. Wang, W. Wang, X. Zhong, and F. Han, "Compressive property of al-based auxetic lattice structures fabricated by 3-d printing combined with investment casting," *Materials Science and Engineering: A*, vol. 722, pp. 255 – 262, 2018.

[81] H. Zhou, K. Jia, X. Wang, M.-X. Xiong, and Y. Wang, "Experimental and numerical investigation of low velocity impact response of foam concrete filled auxetic honeycombs," *Thin-Walled Structures*, vol. 154, p. 106898, 2020.

[82] A. Airoldi, N. Novak, F. Sgobba, A. Gilardelli, and M. Borovinek, "Foam-filled energy absorbers with auxetic behaviour for localized impacts," *Materials Science and Engineering: A*, vol. 788, p. 139500, 2020.

[83] C. Ma, H. Lei, J. Liang, W. Wu, T. Wang, and D. Fang, "Macroscopic mechanical response of chiral-type cylindrical metastructures under axial compression loading," *Materials & Design*, vol. 158, pp. 198 – 212, 2018.

[84] D. Xiao, X. Chen, Y. Li, W. Wu, and D. Fang, "The structure response of sandwich beams with metallic auxetic honeycomb cores under localized impulsive loading-experiments and finite element analysis," *Materials & Design*, vol. 176, p. 107840, 2019.

[85] J. PENZIEN and T. DIDRIKSSON, "Effective shear modulus of honeycomb cellular structure," *AIAA Journal*, vol. 2, no. 3, pp. 531–535, 1964.

[86] M. Grediac, "A finite element study of the transverse shear in honeycomb cores," *International Journal of Solids and Structures*, vol. 30, no. 13, pp. 1777 – 1788, 1993.

[87] V. Burlayenko and T. Sadowski, "Effective elastic properties of foam-filled honeycomb cores of sandwich panels," *Composite Structures*, vol. 92, no. 12, pp. 2890 – 2900, 2010.

[88] J. Huang, Q. Zhang, F. Scarpa, Y. Liu, and J. Leng, "In-plane elasticity of a novel auxetic honeycomb design," *Composites Part B: Engineering*, vol. 110, pp. 72 – 82, 2017.

[89] C. Quan, B. Han, Z. Hou, Q. Zhang, X. Tian, and T. J. Lu, "3d printed continuous fiber reinforced composite auxetic honeycomb structures," *Composites Part B: Engineering*, vol. 187, p. 107858, 2020.

[90] V. Lvov, F. Senatov, A. Korsunsky, and A. Salimon, "Design and mechanical properties of 3d-printed auxetic honeycomb structure," *Materials Today Communications*, vol. 24, p. 101173, 2020.

[91] G. Wypych, "Pa-12 polyamide-12," in *Handbook of Polymers* (G. Wypych, ed.), pp. 239 – 243, Oxford: Elsevier, 2012.

[92] HP Development Company, *HP 3D High Reusability PA 12*, 2017.

[93] BCI Polyurethane Europe, *Promol® DP 25/10B1, techical data sheet*, 2018. TDS/AM-MC 2018.

[94] BCI Polyurethane Europe, *Promol® VA 50/6A3, techical data sheet*, 2020. TDS/AM-MC 2020.

[95] ASTM Standard D1621-16, *Standard Test Method for Compressive Properties of Rigid Cellular Plastics*. ASTM International, West Conshohocken, PA, 2016.

[96] R. L. Taylor, "Feap - a finite element analysis program. version 8.3. user manual," 2011.

[97] R. Luciano and E. Sacco, "Variational methods for the homogenization of periodic heterogeneous media," *European Journal of Mechanics - A/Solids*, vol. 17, no. 4, pp. 599 – 617, 1998.

[98] G. Giambanco, E. La Malfa Ribolla, and A. Spada, "Ch of masonry materials via meshless meso-modeling," *Frattura ed Integritá Strutturale*, vol. 8, pp. 150–165, 07 2014.